Forschungsbericht 2025-17

Calibration of a Nose Boom Mounted Airflow Sensor on an Atmospheric Research Aircraft by Inflight Maneuvers

incl. Appendix A

Andreas Giez, Christian Mallaun,
Vladyslav Nenakhov, Martin Zöger

Deutsches Zentrum für Luft- und Raumfahrt
Einrichtung Flugexperimente
Oberpfaffenhofen

DLR Deutsches Zentrum für Luft- und Raumfahrt

Forschungsbericht 2025-17

Calibration of a Nose Boom Mounted Airflow Sensor on an Atmospheric Research Aircraft by Inflight Maneuvers

incl. Appendix A

Andreas Giez, Christian Mallaun,
Vladyslav Nenakhov, Martin Zöger

Deutsches Zentrum für Luft- und Raumfahrt
Einrichtung Flugexperimente
Oberpfaffenhofen

195 Seiten
129 Bilder
10 Tabellen
20 Literaturstellen

DLR Deutsches Zentrum für Luft- und Raumfahrt

Herausgeber:

Deutsches Zentrum
für Luft- und Raumfahrt e. V.
Wissenschaftliche Information
Linder Höhe
D-51147 Köln

ISSN 1434-8454
ISRN DLR-FB-2025-17
Erscheinungsjahr 2025
DOI: 10.57676/7wf2-dk78

Atmosphärenforschungsflugzeug, Luftströmungssensor, Kalibrierung während des Fluges, Bugausleger, dynamische Kalibrierung, Windmessung in der Luft

Andreas Giez, Christian Mallaun, Vladyslav Nenakhov, Martin Zöger
DLR, Einrichtung Flugexperimente, Oberpfaffenhofen

Kalibrierung eines an der Nase montierten Luftströmungssensors an einem Atmosphärenforschungsflugzeug durch Inflight Manöver inkl. Anhang A

Das Dokument demonstriert die vollständige Kalibrierung eines Luftströmungssensors auf dem deutschen Atmosphärenforschungsflugzeug HALO.

Die an der Spitze eines Bugauslegers montierte Luftströmungssonde misst den statischen und dynamischen Druck sowie die beiden Strömungswinkel "Anstellwinkel" α und "Schiebewinkel" β. Diese vier Einheiten und eine Temperaturmessung werden benötigt, um den kompletten 3-dimensionalen Luftströmungsvektor zu berechnen, der sowohl für Flugtests als auch für die Bestimmung des Windgeschwindigkeitsvektors in der Atmosphärenforschung verwendet wird. Der Bericht basiert auf der vorangegangenen statischen Quellenkalibrierung dieses Sensors mit Hilfe eines Schleppkegels, die in einem vorangegangenen DLR Forschungsbericht (2019-07) dokumentiert ist.

Das Dokument demonstriert Schritt für Schritt, wie die notwendigen Korrekturen bestimmt werden, die erforderlich sind, um den wahren Luftströmungsvektor mit extrem kleinen Messfehlern und einer hohen zeitlichen Auflösung zu berechnen.

Die Kalibrierung verwendet bekannte Eigenschaften des atmosphärischen Windes und erfordert daher die Einrichtung einer 3-Dim-Windmessung am Flugzeug.

Der notwendige experimentelle Flugtestaufwand betrifft statische Kalibrierungsverfahren für die mittleren Luftdateneinheiten sowie dynamische Manöver, die erforderlich sind, um die Reaktion des experimentellen Luftdatensystems auf schnelle Luftströmungsschwankungen zu untersuchen. Die dynamischen Korrekturen beweisen, dass die direkte Messung von vertikalen und horizontalen Windschwankungen eine Richtungsempfindlichkeit aufweist, die korrigiert werden muss, wenn die Daten für meteorologische Untersuchungen verwendet werden sollen.

Atmospheric research aircraft, air flow sensor, inflight calibration, nose boom, dynamic calibration, airborne wind measurement

Andreas Giez, Christian Mallaun, Vladyslav Nenakhov, Martin Zöger
German Aerospace Center (DLR), Flight Experiments Facility, Oberpfaffenhofen

Calibration of a Nose Boom Mounted Airflow Sensor on an Atmospheric Research Aircraft by Inflight Maneuvers
incl. Appendix A

The document demonstrates the complete calibration of an air data sensor on the German atmospheric research aircraft HALO.

The airflow probe which is mounted on the tip of a nose boom measures static and dynamic pressure as well as the two airflow angles “angle of attack” α and “angle of sideslip” β. These four units and a temperature measurement are required to calculate the complete 3-dimensional airflow vector which is used for flight testing as well as for the determination of the wind speed vector in atmospheric research. The report is based on the static source calibration of this sensor by means of a trailing cone which is documented in a preceeding DLR Forschungsbericht (2019-07).

The document demonstrates step by step how to determine the necessary corrections which are required to calculate the true airflow vector with extremely small measurement errors and a high temporal resolution.

The calibration uses known properties of the atmospheric wind and therefore requires the establishment of a 3-dim wind measurement on the aircraft.

The necessary experimental flight test effort concerns static calibration procedures for the mean air data units as well as dynamic maneuvers which are required to investigate the response of the experimental air data system to fast airflow fluctuations. The dynamic corrections prove that the direct measurement of vertical and horizontal wind fluctuations shows a directional sensitivity which must be corrected if the data is used for meteorological investigations.

(Published in English)

Forschungsbericht 2025-17

Calibration of a Nose Boom Mounted Airflow Sensor on an Atmospheric Research Aircraft by Inflight Maneuvers

incl. Appendix A

Andreas Giez, Christian Mallaun,
Vladyslav Nenakhov, Martin Zöger

Deutsches Zentrum für Luft- und Raumfahrt
Flugexperimente
Forschungsflugabteilung Oberpfaffenhofen

DLR Deutsches Zentrum für Luft- und Raumfahrt

Abstract

The document demonstrates the complete calibration of an air data sensor on the German atmospheric research aircraft HALO.

The airflow probe which is mounted on the tip of a nose boom measures static and dynamic pressure as well as the two airflow angles "angle of attack" α and "angle of sideslip" β. These four units and a temperature measurement are required to calculate the complete 3-dimensional airflow vector which is used for flight testing as well as for the determination of the wind speed vector in atmospheric research. The report is based on the preceding static source calibration of this sensor by means of a trailing cone which is documented in another report [5].

The document demonstrates step by step how to determine the necessary corrections which are required to calculate the true airflow vector with extremely small measurement errors and a high temporal resolution.

The calibration uses known properties of the atmospheric wind and therefore requires the establishment of a 3-dim wind measurement on the aircraft.

The necessary experimental flight test effort concerns static calibration procedures for the mean air data units as well as dynamic maneuvers which are required to investigate the response of the experimental air data system to fast airflow fluctuations. The dynamic corrections prove that the direct measurement of vertical and horizontal wind fluctuations shows a directional sensitivity which must be corrected if the data is used for meteorological investigations.

Content

Introduction

In the modern world aircraft represent one of the most powerful transport systems. Due to their speed aircraft are in great demand in the transportation of goods and passengers especially over large distances.

The performance of aircraft in the real world is described in terms of speed and distance covered and these units are usually referenced to the earth surface. The respective aircraft speed is known as ground speed ($\overrightarrow{gs}$) and relates to an earth fixed coordinate system.

However, the science behind a flying aircraft is aerodynamics which is based on a completely different perception. The reference system is no longer the earth but the aircraft itself and speed is measured with respect to the surrounding air. This velocity is called the True Air Speed ($\overrightarrow{TAS}$). Depending on the sign one can refer to $\overrightarrow{TAS}$ also as the airflow vector $\vec{v}_{air} = -\overrightarrow{TAS}$ with respect to the aircraft, i.e. the vector which describes the speed of the airflow relatively to the platform. The absolute value TAS as well as the orientation of the vector relatively to the aircraft coordinate system are essential data for the aircraft operation. A precise measurement of $\overrightarrow{TAS}$ is of great importance in order to describe the aircraft state and to guarantee a safe operation of the platform. Therefore, all aircraft must carry a reliable instrumentation to determine TAS and in many cases its orientation with respect to the aircraft x-axis.

Especially during the development and flight testing of new or modified aircraft flight science aims at the complete characterization of $\overrightarrow{TAS}$ during flight i.e. the measurement of the absolute value as well as the orientation with respect to the aircraft axes. Special instrumentation is needed for this task and most flight test aircraft carry a nose boom with an airflow sensor to allow for this measurement. However, the validation and calibration of such an instrument is extremely challenging since there is usually no direct reference data available for atmospheric parameters like pressure, flow speed or flow direction available along the flight path of an aircraft.

An analysis of the relation between $\overrightarrow{gs}$ and $\overrightarrow{TAS}$ involves another important parameter. If the air mass around the aircraft is at rest it becomes immediately clear that $\overrightarrow{gs}$ and $\overrightarrow{TAS}$ must be identical if they are compared with each other in the same coordinate system. While the coordinate transformation between an earth fixed and an aircraft coordinate system is easy to accomplish, the fact that the air is not at rest adds another unknown component to the speed analysis: the atmospheric wind speed $\overrightarrow{ws}$. From the above one can easily conclude that the difference between $\overrightarrow{gs}$ and $\overrightarrow{TAS}$ directly yields the wind speed $\overrightarrow{ws}$. Therefore, airborne wind measurements use $\overrightarrow{gs}$ and $\overrightarrow{TAS}$ to calculate a wind speed vector $\overrightarrow{ws}$.

In atmospheric science "wind" is a very important parameter. Atmospheric wind is well characterized and has specific properties which are known from experimental data collected with situ sensors (ground, tower, aircraft…) or remote sensing instruments (Lidar, Radar, …) as well as data from models and simulations based on physical or meteorological theory.

But there is another possible perspective: A close view on the calculated wind speed $\overrightarrow{ws}$ can be used to check the plausibility of the speed measurements of $\overrightarrow{gs}$ and $\overrightarrow{TAS}$ which are used to calculate it. We will show in this work that $\overrightarrow{ws}$ data can even be used to calibrate the aircraft measurements themselves.

For many reasons the speed vector $\overrightarrow{gs}$ of an object in an earth fixed coordinate system is much easier to determine than $\overrightarrow{TAS}$ which means that the wind data is mainly used to calibrate the airflow vector measurements.

In this work we will demonstrate the complete characterization and calibration of an airflow sensor system on a research aircraft and describe step by step the necessary flight test effort. It aims not only at the improvement of air data for flight tests but also at precise wind data measurements on aircraft dedicated to atmospheric science research.

Aircraft and Instrumentation

This report is based on actual aircraft data from flight tests performed by the Flight Experiments Facility of the German Aerospace Centre (DLR). The aircraft which was used for these experiments is the German Atmospheric Research Aircraft HALO (High Altitude and LOng Range Research Aircraft) which is briefly described in the following section.

Aircraft

The atmospheric research aircraft HALO is a Gulfstream Aerospace Corporation G550 business jet which was heavily modified this purpose. HALO is shown in Figure 1.

The modification work on this special mission aircraft took almost 3 years and concerned the airframe as well as the aircraft power and data system. As a result, HALO allows the installation and operation of scientific instrumentation throughout the whole aircraft. The required hardpoints and electrical interfaces concern not only the aircraft cabin itself but also the unpressurized compartments (rear compartment, tail cone, nose, vertical stabilizer, winglets), the aircraft fuselage (top, bottom, side) and the wing (6 wing stations). A large belly instrumentation pod can be attached to the aircraft bottom in order to carry additional instrumentation. Almost 30 large apertures in the fuselage allow for the installation of air intake systems as well as optical windows, antennas, radiation sensors or other external instrumentation. A detailed description of the HALO modifications can be found in [9].

Figure 1*: Atmospheric research aircraft HALO*

HALO was designed as a "multipurpose platform" which means that the aircraft is not operated with a fixed payload. The aircraft must be seen as a flexible airborne research platform for atmospheric science. HALO is a flying laboratory with a scientific instrumentation which can change completely between single missions and which is always optimized for the specific research task. As a consequence, the aircraft configuration changes several times per year. However, the basic configuration of HALO is an empty and "clean" aircraft. The only exception from this is the nose boom. This permanent installation carries the experimental air data sensor which is subject to this report.

Some of the mission configurations include external installations on the aircraft fuselage and wing. It is obvious that these modifications change the aircraft shape and possibly influence its aerodynamic properties (i.e. performance and handling qualities) as well as the quality of air data as measured by the aircraft avionic systems.

This possible impact is a very critical point in the certification of payloads and subject to extensive flight testing. Figure 2 visualizes some of the most important external installations on HALO.

Figure 2*: Examples of external payload installations on HALO which can influence the aircraft aerodynamic properties as well as the air data measurements on the aircraft. From left to right: Under-wing installation of cloud particle probes, large belly instrumentation pod and gas inlet installations on the aircraft fuselage.*

Basic Data System BAHAMAS

The only permanent installation of scientific instrumentation on HALO is the Basic HALO Measurement and Sensor System (BAHAMAS). BAHAMAS was developed by the Instrumentation and Data Science Group of the Flight Experiments Facility of DLR and supports the science projects on HALO with a basic data set which describes the aircraft state and air data for the surrounding atmosphere. BAHAMAS consists of several components:

- A main data acquisition rack in the rear cabin
- An instrumented box in the unpressurized nose section
- 6 Total Air Temperature (TAT) inlets in the aircraft nose section
- An instrumented nose boom
- GPS antennas, a data distribution network, …..

Concerning the aircraft state parameters, the system directly monitors several avionic systems of the Gulfstream G550 (Air Data System, Flight Management

Computer, Inertial Reference System etc. via ARIC 429) as well as the main aircraft avionic bus ASCB-D.

For the measurement of pressure, temperature, humidity and wind vector BAHAMAS deploys a set of own sensors:

- An experimental Inertial Reference System (IRS)
- Temperature sensors in selected TAT housings
- Humidity sensors in the nose box and in the main data acquisition rack
- An airflow sensor with pitot static probe at the tip of the nose boom

Figure 3 shows the most important components and their location on the aircraft. A detailed description of the sensors which are used for airflow/wind measurements will be given later in this report.

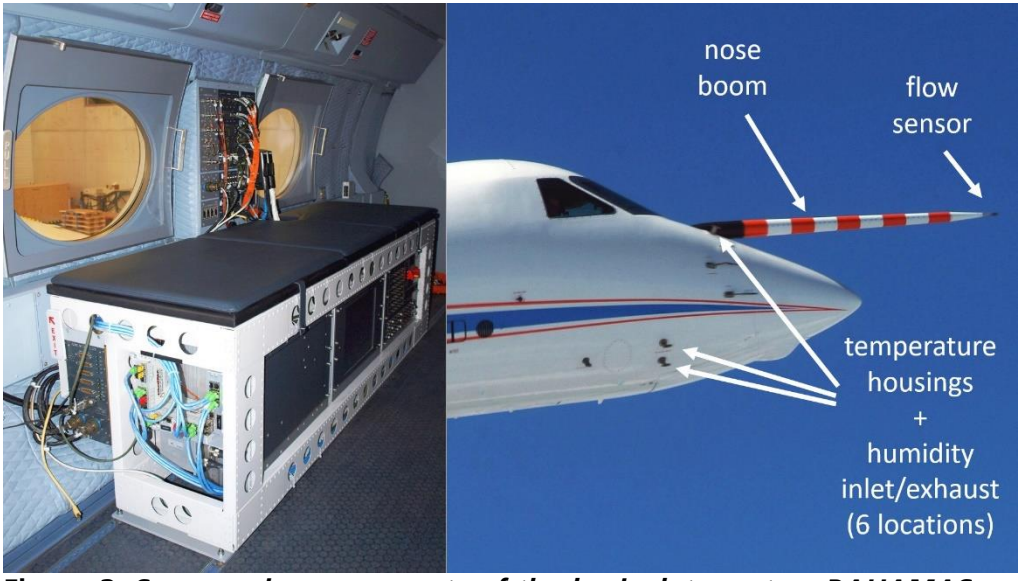

Figure 3*: Some main components of the basic data system BAHAMAS on HALO. Left side: main data acquisition rack in the aircraft cabin. Right side: Aircraft nose section with TAT inlets and the airflow instrumentation at the tip of the nose boom.*

Coordinate Systems and Transformation

The exact definition of coordinate systems, aeronautical units and angles in aviation is subject to national and international norms like [3]. Therefore, we want to point at these references for the precise definitions. In the following we will only briefly list the most important parameters which are required for this work.

Aircraft Based Reference System

The aircraft fixed coordinate system is an orthonormal system as shown in Figure 4 and bears no specific index.

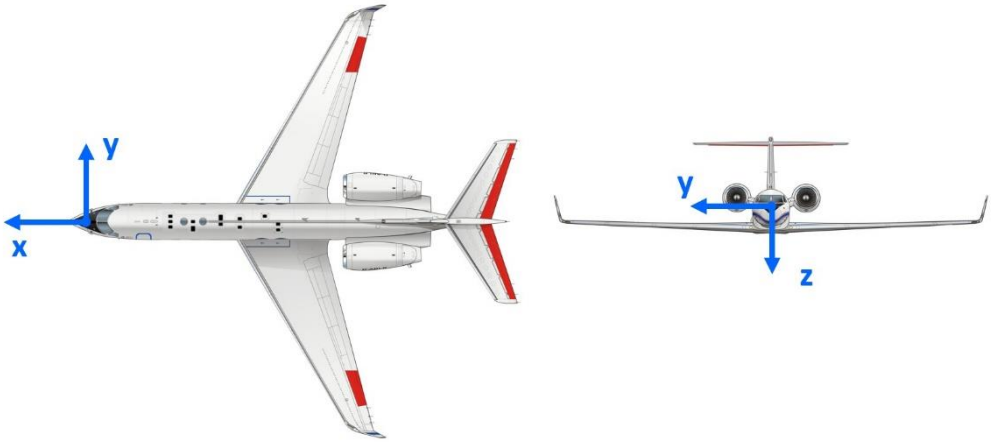

Figure 4: ***Orientation of the axes in an aircraft fixed coordinate system***

The orientation of the axes is shown in Figure 4 and defined as follows:

x : front
y : starboard
z : for normal flight state: down (defined by x and y)

The exact orientation of these axes is usually defined by the manufacturer of the respective aircraft and referenced in its technical data. In some cases, the principal axes of inertia or the aerodynamic body axes are chosen as x, y and z.

An important question concerns the location of the origin for this coordinate system. Although the manufacturer usually defines an exact origin for the drawings of the airframe there are other possible solutions which can simplify the interpretation of experimental data. The center of gravity is a good choice for flight test while another straight forward solution is the location of the inertial reference system (IRS) which is used to measure aircraft location, speed and attitude.
In order to directly use the output data from an IRS for flight tests or navigation it is necessary to properly align the system with the aircraft axes.
In case of atmospheric research, it turns out that a precise alignment between IRS and aircraft axes is **not important** for exact wind measurements using an airflow sensor. For this kind of measurement, the IRS defines the coordinate system i.e. origin and the orientation of the axes and the only critical parameter is the relative orientation of the flow sensor with respect to the IRS coordinate system. This angular relation is determined by the inflight calibration which is described in this report.
However, it is important to note that in traditional flight testing the exact IRS orientation relatively to the aircraft axes must be known. This requires a significant measurement/calibration effort before the actual flight trials can start.
In this work the origin of the aircraft fixed coordinate system and its orientation is defined by the experimental inertial reference system in the aircraft nose compartment. This instrument is described later in this report.
Throughout this report we assume a properly aligned IRS and we do not distinguish between "aircraft" and "IRS" coordinate system. However, the reference is always the IRS, i.e. even an angle of attack or a pitch angle refers to the IRS coordinate system.

Ground Based Reference System

This orthonormal coordinate system is fixed to the earth surface and marked with the index 'g'. The orientation of the axes is as follows:

x_g : North
y_g : East
z_g : Down (along g-vector)

The orientation of an aircraft in this system is described by three attitude angles pitch (θ), roll (ϕ) and yaw/heading (ψ). These three angles and the associated angular velocity $\vec{\omega}$ are often directly related to the aircraft axes as indicated in Figure 5. Although this is a descriptive picture to explain the principal relation between aircraft attitude angles and motion it is important to note that the exact definition of the three angles θ, ϕ, ψ and of $\vec{\omega}$ refers to the ground-based coordinate system [3]. As can be seen from Figure 6 the three angles are defined with respect to the projection of the aircraft axes on the earth fixed x-y-plane.

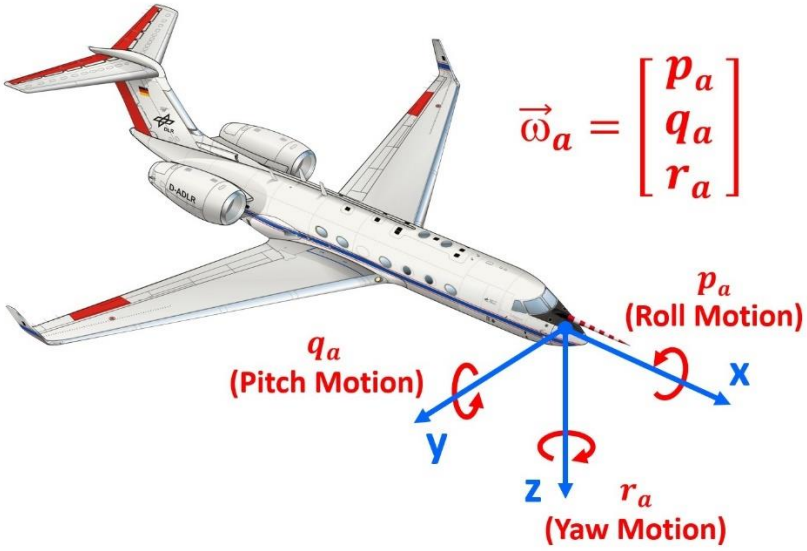

Figure 5*: Angular velocity $\vec{\omega}_a$ and its principal relation to changes of the aircraft attitude*.

The same is true for the angular velocities. However, modern inertial reference systems deliver angular rates with respect to the aircraft axes which are not consistent with the $\vec{\omega}$ which has been defined in the earth fixed coordinate system. We therefore introduce $\vec{\omega}_a = (p_a, q_a, r_a)$ as the angular velocity around the axes of the aircraft coordinate system as shown in Figure 5.

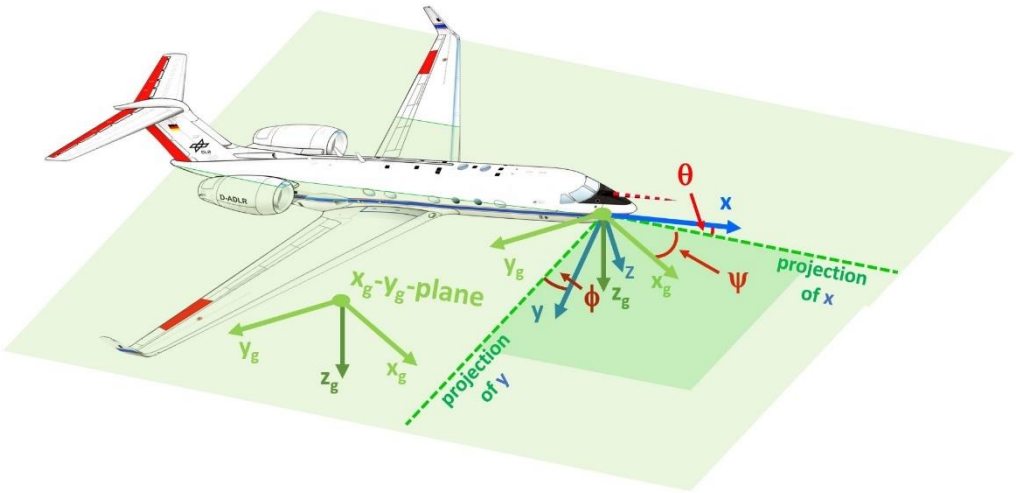

Figure 6*: Definition of the aircraft attitude angles in an earth fixed coordinate system (x_g,y_g,z_g). The projection of the aircraft coordinate system (x,y,z) on the earth fixed x_g-y_g-plane defines the attitude angles ψ, ϕ and θ. The example shows an aircraft with heading North-West (-90° <ψ< 0°), nose up (positive θ) during a right turn (right wing down, positive ϕ).*

Another important angle in the earth fixed coordinate system is the actual track angle (ATA). It describes the direction of the flight track (i.e. its tangent line during a turn) in the x_g-y_g-plane. It is important to note that this angle is typically not identical to the aircraft heading since an aircraft drifts under the influence of horizontal wind. The effect is described in the following chapters.

The analysis of atmospheric wind data in meteorological research often uses another convention. The horizontal wind speed $\overrightarrow{ws}$ refers to the x_g and y_g axes by

introducing the North-South (nsv) and East West (ewv) wind velocities and a horizontal wind speed direction (wa) which is 0° for North wind. Furthermore, vertical wind is positive in case of an upward motion, which is more intuitive while interpreting the data. All wind data shown in this work will follow this convention.

Coordinate System Transformation

The processing of aircraft data requires that the different measurements of airflow and ground speed are referenced to the same coordinate system. Therefore, it is necessary to perform a coordinate system transformation on the speeds vectors. As described above the relative orientation of an aircraft fixed coordinate system with respect to the earth is defined by the three aircraft attitude angles θ, ϕ and ψ. A transformation matrix C needed to transform the vector (x, y, z) from an aircraft fixed coordinate system into the earth-based coordinate system. This matrix is also defined in [3]:

$$\begin{bmatrix} x_g \\ y_g \\ z_g \end{bmatrix} = C \cdot \begin{bmatrix} x \\ y \\ z \end{bmatrix}$$

Equation 1

with

$$C = \begin{bmatrix} cos\theta\, cos\psi & sin\phi\, sin\theta\, cos\psi - cos\phi\, sin\psi & cos\phi\, sin\theta\, cos\psi + sin\phi\, sin\psi \\ cos\theta\, sin\psi & sin\phi\, sin\theta\, sin\psi + cos\phi\, cos\psi & cos\phi\, sin\theta\, sin\psi - sin\phi\, cos\psi \\ -sin\theta & sin\phi\, cos\theta & cos\phi\, cos\theta \end{bmatrix}$$

How to Measure Wind on an Aircraft

As stated above the wind speed vector $\overrightarrow{ws}$ is simply the difference between $\overrightarrow{TAS}$ and $\overrightarrow{gs}$ i.e. the (usually small) difference between two very large units.

$$\overrightarrow{ws} = \overrightarrow{gs} - \overrightarrow{TAS} = \overrightarrow{gs} + \vec{v}_{air} \qquad \textbf{Equation 2}$$

From this it becomes clear that a precise wind measurement requires extremely accurate data for $\overrightarrow{gs}$ and $\overrightarrow{TAS}$.
The source for ground speed data is usually a commercial IRS, which must be treated as a black box with no interfaces into the data handling or data processing.
In contrast $\overrightarrow{TAS}$ cannot be measured directly but has to be derived from air data which is acquired by an airflow sensor: according to [11] the absolute value of $\overrightarrow{TAS}$ can be calculated from

$$\mathrm{TAS} = \sqrt{C_2 \cdot T_s \cdot \left[\left(1 + \frac{\mathrm{qc}}{p_s}\right)^{\mathrm{C_1}} - 1\right]} \qquad \textbf{Equation 3}$$

where
$C_1 = \frac{\kappa - 1}{\kappa}$, $C_2 = 2 \cdot \frac{\mathrm{R}}{\mathrm{C_1}}$

p_s is the static pressure
qc is the dynamic (impact) pressure
κ is the adiabatic index
R the universal gas constant
T_S is the static air temperature

The determination of the orientation of $\overrightarrow{TAS}$ requires an additional flow angle measurement.

Please note that T_S represents an absolute temperature. Therefore, a typical measurement error of 0.5K for airborne temperature data [12] will not have a significant impact on the overall TAS accuracy. This means that the two pressure units qc and p_s represent the most critical inputs to this formula.
Another important speed unit is the Mach Number M_C which is regularly used throughout this report. M_C is defined as

$$M_c = \frac{aircraft\ air\ speed}{speed\ of\ sound} = \sqrt{5 \cdot \left[\left(\frac{\mathrm{qc}}{p_s} + 1\right)^{\frac{2}{7}} - 1\right]} \qquad \textbf{Equation 4}$$

The 2-dimensional Solution: Wind Triangle

All wind data provided by air data systems on commercial aircraft is calculated with this method. The wind triangle method is based on the assumption that the nose of any aircraft flying under stabilized and trimmed conditions always points directly into the airflow i.e. the direction of x and $\overrightarrow{TAS}$ are the same. As one can see in Figure 7 an aircraft starts to drift under the influence of lateral wind i.e. ATA and ψ will deviate from each other and the aircraft nose will not point along the flight path any more. One can then calculate the horizontal wind speed from a vector triangle which is made up by $\overrightarrow{gs}$, $\overrightarrow{TAS}$ and the drift angle δ = ATA-ψ. In case the aircraft is flying along the wind direction the wind speed becomes the simple difference between TAS and gs.
Due to the assumption of $\vec{x}$ and $\overrightarrow{TAS}$ being parallel the method does not require a sophisticated airflow sensor which is able to determine the direction of $\overrightarrow{TAS}$. The only instrumentation needed is an inertial reference system and a pitot static system + air data computer which can calculate TAS.

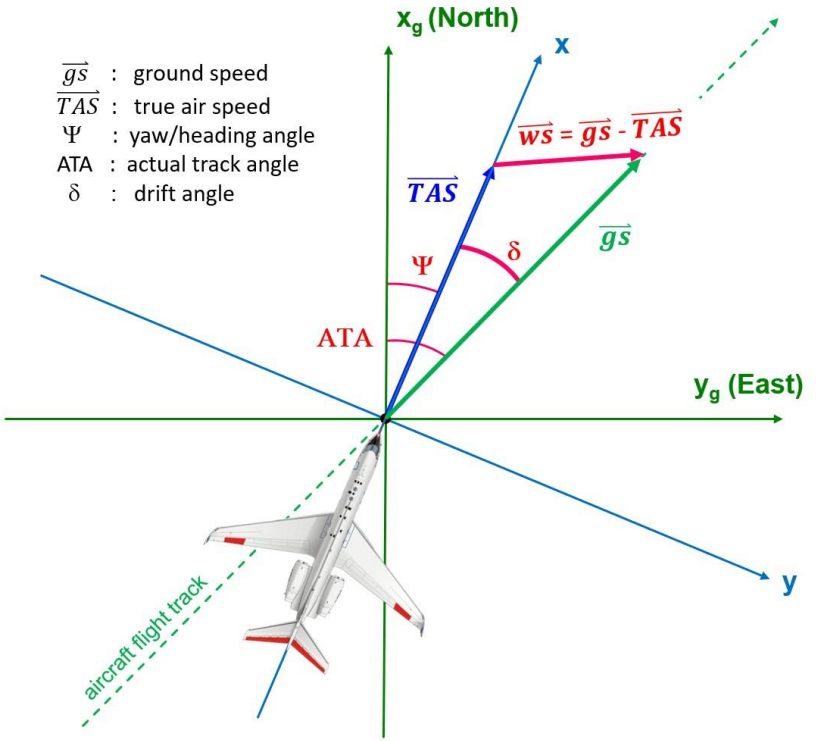

Figure *7: Determination of horizontal wind speed for an aircraft in trimmed, stabilized flight using the wind triangle method.*

The wind triangle has proven to be a very robust technique but there are some obvious disadvantages of this method:

- The wind triangle method is a 2-dimensional method which works in the x_g-y_g-plane. Therefore, it allows for horizontal wind measurements only and is not capable of detecting vertical wind.
- The method works for stabilized trimmed flight conditions only. Especially during turns the wind triangle does not deliver precise wind data any more. The same is true during any other aircraft maneuver like the ones presented later in this paper.
- Another requirement for good wind data is the precise alignment of the aircraft IRS with the aircraft (aerodynamic) x-axis. Any misalignment will

cause an offset in the drift angle (via ψ) which will result in erroneous wind data.

- The basic principle of this method is the assumption that the aircraft itself acts as a wind sensor. Changes in wind speed and direction will only be detected if the whole aircraft reacts to these conditions by changing its heading. Especially for a heavy and large aircraft it becomes clear that this reaction will always be significantly delayed and, in many cases, just too small to be detected. Therefore, the wind triangle method must be treated as a slow method which is not able to detect fast changes in the wind data.

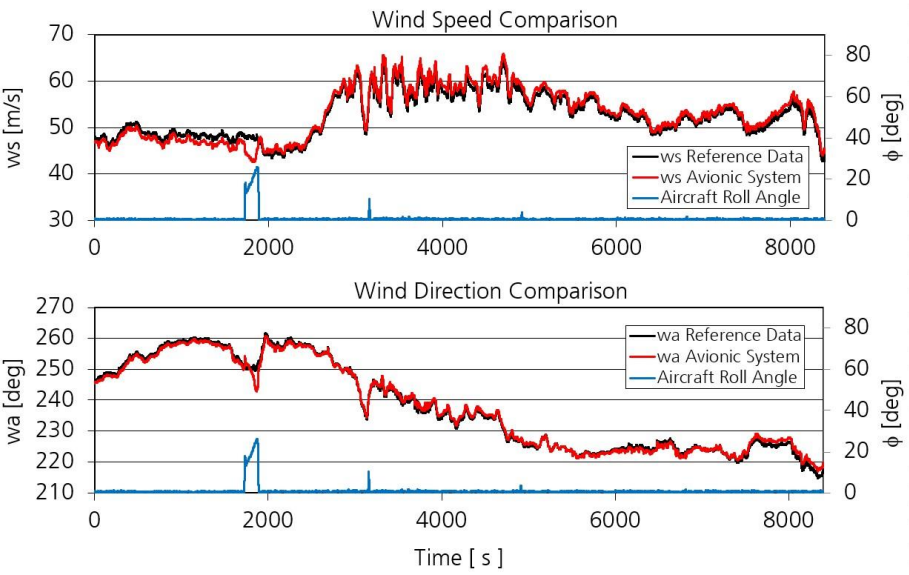

Figure 8*: Comparison between wind data calculated by the HALO avionic system using the wind triangle method and the precise reference data from BAHAMAS. The unit ws is the absolute value of the horizontal wind speed and wa the wind direction. The data set shows a flight leg of 02:20 h at a constant flight altitude of 12500m and a single turn. Deviations between the two data sources are obvious during the turn but also present during straight flight.*

As a general conclusion one can state that slow wind data variations lead to a response of the whole aircraft while fast and small changes in $\overrightarrow{ws}$ can only be detected as high frequency airflow variations. The detection of these variations requires a suitable sensor which is able to detect fast changes in airflow speed and direction.

Figure 8 and Figure 9 demonstrate these findings by comparing HALO data from the avionics system with the BAHAMAS reference measurements. Although the first impression indicates a relatively good agreement between wind triangle data and the precise data of the scientific system a detailed analysis yields systematic offsets and a significant error during maneuvers.

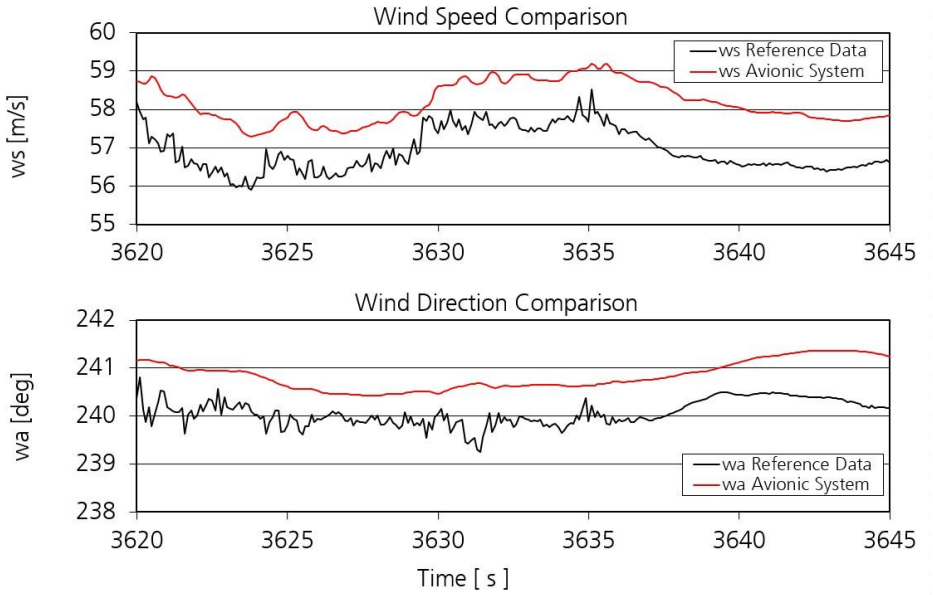

Figure 9*: Comparison between wind data calculated by the HALO avionic system using the wind triangle method and the precise reference data from BAHAMAS for a small subset of Figure 8. Besides a general offset error one can see the slow response time of the wind triangle method.*

The Exact Solution

The exact solution of airborne wind measurements is based on the complete and independent determination of the two speed vectors of $\overrightarrow{gs}$ and $\overrightarrow{TAS}$. This can only be achieved by using a flow sensor which is able to measure the complete airflow vector $\overrightarrow{TAS}$ including its vertical component. As shown in Figure 11 the 3-dimensional wind vector $\overrightarrow{ws}$ is then calculated as the difference of two speed vectors according to Equation 2.

A respective airflow sensor is capable of determining the two flow angles "angle of attack" (α) and "angle of sideslip" (β) which describe the orientation of $\overrightarrow{TAS}$ with respect to the aircraft axes. Figure 10 shows the definition of these two flow angles.

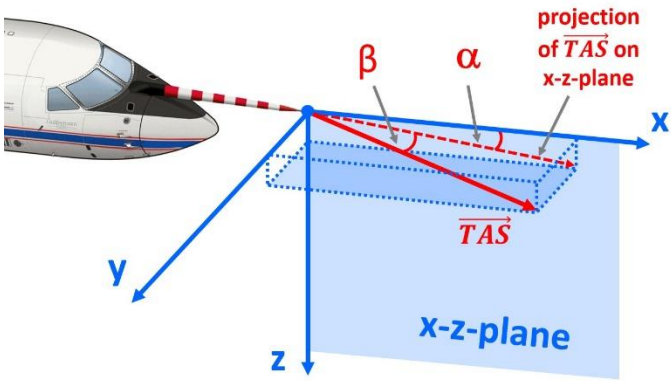

Figure 10*: Definition of the two flow angles α and β. The determination of the angle of attack α and angle of sideslip β refers to the projection of the $\overrightarrow{TAS}$ vector on the aircraft x-z-plane.*

From TAS, α and β the $\overrightarrow{TAS}$ vector can then be calculated according to [10]:

$$\overrightarrow{TAS} = \frac{TAS}{\sqrt{1 + tan^2(\alpha) + tan^2(\beta)}} \cdot \begin{bmatrix} 1 \\ \tan(\beta) \\ \tan(\alpha) \end{bmatrix} \qquad \textbf{Equation 5}$$

While $\overrightarrow{gs}$ is always referenced to an earth fixed coordinate system, the true air speed is determined with a sensor which is fixed to the aircraft structure. This means that the primary $\overrightarrow{TAS}$ measurement always refers to the aircraft axes. Therefore, it is necessary that the measured $\overrightarrow{TAS}$ vector undergoes a coordinate transformation into the earth fixed coordinate system ($\overrightarrow{TAS}_g$) before $\overrightarrow{ws}$ can be calculated.

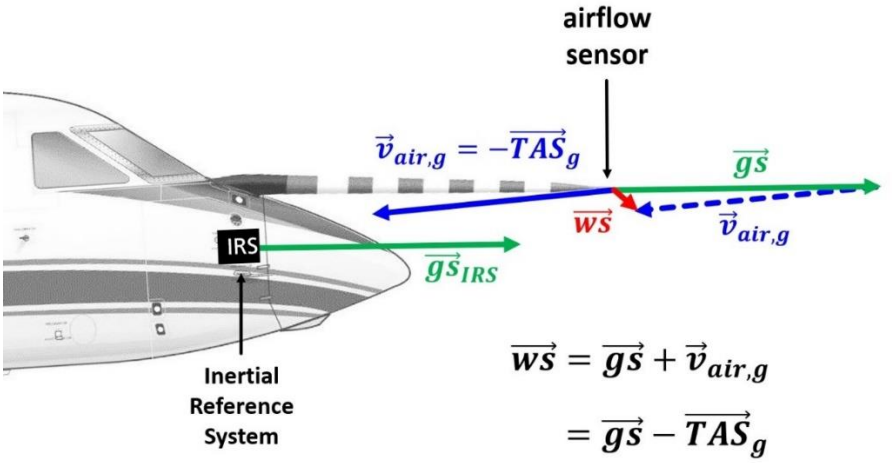

Figure 11*: Basic principle of the exact determination of the wind speed vector on an aircraft. The wind speed is calculated as the difference between two speed vectors: The ground speed $\overrightarrow{gs}$ and the true air speed $\overrightarrow{TAS}$. Both speeds must be referred to the same coordinate system ("g" = earth fixed coordinate system) as well as the same location on the aircraft.*

$\overrightarrow{gs}$ is measured by means of an inertial reference sensor on the aircraft. It must be clear, that the respective data set describes the motion of the IRS sensor itself only. Especially during changes of the aircraft attitude the ground related speed of any other location on the aircraft will slightly differ from the IRS data. Tn other words: the ground speed of the IRS $\overrightarrow{gs}_{IRS}$ is different from the ground speed of the airflow sensor $\overrightarrow{gs}$. Figure 12 shows that this speed difference can be calculated from the angular velocity vector $\vec{\omega}_a$ and the lever arm $\vec{R}$ between the IRS and the flow

sensor as $\vec{v}_{rot} = \vec{\omega}_a \times \vec{R}$. The $\vec{v}_{rot}$ vector also needs to be transferred into the earth fixed coordinate system according to Equation 1.
Due to this additional speed component it becomes important that the two vectors which are subtracted from each other in Equation 2 must refer to the same location on the aircraft. It is common to choose the tip of the airflow sensor as the reference point for a wind measurement, i.e.

$$\overrightarrow{gs} \overset{\text{def}}{=} \overrightarrow{gs}_{sensor} = \overrightarrow{gs}_{IRS} + \vec{v}_{rot,g} \qquad \textbf{Equation 6}$$

In this case $\overrightarrow{gs}$ and $\overrightarrow{TAS}$ describe the motion of the sensor itself. Please note that this reference point for the wind measurement has nothing to do with the origin of the aircraft fixed coordinate system.

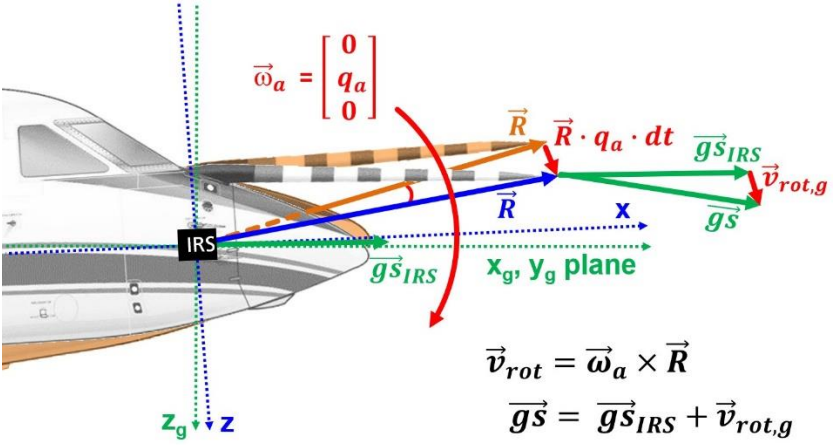

Figure 12*: A change of aircraft attitude results in a relative speed component between IRS and the airflow sensor which must be considered in the wind calculation. The example visualizes the effect for a downward pitch motion. The respective speed component can be calculated as the vector product of the angular velocity vector $\vec{\omega}_a$ and the lever arm $\vec{R}$ which describes the location of the measurement reference point which is the tip of the nose boom.*

The challenge for this kind of measurement results from the fact that the wind vector is measured as a relatively small difference between two very large units.

Therefore, the method requires extreme accuracies for the two aircraft speed measurements.

Required Data and Sensors

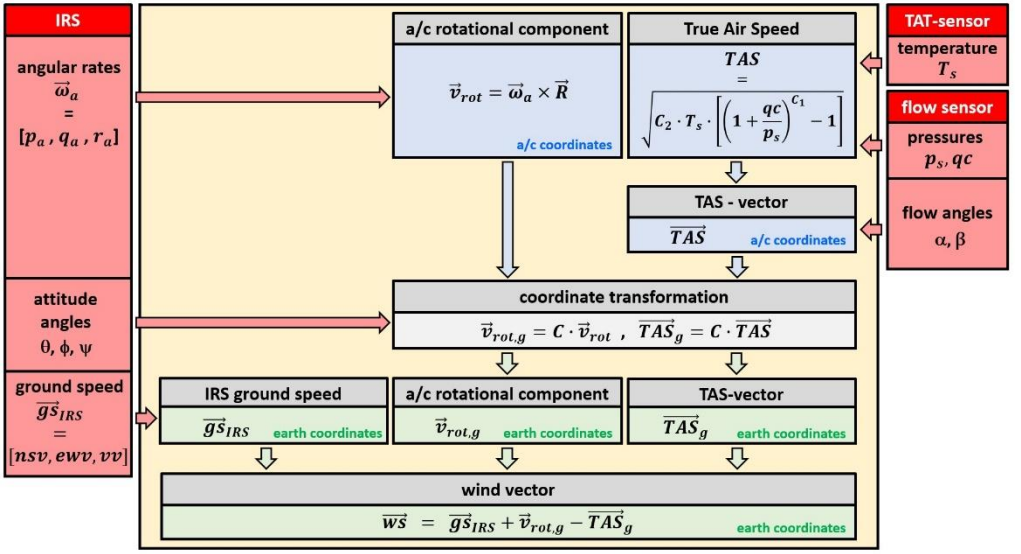

Figure 13*: Data sources and processing scheme for the wind speed vector measurement on an aircraft (a/c).*

Figure 13 visualizes the processing scheme of the wind vector calculation for an airborne platform which is equipped with an airflow sensor. As one can see the measurement involves three major sensors for the following data:

- inertial reference system (IRS):
  - attitude angles (θ, ϕ, ψ)
  - angular velocities (p_a, q_a, r_a)
  - ground speed (north-south: nsv, east west: ewv, vertical: vv)
- temperature sensor (TAT-sensor):
  - static air temperature (T_s)
- air data probe (airflow sensor):

- static pressure (p_s)
- dynamic (impact) pressure (qc)
- angle of attack (α)
- angle of sideslip (β)

Sensor Properties and Installation

While standard aircraft systems (avionics) have to fulfill official standards in order to get certified atmospheric science aims at maximum accuracy beyond these limits. Therefore, the sensors being used in this field are properly selected and sometimes modified or even exclusively developed for this task in order to achieve best performance. Independent of the sensor selection one can improve the system performance by following some rules for their proper installation and configuration as well as for the required data acquisition and processing. The most important aspects are listed in the following.

Airflow Sensor

An ideal airflow sensor measures the data listed above at one single location. The sensor should have high sensitivity to airflow modulations, a fast time response and must be insensitive to precipitation and icing.

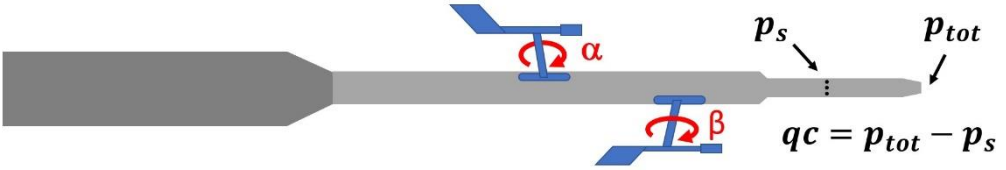

Figure 14*: Traditional flight test airflow sensors often use small boom mounted vanes which directly align with the airflow direction. The setup usually includes the measurement of static and dynamic pressure by means of a pitot static tube ahead of the flow angle vanes.*

Due to these criteria the classical wind vanes which are often used in flight test are not suitable for airborne science. As shown in Figure 14 these vanes align with the airflow and allow to directly measure the flow angles as the orientation of the

vane. Due to the inertia of the moving parts the time response is poor, the sensor does not work properly under icing conditions and the resolution in the measurement of the vane orientation angle is relatively low.

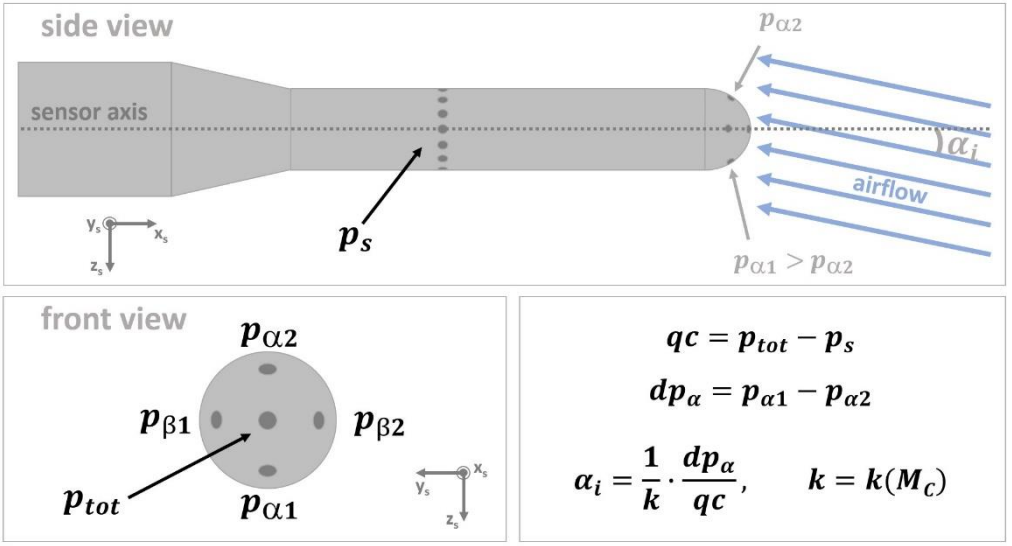

Figure 15*: Airflow sensor based on the five-hole measurement principle. The sensor determines the flow direction α_i relatively to the sensor x-axis (x_s) from the pressure difference between two pressure ports which are symmetrically located on a half-sphere along the vertical axis z. The sensor also includes a measurement of the lateral angle β_i as well as of the static (p_s) and total pressure (p_{tot}). The calculation of flow angles from the pressure data is based on a Mach Number (M_C) dependent calibration coefficient which has been determined in wind tunnel experiments.*

Today, the established standard for research applications aiming at precise and fast airflow measurements on aircraft are flow probes which are based on pressure measurements as depicted in Figure 15. The idea is to measure the symmetry of the pressure distribution on a half-sphere which is placed in the flow. Any angular offset from the sensor axis will lead to a non-symmetric pressure distribution which is detected as a differential pressure between two opposite pressure ports

which are symmetrically located on the sphere along the sensor main axes y_s and z_s. As a consequence, this kind of flow sensor (5-hole probe) requires a pressure sensor instrumentation which is connected via tubes with the pressure ports on the probe.

The ideal location for any airflow sensor is in the front of the aircraft on the centerline in order to be symmetric to the flow and pressure distribution around the aircraft. However, on single engine aircraft this solution is not feasible and the sensor must be attached to the wing [11].

An important improvement is the usage of a nose boom in order to place the sensor ahead of the aircraft nose. The idea behind this is to minimize the aircraft impact on the measurement i.e. to place the sensor outside of the aircraft influence on pressure distribution and airflow deflection. It is also common that the boom is inclined with respect to the aircraft x-axis in order to compensate the mean angle of attack thus aligning the sensor with the mean airflow. This helps to minimize measurement errors of the airflow sensor which typically increase at larger flow angles.

The design and installation of a nose boom on an aircraft is challenging, since the aircraft nose is very sensible to modifications. The boom can possibly interfere with important aircraft sensors like the pitot static probe, the angle of attack vane, temperature sensors or the weather radar. Flight test often accepts that the weather radar is not needed for the actual flight trials. In this case the radar is removed and the respective space is used for the boom installation. It is obvious that this solution is not acceptable for a permanent boom installation on an operational research aircraft.

However, the main challenge for the installation of a nose boom on an aircraft is aeroelasticity. The main design goal for any nose boom installation is maximum stiffness of the installation. This concerns the boom itself (i.e. its Eigenfrequency) as well as the interface into the aircraft structure. A “weak” installation not only has an influence on the airflow data itself but also puts the complete aircraft at risk:

- The boom installation has a specific Eigenfrequency which can be excited by the airflow and lead to serious damage or disintegration of the whole installation during flight. The weight of the sensor installation at the nose boom tip further boosts this effect.
- A vibration of the nose boom will degrade the airflow data. The respective motion of the boom tip leads to an artificial signal in the flow angle signal. According to Equation 2 this modulation will be interpreted as a wind modulation since the IRS is not able to detect and compensate this motion.

It is important to note that any boom installation has a specific Eigenfrequency and will always show this effect. Therefore, the design of a nose boom installation always represents a compromise between the acceptable level of vibration and the minimum acceptable boom length (i.e. the maximum acceptable aircraft impact on the data). The existing aircraft structure in the nose section also creates limits for a stiff connection between airframe and boom. Modern nose booms are composite structures designed to achieve maximum stiffness at minimum weight. It turns out that a 20Hz Eigenfrequency represents an ambiguous goal which is achieved only by very few examples.

One disadvantage of a nose boom arises from the fact that the respective pressure sensors are usually located inside the aircraft nose and must be connected with the airflow probe via tubes which have a significant length. These tubes cause resonance and dampening effects which can seriously degrade the data quality of the flow measurement.

In order to avoid this problem some research aircraft use the aircraft nose itself as the airflow sensor by placing 4 pressure ports symmetrically around the typical location of the stagnation point. This solution is also required when a boom cannot be installed due to structural or space limitations in the aircraft nose section. The advantage of this configuration are shorter pressure lines and the absence of any artificial fluctuations in the flow angle signal caused by sensor (boom) vibration. However, this solution creates other problems. Since an aircraft nose is not a perfect sphere the calibration coefficients for this flow sensor are non-symmetric and must be determined individually for each flight state. The

static pressure errors are also very large at this location and the dynamic pressure measurement is challenging since the stagnation point will move with changing flight conditions. Due to the weather radar which is directly behind the pressure ports the construction must not use metal parts. However, the most serious disadvantage is the fact that it is not possible to measure the static pressure with this configuration at the probe itself.

Inertial Reference System

The second important data source is the inertial reference system. These systems have been developed as standard aircraft instrumentation and any large aircraft has at least one of these instruments onboard. In the past it was a common practice to either use the available basic aircraft IRS or to install such a standard avionic component as scientific instrumentation. These systems are reliable and rugged but they must be treated as black boxes. Their data interface is a standard avionic serial port (ARINC429), data rates are fixed and not the same for all available parameters. There is no control or insight about how the data is generated. Details on internal data handling and filtering are typically not available and the exact timing is not clear.

Over the last years internal reference platforms were often used by science to monitor and characterize the motion and attitude of vehicles (airborne and ground based) in order to describe the orientation and location of the platform itself or of sensors mounted on these platforms. One example is airborne photogrammetry or earth observation experiments on aircraft. These applications triggered the development of an own class of IRS. These instruments usually combine two data sources: high frequency data from accelerometers and fiber optic gyros and the slow but precise and drift free data from a global navigation satellite system (GNSS) like GPS. A Kalman Filter is used to generate a data product from these two sources which is fast and precise. These systems are often very compact. They provide an exact timing (real time data), high data rates and more common data interfaces like Ethernet.

Many of these instruments additionally offer post processing techniques which can significantly improve the GNSS data quality by using correction data which becomes available typically some days after the measurement. The usage of post processing techniques leads to an extreme accuracy in the data.
For wind measurements on aircraft the IRS should be placed as close as possible to the airflow sensor. By doing so the error of the rotational speed component $\vec{v}_{rot} = \vec{\omega}_a \times \vec{R}$ depicted in Figure 12 is reduced since a large $\vec{R}$ will always magnify any existing measurement error of $\vec{\omega}_a$. Another reason for a close installation between IRS and airflow sensor is the rigidity of the connection between them. If the IRS and the flow sensor are mounted at a large distance the airframe cannot be seen as a rigid structure any more especially during flight maneuvers with significant load factors or turbulent atmospheric conditions.
It is highly desirable that the IRS is aligned with the aircraft axes especially when real time data is required during a flight test and in order to simplify data interpretation and visualization.
However, for wind measurements it is the relative orientation of the airflow sensor with respect to the IRS which is of interest. The respective angular offsets are subject to the calibration procedures described in this work.
This means that the exact adjustment of the IRS with respect to the aircraft axes is not critical for a wind measurement. Deviations between IRS and aircraft orientation will not affect the precision of the wind calculation. The IRS coordinate system defines the "aircraft".

Temperature Sensor

According to Equation 3 a temperature measurement T_s is needed for the calculation of TAS.
Temperature measurements on aircraft are difficult due to the disturbed temperature field around an aircraft, the strong airflow and the impact of raindrops and ice particles. Therefore, precise temperature measurements are usually based on the determination of the Total Air Temperature (TAT). The respective sensors use housings which separate particles (like rain and snow) from

the airflow and which are designed to significantly slow down the airflow in order to achieve an adiabatic heating of the air which is very close to the max value (of air at rest) called the Total Air Temperature. Since a certain flow through the housing is needed for obvious reasons the real temperature is always below the theoretical TAT value. This means that the measured temperature has to undergo a correction called the "Recovery Correction".
TAT measurements have the advantage of being independent of the location on the aircraft as long as they stay outside the aircraft boundary layer. In the disturbed pressure field around the aircraft a higher temperature is always correlated with a slower flow i.e. a lower adiabatic heating. The combination of these effects always leads to the same TAT independent of the probe location.
However, TAT sensors should be located in the aircraft forward fuselage or aircraft nose in order to have a shallow boundary layer and to probe the same air volume as seen by the airflow sensor thus avoiding time shift corrections to the temperature data.

Response Time and Synchronization

The time resolution of the measurements and the speed of the aircraft define a spatial resolution of the data which must satisfy the research requirements. This time resolution is not only depending on the data acquisition rate but also on the time response of the sensors being used. Especially the air data sensors have a limited time response which typically depends on air density (flight altitude) and aircraft speed.
Temperature sensors are typically the slowest air data instruments. Depending on aircraft and flight state an open wire Pt100 resistance thermometer in a TAT housing can show time constants in the order of 50 ms. Pressure sensors are faster and have typical response times of 10-20ms. This does not consider any additional delay caused by the connecting tubes to the airflow sensor.
As a consequence, air data investigations usually chose a maximum data rate of 100Hz. On a jet like HALO with a true air speed range of 100-250 m/s this

corresponds to a spatial resolution of 10-25m, which is sufficient for most atmospheric science research including studies of atmospheric turbulence.
From Equation 2 it becomes clear that a precise measurement of wind speed requires a proper synchronization and a drift free and accurate time base for each of the data sources being involved. A drifting time base would result in an artificial wind signal since the time series of $\overrightarrow{gs}$ and $\overrightarrow{TAS}$ in Equation 2 will not be able to properly eliminate common motions any more.
Therefore, it becomes important to regularly check the different data sources for this common time base and possible time drift effects.

BAHAMAS Sensors

All experimental data presented in this report was measured by the BAHAMAS system on HALO. Therefore, the most important sensors of this system are presented in the following sections.

Airflow Sensor

BAHAMAS uses a nose boom mounted probe for airflow measurements. The sensor itself is a commercial 5-hole probe (Collins Aerospace, formerly Rosemount Aerospace 858AJ flow angle sensor, [13]) similar to the sensor which is sketched in in Figure 15. The probe is anti-iced and has pressure ports for static and total pressure as well as for the 2 directional (vertical and horizontal) differential pressures. The sensor is specified to have an accuracy of 0.2° for flow angles [13], a static pressure error of <1% qc_i for α_i between -8° to +8° and a dynamic pressure error of <1% qc_i for α_i between -10° to +10° [14].
The Rosemount 858 sensor was fully characterized in excessive wind tunnel tests by the manufacturer which cover the complete flight envelope of HALO. The BAHAMAS data evaluation uses these calibration constants which are a function of the Mach Number M_C and documented in an official report [13].
The airflow sensor is mounted on a nose boom which compensates the mean aircraft angle of attack and shows an Eigenfrequency of 19.5Hz. The HALO nose boom was designed to house the required pressure instrumentation directly

behind the airflow probe on a so called “sensor tray” inside the boom tip. This sensor tray also carries a 3-axis accelerometer which allows to monitor possible boom vibrations during flight. The complete setup is shown in Figure 16.

Figure 16*: BAHAMAS airflow instrumentation. The system uses a commercial 5-hole probe which is mounted on a nose boom. The associated pressure sensor instrumentation is located directly behind the probe on a “sensor tray” inside the nose boom. Due to this design the connecting tubes are extremely short.*

With this design HALO achieves the optimum compromise of measuring the complete pressure information ahead of the aircraft with the shortest possible connecting tubes and a design which is insensitive to icing.
However, due to the limited space on the sensor tray, the extreme environmental conditions inside the boom during flight and the required accuracy of the measurement the respective pressure sensors had to be developed by DLR exclusively for this application. The sensors are actively temperature stabilized, very small (10cm length) and light (150g). The accuracy is better than 0.2hPa for a temperature range between -70°C and +50°C which was demonstrated in an environmental simulation chamber.
In order to guarantee a precise timing the pressure sensors were designed as analogue sensors. Therefore, the main data system in the cabin is responsible for the provision of a proper timing standard. This is achieved by means of a time server which synchronizes with GPS. The data acquisition is clocked with a time trigger from a signal generator which is part of the time server. Since the accelerometer on the sensor tray is also an analogue sensor pressure and acceleration are referenced to the same time base.

Inertial Reference System

Although the basic G550 aircraft platform of HALO already uses 3 Inertial Reference Systems, BAHAMAS deploys an own experimental IRS in order to better control timing and data quality.

Position [m]	0.1-0.3
Roll/Pitch [deg]	0.05
True Heading [deg]	0.1
Data Rate [Hz]	100

Table 1: ***Accuracies of the 100Hz real time data stream of the experimental IRS in DGPS mode as specified by IGI.***

The BAHAMAS IRS was manufactured by the Ingenieur-Gesellschaft für Interfaces (IGI) in Kreuztal/Germany [2]. The AEROconrol III system consists of a compact Inertial Measurement Unit (IMU-IIe) which is the reference point for the measurement and therefore mounted as close as possible to the aircraft nose boom sensor and the Sensor Management Unit (SMU) which contains the GNSS receiver. The respective GNSS antennae is installed on the HALO upper fuselage. The SMU is part of the main BAHAMAS data acquisition system in the aircraft cabin. The IRS sensor head is certified for temperatures down to -55°C and altitudes of 55,000ft.

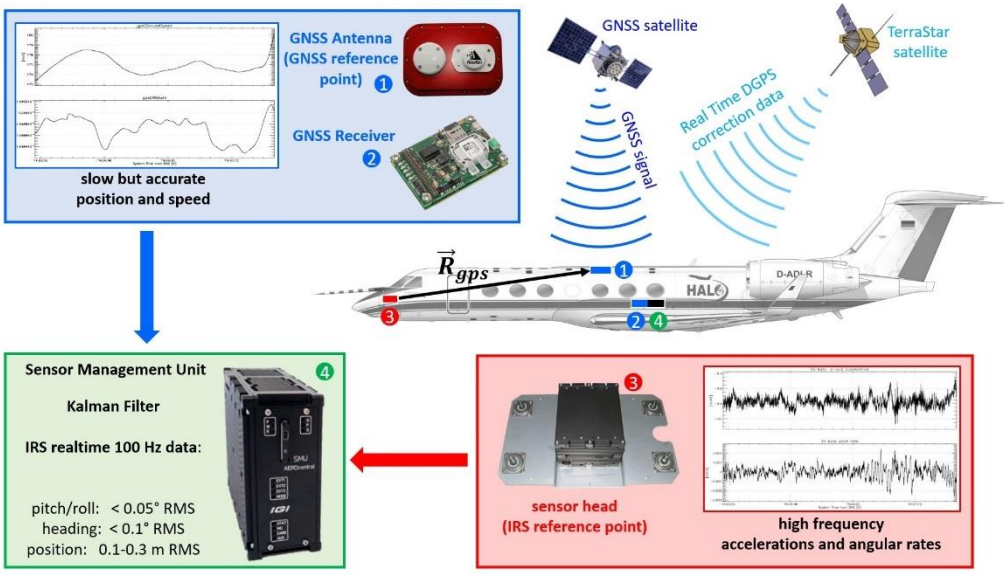

Figure 17*: Principal setup and data management of the experimental IRS by IGI. The system consists of 3 main components: sensor head, sensor management unit (which contains the GNSS receiver) and the antenna. Final data is referenced to the sensor head which is placed close to the air data probe. The system also offers a real time DGPS correction via a satellite data link.*

The system is able to provide a real-time differential GPS (DGPS) signal by using GPS correction data from a satellite data link (TerraStar) during flight as shown in

Figure 17. The real time data stream is available via a UDP interface with a data rate of 100HZ. The accuracy of this real time interface can be seen in Table 1.
A significantly better accuracy of the IRS data is achieved by data post processing using the AEROoffice Software from IGI. Figure 18 visualizes the workflow.
After the original GNSS data is extracted from the data set the post processing Software GrafNav (by Novatel) is used to calculate high precision GNSS data by using corrections which are available via the internet some days after the flight. The software can process data from different GNSS sources (GPS, GALILEO, GLONASS, BEIDOU and QZSS).

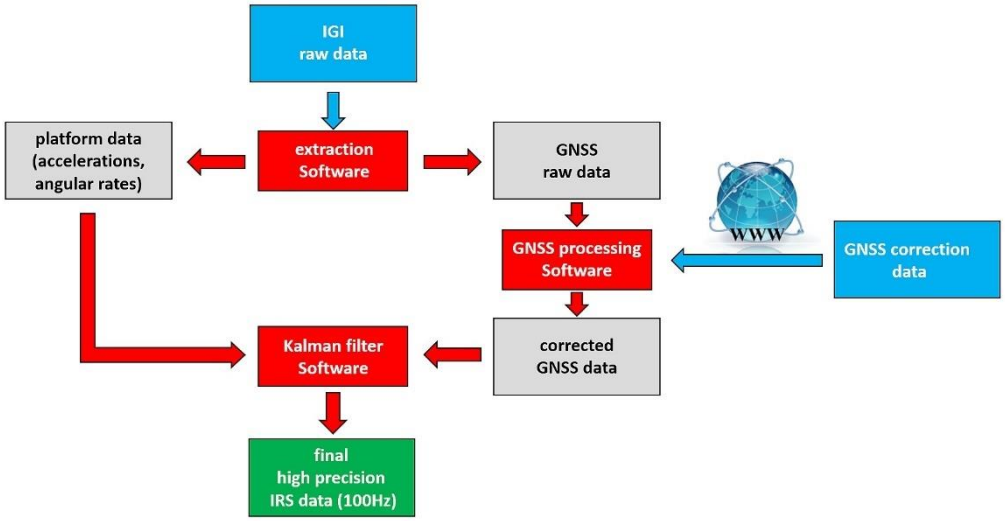

Figure 18*: Principal workflow of the processing of IRS data. After the initial raw data is extracted from the data files the GNSS data undergoes a precise post processing using correction data which is available in the internet some days after the flight. The final data is then calculated from the corrected GNSS data and the measurements of the sensor head.*

In a final step AEROoffice combines the corrected GNSS data with the IRS sensor head raw data in order to provide position, velocity and attitude of the IRS sensor head with extreme accuracy. The respective data can be seen in Table 2.

The stated accuracy has been demonstrated for aircraft measurements [ref-Cram]. However, there are indications that this accuracy depends on the flight pattern. The Kalman filter works much more efficient in presence of variations in attitude and position data. If the aircraft is flying with constant heading and altitude for a long time it is possible that the accuracy degrades somewhat from the values given in Table 2. This behavior is presently subject to further investigations. However, the IRS data used in this report always relates to test flights with many maneuvers. We can therefore assume, that the specifications listed in Table 2 are valid for this report.

Position [m]	0.05
Velocity [m/s]	0.005
Roll/Pitch [deg]	0.003
True Heading [deg]	0.007
Max. data rate [Hz]	400

Table 2: ***Performance of the AEROcontrol-III experimental IRS onboard HALO. The specified accuracies refer to postprocessed data.***

A typical error for airborne wind measurements on research aircraft lies between 0.3 and 0.5 m/s, even when a precision IRS is part of the aircraft instrumentation [11]. Keeping in mind that this measurement represents the difference of two speed vectors according to Equation 2 it becomes immediately clear, that this error can almost completely attributed to the airflow vector determination, i.e. the contribution of the IRS to the wind speed measurement can be treated as error free. The quality of the airflow measurement usually limits the accuracy of airborne wind measurements.

Temperature Sensor

The BAHAMAS temperature measurement uses a Collins Aerospace (formerly Rosemount Aerospace) deiced TAT housing (102 series, configuration B) as shown

in Figure 19. The sensor itself is an open wire PT100 resistance thermometer which can be removed from the housing for calibration or repair. The properties of the housing are well documented and the Recovery Correction and the deicing effect are well understood and documented for the complete flight envelope of any civil aircraft [6]. The respective corrections were gained during excessive wind tunnel tests by the manufacturer.

Air data calculations use temperature always as "absolute temperature" measured in Kelvin. Therefore, the relative error of temperature data is typically small and the impact of this uncertainty not very critical for the result of such a calculation especially when compared to the impact of errors from the pressure instrumentation.

Figure 19*: Total Air Temperature housing (Rosemount Model 102B) and the respective resistance thermometer (open wire Pt100). The brass cylinder around the element is a heat shield which prevents an influence of the deicing on the measurement.*

Aircraft Impact on Air Data

The goal of any air data measurement is the determination of the different parameters in the "free atmosphere" i.e. for an air volume which is not affected by any external influence like an aircraft which passes through this volume. Especially the measurement of pressure and airflow on an aircraft is seriously complicated by the fact, that the aircraft itself influences both units during flight.

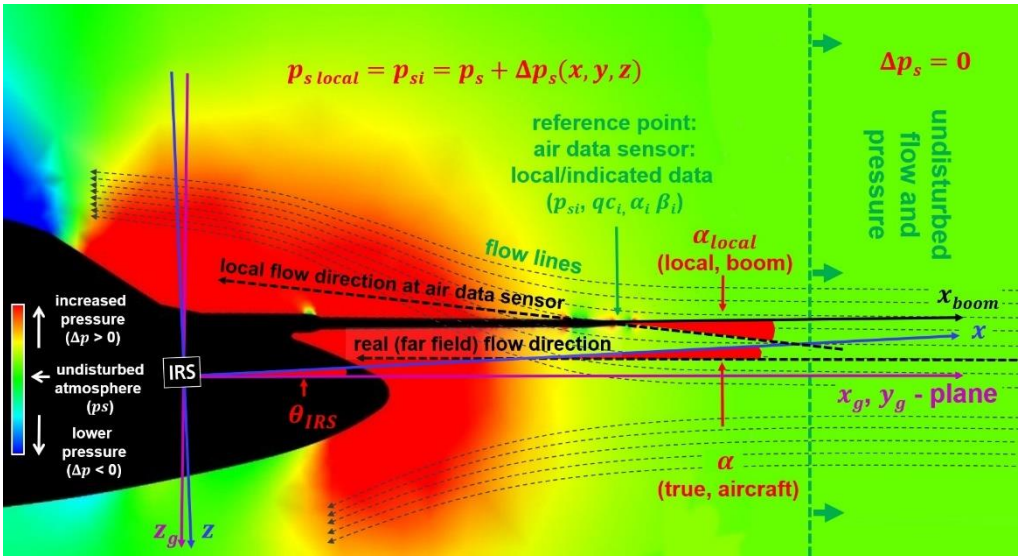

Figure 20*: Schematic view of the typical pressure field and airflow around the nose section of an aircraft during flight. The aircraft shown is equipped with a nose boom.*

Figure 20 visualizes schematically theses effects for an aircraft which is equipped with a nose boom. One can see that the boom reduces these effects by placing the airflow sensor outside the strongest perturbation zone close to the aircraft nose. But it also becomes clear that the boom tip is still influenced by the aircraft. Therefore, we have to conclude that in general it is not possible to directly measure undisturbed air data from a moving aircraft. Even a perfect air data instrumentation will only measure the local values of pressure and airflow at the

sensor location. These values are not identical to the undisturbed units one is actually looking for. In order to account for this difference, we introduce the "local" or "indicated" data (index "i") in contrast to the real values in the free atmosphere. This report will show how to determine and parameterize corrections to the indicated values in order to calculate the real air data for the free atmosphere. Please note that even calculated units like a Mach Number can be treated as "indicated" if they are calculated directly from the uncorrected values i.e. from qc_i and $p_{s,i}$ instead of qc and p_s in Equation 4. The comparison of M_C and M_{Ci} is shown in Figure 94.

Pressure Field

As one can see in Figure 20 the aircraft builds up a shock wave in front of the airframe and the indicated pressure ps_i at the air data probe differs from the value ps for the free atmosphere. The difference Δp_s between these two values is called the "static source error". An exact parameterization of Δp_s is prerequisite in order to provide a proper (corrected) pressure information for the air crew. In the vicinity of the airframe Δp_s strongly depends on the location along the fuselage. Depending on this position the value of Δp_s can become positive or negative [8]. Assuming a fixed position for the air data sensor Δp_s depends on the following parameters:

- Aircraft speed (main parameter: Mach Number M_C according to [7])
- Static pressure / pressure altitude (air density)
- Flow angles: angle of attack α and angle of sideslip β
- Aircraft state: deployment of spoilers, flaps, landing gear,..
- Flight state: maneuvers, level change, turns,..
- Aircraft configuration: aircraft weight, change of aircraft shape by external modifications like wing pods, belly pod or air intakes

The parameterization of these effects can be simplified by using "indicated values" as input parameters, since these are directly available from the data system and do not require any corrections.

The second important pressure information is the dynamic pressure qc which is subject to the same effects. The correction for qc_i is greatly simplified by the fact that outside the aircraft boundary layer the total pressure $p_{tot} = p_s + qc$ is constant [8], [17]. This means that

$$p_{tot} = p_s + qc = p_{s,i} + qc_i \qquad \textbf{Equation 7}$$

Therefore, Δp_s applies to $p_{s,i}$ as well as to qc_i but with opposite sign.

Airflow

The airflow is described by $\overrightarrow{TAS}$ which is calculated via Equation 5 which uses the flow angles α and β. It is clear that the errors in the pressure measurement of p_s and qc must have a direct impact on TAS. Due to Bernoulli's law the dynamic pressure must be lower in areas where the static pressure increases. This results in a lower true air speed.

Figure 20 also shows the aircraft influence on α_i and β_i. Since the airflow has to go around the airframe, the flow lines are deflected. Especially α_i will deviate from the free atmospheric value close to the aircraft nose. This flow line deflection is often referred to as "upwash".

The corrections which are needed to derive α and β from α_i and β_i (as directly measured by the airflow sensor) must also include an offset which accounts for the different orientations of the boom and the aircraft coordinate system (as defined by the IRS). The relation between real and indicated flow angles can in principle be influenced by the following parameters:

- Aircraft speed and altitude
- Aircraft state
- Flight state
- Aircraft configuration

Atmospheric Wind: Properties

The complete and accurate calibration of airflow data must consider the influence and properties of atmospheric wind which is "seen" by the air data probe.
Atmospheric wind describes the motion of air parcels relative to the earth. Thus, it is responsible for the mass transport of air and with this also for the transport of energy (sensible heat), moment, moisture (latent heat), trace gases or aerosols. Furthermore, wind plays a key role in the development of weather systems. During extreme weather events wind often demonstrates also its destructive potential. These examples highlight the importance of wind in atmospheric science and its undeniable need of adequate measurement.
In order to measure the wind, one needs the information about magnitude (wind speed) and direction. In meteorological discussions the horizontal wind and the vertical wind are often considered separately. The mean values of the horizontal wind are usually 1-2 orders of magnitude larger than the vertical wind. While the prior is crucial for the evolution of large scale (synoptic) weather phenomena, the latter is very important for smaller scales (i.e. cloud formation, turbulent transport). The horizontal wind can reach peak values of >100 m/s, the vertical wind will hardly exceed values of ~20 m/s. Due to mass conservation the vertical wind has to be 0 m/s when averaged over a sufficient area and time period. Thus, in a first approximation of the equations of motion for the air the wind is only horizontal. This approximation is the geostrophic wind, where the wind results from the equilibrium of the horizontal pressure gradient force and the Coriolis force:

$$u_g = -\frac{1}{\rho f}\frac{\partial p}{\partial y} \qquad v_g = \frac{1}{\rho f}\frac{\partial p}{\partial x} \qquad \textbf{Equation 8}$$

Here u_g and v_g are the horizontal components of the geostrophic wind, ρ represents the air density and f ($\sim 10^{-4}\ rad\ sec^{-1}$ in mid latitudes) the Coriolis parameter. $\frac{\partial p}{\partial x}$ and $\frac{\partial p}{\partial y}$ are the respective pressure gradients. The geostrophic wind will blow along the isobars with the low-pressure left-hand side on the northern

hemisphere. At the synoptic scale this is a very good approximation for the mean wind in the middle troposphere (a height of 5-10 km). Thus, a map of the pressure distribution at a specific height (see Figure 21b) gives information on the distribution of the wind which blows along the isobars. At regions where the isobars are lying closer together, also the wind blows stronger. The geostrophic wind has no wind component from the high to the low-pressure area. Thus, the pressure field remains unchanged and also the mean wind field is persistent. Deviations of this idealized scenario arise for example from frictional effects (especially near the ground) or horizontal temperature gradients.

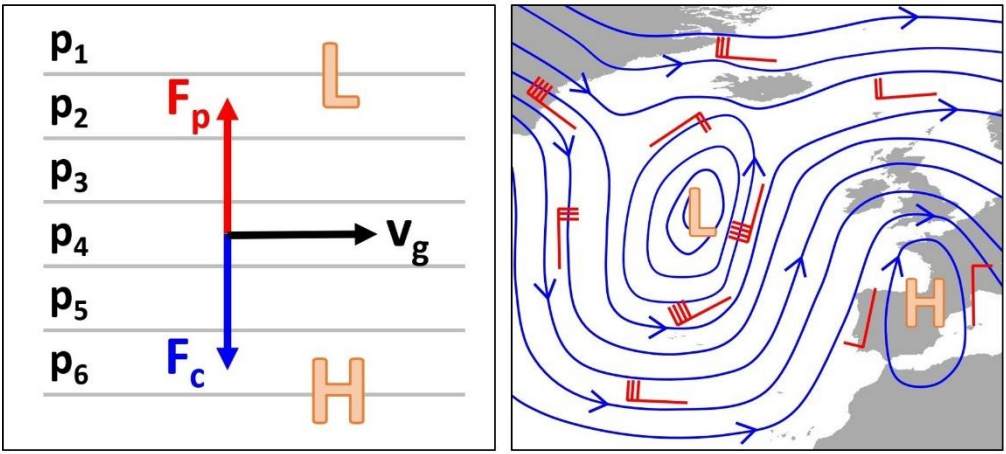

Figure 21*: Left panel: schematic view of the Geostrophic wind. The pressure gradient force (F_P) is equal in strength but in the opposite direction to the Coriolis force (F_C). The geostrophic wind (v_g) is blowing along the isobars with the lower pressure on the left-hand side on the northern hemisphere. Right panel: example pressure distribution in the free atmosphere over Europe. The blue lines represent the isobars which determine the geostrophic wind according to Eq. 8. The arrows indicate the direction of the wind which is also shown by the wind arrows (red). On the northern hemisphere the airflow around a low-pressure area is oriented counter clockwise.*

Complementary to the mean wind signal the short-time fluctuations of the wind are usually randomly distributed. In these smaller scales the turbulent motion of the atmosphere becomes visible. The statistical methods of isotropic turbulence are used to analyze the properties of the turbulent atmosphere. Turbulent eddies (bubbles) of different sizes carry out the transformation of the kinetic energy from the biggest eddies (diameter ~ 1000 m) down to the so called "Kolmogorov Scale" (diameter ~ 1mm). Finally, the energy is dissipated in molecular motion, into heat.

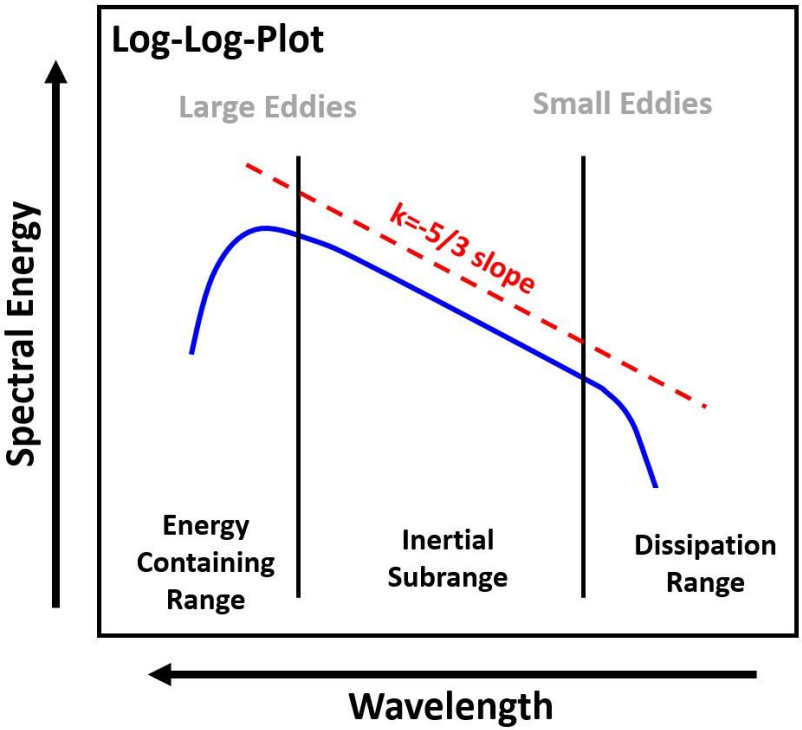

Figure 22*: Schematic view of the wind spectrum in isotropic turbulence. The largest eddies develop in the energy containing range on the left hand of the figure. In the inertial subrange the eddies are splitting up to smaller eddies which is called the energy cascade. In this range no energy is added or removed from the air parcel. The Kolmogorov Scale separates the inertial subrange from the dissipation range.*

This energy cascade is visualized in Figure 22. On the left hand of the chart the energy containing range represents the biggest scales. In this region atmospheric processes (i.e. surface heating, wave breaking, …) introduce energy in terms of motion to the turbulent eddies. Towards the smaller scales (further to the right in the Figure) no more energy is added or removed from the system. This region is called the inertial subrange. The energy is simply transferred to the smaller scales through breaking of the eddies until the Kolmogorov Scale is reached and dissipation becomes dominant. The energy distribution in the inertial subrange is very characteristic. In this logarithmic presentation the slope of the spectral energy is according to Kolmogorov (e.g. [16]) always equal to $k = -5/3$. When the atmospheric turbulence is stronger the slope of the curve still remains unchanged, it is only shifted towards higher values. The only variable is the dissipation rate, which is higher when the turbulence is stronger.

There are many examples where turbulence is a key feature of atmospheric processes. Turbulent mixing is much more effective compared to molecular mixing. Turbulent transport of heat, energy, moisture or trace gases is one of the major processes in the atmospheric boundary layer. For cloud microphysics or regions of strong wind shear turbulence has a major impact. It is obvious that reasonable measurements of the entire wind spectrum including also the small wind fluctuations are crucial. For airborne measurements it is a special challenge to guarantee high quality wind measurements for the smaller eddies of diameters even below one meter. Due to the increasing impact of the moving aircraft it requires fast sensors with minimal measurement uncertainties and a perfect inflight calibration, which controls the aerodynamic influences.

Concerning the characteristic properties of atmospheric wind for this inflight calibration experiment we can summarize that

1. Horizontal and vertical wind have different properties
2. Horizontal wind structures are driven by the atmospheric pressure field. Therefore, the horizontal wind field shows significant mean wind data with large scale spatial structures which vary typically slowly with time.
3. The mean vertical wind is zero. Significant and persisting structures larger than 1-2km are only common as wave motions (gravity waves), cloud evolvement or thermal heating processes.
4. The spectra of both wind components show contributions over a wide wavelength range. For a fast-moving platform like an aircraft the spectral properties of wind can also be treated in the frequency domain.
5. Towards high frequencies the power spectra of horizontal and vertical wind speed follow a $k = -5/3$ slope which is associated with isotropic turbulence

Calibration Strategy

Calibration is the comparison between the indicated measurement of a sensor with a reference instrument which is able to provide the "real" value with high precision. This reference or "transfer standard" is usually a precision instrument with small measurement uncertainties. These must be confirmed regularly by an official calibration laboratory or the national bureau of standards.
It is obvious that for an aircraft in flight a respective air data reference instrument or measurement does not exist, especially since the atmosphere around the aircraft is significantly disturbed and the aircraft is moving very fast. Therefore, special techniques are required to provide this kind of reference data:

- Special instrumentation can be used to provide a reference measurement at a sufficient distance from the aircraft. This is the case for the Trailing Cone method in static pressure calibration or ground based instrumentation in tower fly-by experiments.
- Another way is to use maneuvers to artificially generate reference air data signals which can independently be calculated directly from the maneuver parameters.
- The third possibility is to use known properties of the natural air motion (i.e. wind). The plausibility of calculated wind data is used to correct the airflow data used for the wind calculation.

All three options are "in flight calibration techniques" and all three were used in the calibration of the HALO airflow probe.

Principal Considerations

In general, the calibration of a single air data parameter is valid for a fixed combination of the relevant input parameters. As described above the static source error is principally influenced by Mach Number M_C, pressure altitude, angle of attack α and sideslip β, flight state, aircraft state and aircraft configuration.
It is clear that a pressure calibration for the complete input parameter matrix would require a tremendous flight test program in order to cover all possible

combination of parameters. This report will show, that some of these parameters have only a very small impact on the calibration data, a few ones can be ignored completely. In meteorological research for example the aircraft state is not relevant since measurements are usually performed with an aircraft where flaps, spoiler or gear are not deployed. The same is true for flight state as long as measurements are performed for straight level flight only. However, it is always necessary to cover the entire aircraft flight envelope in terms of speed and height in order to get a complete calibration.
One way to handle the flight envelope and aircraft configuration matrix is to always combine a respective measurement with a calibration procedure for the chosen flight conditions.

Dynamic and Static Calibration

The inflight calibration of air data probes in atmospheric science knows two different types of calibration: static and dynamic calibration [11] which are explained in the following.

Static Calibration

A static calibration is a classic calibration as known from metrology. A known reference signal is applied to the sensor and the corresponding response of the device is detected. This procedure is repeated for a representative number of test points which cover the expected sensor data range. The relation between reference signal and sensor response is called the calibration curve which is then parameterized in order to be applied to the sensor indicated data during any measurement.
This kind of calibration is called static, because the reference signal is constant for a single calibration test point. Therefore, the reference signal as well as the sensor response can be averaged in order to improve the statistical noise of the measurement. A test point for the static calibration of β on an aircraft is achieved by flying a constant angle of sideslip for an adequate time (“steady sideslip

maneuver") and monitoring the airflow sensor indicated value β_i. The plot of β over β_i over all test points of this calibration then yields the calibration curve.

Dynamic calibration

The calibration of airflow sensors in atmospheric science knows a second kind of calibration which investigates the sensor response to an input signal which is dynamic i.e. not constant in time. In order to simplify the data analysis, the variation of the input data is chosen to be a harmonic oscillation which leaves a characteristic signature in the time series of any unit and can thus be easily detected. This harmonic variation in the airflow sensor input signal is achieved by flying respective maneuvers. Two kind of maneuvers have proven to be important: yaw and pitch oscillations. They generate an oscillating flow angle input signal (α_i or β_i) at the airflow sensor. If one calculates wind data during this maneuver it becomes immediately clear that the wind data must not show any oscillation since the atmosphere is completely independent of the aircraft motion. In other words: all contributing terms in the wind Equation 2 including Equation 6 are expected to show the harmonic oscillation from the maneuver input but the addition of these terms must cancel out the artificial modulation.

In case of real aircraft data, it is expected that the signature of the harmonic sensor input signal will always be found to some extend in the final wind data. In order to assess this effect D.H. Lenschow and P. Spyers-Duran have defined a threshold to evaluate the measurement system [10]. They postulated in case of the pitch oscillations that "the system performance is judged to be satisfactory if the vertical air velocity error is less than 10% of the vertical airplane velocity for the pitch maneuver". We will refer to this definition throughout this work as the „Lenschow Criterion ".

In the past the dynamic calibration was often treated as a functional test of the complete measurement system. Timing problems (unknown or varying delays) between the different input data sources in Equation 2, a wrong lever arm $\vec{R}$ in the calculation of $\vec{v}_{rot}$, systematic errors or delays in the IRS data during maneuvers will all result in an artificial harmonic modulation of the calculated

wind signal. However, we will show in this report that for a proper experimental setup with a precision IRS and a good timing concept of the data acquisition the residual harmonic variation of the wind data can completely be attributed to airflow sensor behavior. This can be treated by an additional correction term for the airflow sensor data which completely eliminates these effects. Therefore, the dynamic maneuver method must be treated as a real calibration rather than a system test.

Required Steps

The following tables summarize the calibration effort for an airflow sensor on an aircraft. As stated above the influence of aircraft state and flight state were not completely characterized, since atmospheric research usually doesn't require this information.

	Pressure Calibration Matrix					
	static calibration				**dynamic calibration**	
input parameter	M_{Ci}	$p_{s,i}$	α_i	β_i	α_i	β_i
basic calibration	+	+	+	+	+	+
diff. a/c state	o	o	n/a	-	-	-
diff. a/c config	o	o	n/a	-	o	o
diff. flight state	-	-	n/a	-	-	-
a/c envelope coverage	+	+	n/a	+	+	+

Table 3: ***Suggested calibration effort and HALO status for a complete parameterization of the pressure corrections (+: completely covered by this report, o: partly checked, - : not checked)***

Since the angle of attack on an aircraft is completely controlled by aircraft speed and altitude for a given aircraft configuration, the direct calibration of the static source error as a function of α_i is not possible. However, as shown later in this report the dynamic calibration of α yields an α_i dependency of ps.

	Flow Angle Calibration Matrix (α,β,γ)			
	offset to IRS	static calibration	dynamic calibration	
input parameter	(n/a, n/a, n/a)	$(\alpha_i, \beta_i, \gamma_i)$	$(\alpha_i - \alpha_{trim}, \beta_i, \gamma_i)$	M_{Ci}
basic calibration	(+, +, +)	(+, +, n/a)	(+, +, n/a)	(+, +, n/a)
diff. a/c state	(n/a, n/a, n/a)	(o, -, n/a)	(-, -, n/a)	(-, -, n/a)
diff. a/c config	(n/a, n/a, n/a)	(+, o, n/a)	(o, o, n/a)	(o, o, n/a)
diff. flight state	(n/a, n/a, n/a)	(o, -, n/a)	(-, -, n/a)	(-, -, n/a)
a/c envelope coverage	(n/a, n/a, n/a)	(+, +, n/a)	(+, +, n/a)	(+, +, n/a)

Table 4: ***Suggested calibration effort and HALO status for a complete parameterization of the flow angle corrections (+: completely covered by this report, o: partly checked, - : not checked). The dependence of the dynamic calibration on the indicated Mach Number M_{Ci} is explained later in this report.***

The flow angle calibration includes the angle γ which describes the rotation around the aircraft x-axis. For the wind calculation only the offset of γ with respect to the IRS axes is of interest. An offset in γ means that the pressure ports $p_{\alpha 1}$ and $p_{\alpha 2}$ in Figure 15 are not oriented vertically above each other (i.e. $p_{\beta 1}$ and $p_{\beta 2}$ not horizontally).

The following we will present the calibration of the HALO airflow sensor in flight. The goal is to cover all points listed in the "Pressure Calibration Matrix" and "Flow Angle Calibration Matrix" listed above.

Inflight calibration: Preparation

Laboratory calibration

As described above the airflow determination on HALO is based on pressure measurements performed on a five-hole probe. It is immediately clear that the quality of this measurement strongly depends on the accuracy of the pressure instrumentation. The most important contribution to this error is the primary calibration of the pressure sensors.
All pressure sensors used in this experiment were calibrated using a Ruska 7750i Air Data Test Set (ADTS) [4].

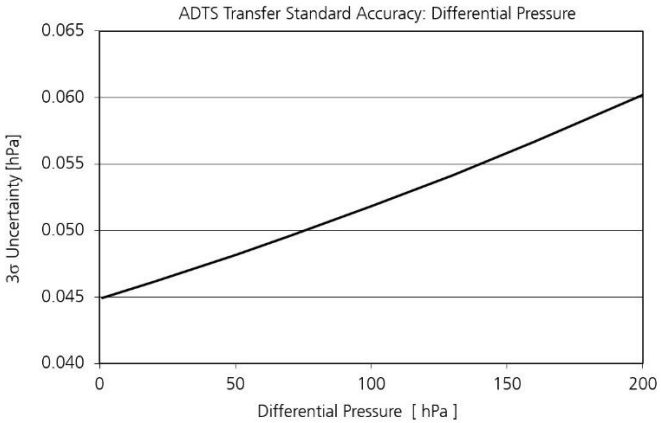

Figure 23: ***Total uncertainty of the pressure transfer standard Ruska 7750i from [4] for differential pressure calibration. Total uncertainty is defined as the 3σ combined uncertainty of linearity, hysteresis, repeatability, thermal effects one-year drift stability and the uncertainty in the primary standard, which includes the uncertainty from the national standard.***

The instrument accuracy for a differential pressure calibration with this instrument can be seen from Figure 23. Figure 24 shows the result of the calibration of the nose boom differential pressure sensor for the flow angle α_i. A similar plot for a static pressure calibration and the ADTS absolute pressure accuracy can be found in [5].

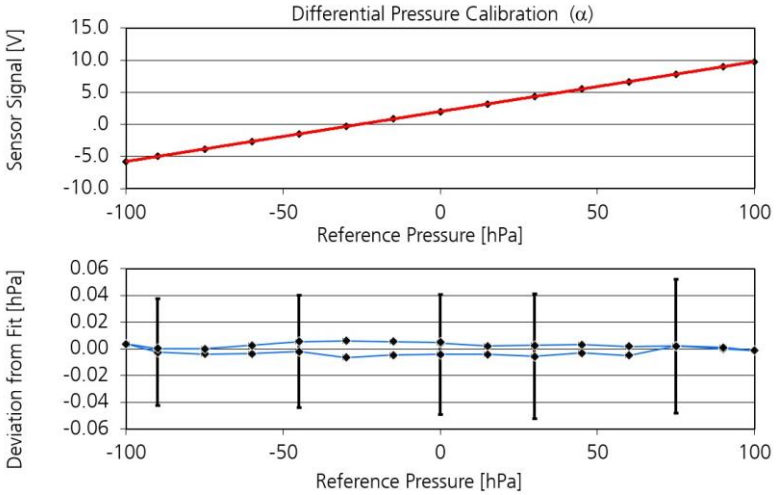

Figure 24*: Result of the differential pressure calibration of the pressure sensor for the flow angle α_i.*

The calibration of pressure sensors is always performed as a true end to end calibration which includes the data acquisition analogue to digital conversion. This means that all sensors are calibrated while already installed on the aircraft. An adequate number of calibration reference points and frequent calibrations (before and after the experiment) help to eliminate some of the major sensor error sources like non-linearity and drift.

In general, pressure sensors are sensitive to environmental conditions:

- Aircraft accelerations which act on the sensor membrane will distort the signal. This effect can be minimized by choosing an appropriate sensor orientation: accelerations along the aircraft x-axis are much smaller than the lateral ones.
- Temperature changes have a strong impact on the material properties of the pressure sensing membrane of the sensor. There are two ways to treat this effect. The temperature at the sensor can be measured and used to correct the original measurements digitally. The second possibility is to actively control the temperature of the sensor with a heating element.

Especially for changing temperatures the active temperature stabilisation turns out to be the better solution.

The pressure sensors on HALO are oriented with the membrane pointing along the x-axis. The sensors are temperature controlled to about 60°C with an accuracy significantly better than 0.1°C. Their performance hast been excessively checked in an environmental simulation chamber between -70°C and +50°C. The temperature of the sensing element is also monitored and stored during flight.

Data Acquisition: Timing Checks and Spectral Analysis

As pointed out above a proper timing concept of the data acquisition is critical for airflow measurements especially since the required data is generated by completely independent systems - each of them having its own timing concept. One of them is the analog to digital conversion of the BAHAMAS main data acquisition system which stores the analogue (real time) data from the pressure and temperature sensors installed in the aircraft nose. The other system is the IRS which acts as a complete autonomous system with an independent timing and data processing chain. Any drift or offset would result in erroneous wind data since common contributions in Equation 2 caused by aircraft motion will not properly cancel out any more. According to the HALO data rate of 100Hz the required accuracy of the time base in each measurement must be better than 10ms for a flight of 10 hours duration.

The time base of the experimental IRS on HALO is GNSS (GPS) time. Since the GNSS data is an essential contribution to the IRS data processing scheme the respective time is precisely monitored and stored.

The BAHAMAS system uses a commercial time server (Meinberg Lantime M300) which is constantly synchronized to GPS time during the whole measurement. Part of the time server is a programmable signal generator which provides a 1kHz clock signal and a pps trigger. The 1kHz signal is used as a hardware timing source for the data acquisition which builds an internal clock with this signal.

However, the timing between these two data sources must always be checked for each flight during the BAHAMAS data processing. An offset can easily be detected

by comparing the data from the accelerometers on the nose boom instrument tray with the accelerations as recorded by the IRS. This comparison is performed by means of a cross covariance function (CCF) as shown in Figure 25. Drift effects would become visible as a variable time difference between the two time series during a single flight.
In case of HALO no time drift and no time offsets in any data can be detected. Therefore, **no timing corrections** were applied to any parameter used in the following investigations.

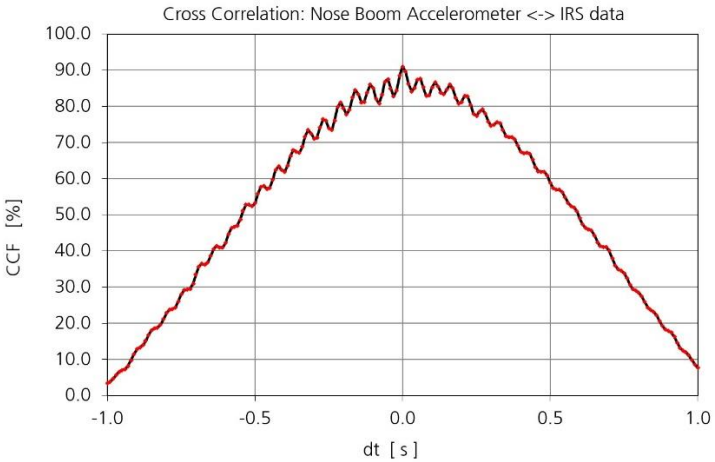

Figure 25*: BAHAMAS timing check. Cross correlation between 100Hz data from the accelerometer on the nose boom sensor tray and the respective data from the IRS. The maximum is found at dt=0s.*

The second important timing check concerns the spectral analysis of the time series. As an example, Figure 26 shows the power spectrum of the indicated vertical flow angle differential pressure $dp_{\alpha,i}$ and the indicated static pressure $p_{s,i}$. The -5/3 decay of spectral energy can only be seen when the air volume is homogeneous along the flight path of the measurement and no large wind structures are present. When atmospheric variations are very small (high altitude, low turbulence level) instrument noise will eventually dominate the spectrum at high frequencies. It can easily be detected as a horizontal line in the power spectrum. The noise is referred to as "white noise" since the spectral energy is

constant over all frequencies ("white"). However, in many cases the white noise will not be visible at all.

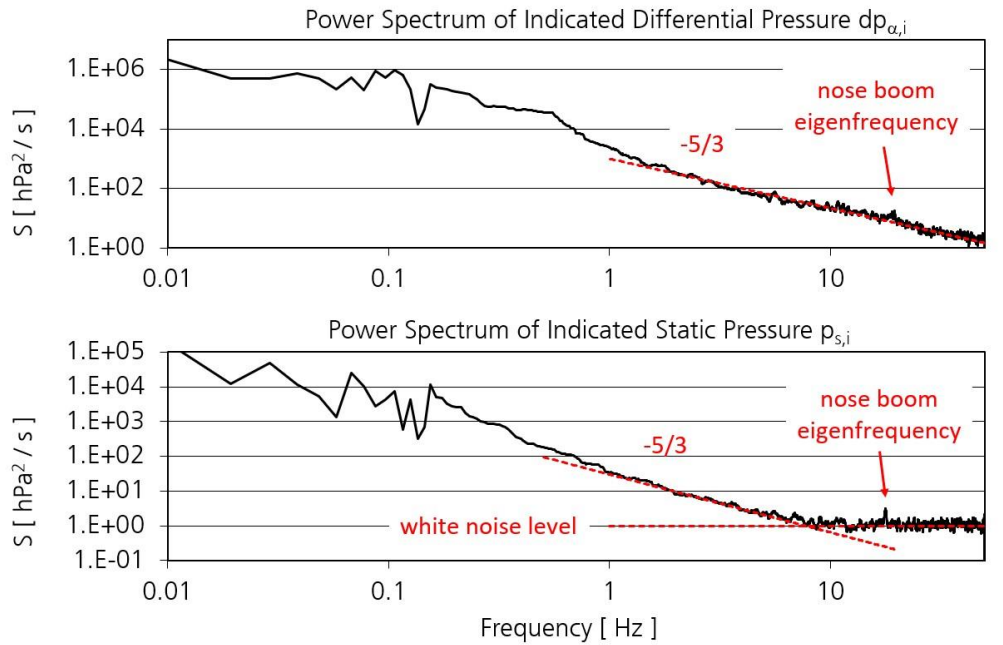

Figure 26*: Smoothed power spectra of static pressure data from the HALO airflow sensor for a flight leg of about 100s at FL430 and M_C=0.80. The data shown is the indicated differential pressure $dp_{\alpha,i}$ and the indicated static pressure $p_{s,i}$. Additional lines (red, dashed) show the expected -5/3 behavior. Due to low atmospheric variability at this altitude white noise in the static pressure signal becomes visible. In this case, the nose boom vibration is visible in the spectra.*

The same is true for the nose boom eigenfrequency but with an opposite sign: Atmospheric turbulence excites the boom vibration and leads to a characteristic peak in the pressure data. Depending on the direction of the excitation the peak becomes visible in the spectra of $dp_{\alpha,i}$ or $dp_{\beta,i}$ and very rarely in $p_{s,i}$.

More interesting than the spectra of indicated units are the respective plots for calculated units like the three wind components. These spectra will immediately indicate systematic errors, dampening effects or artificial modulations especially

at higher frequencies. Therefore, spectral analysis is an important tool in the quality check for airborne airflow instrumentation.

Static Calibration of HALO airflow sensor

Static Pressure Calibration

The calibration of the static source error on HALO was performed with the "Trailing Cone" (TC) method which is based on the assumption that undisturbed air is available behind the aircraft and that this "free atmosphere" can be accessed by means of a long tube trailing behind the aircraft. This tube is stabilized by a plastic cone the method is named after. Figure 27 shows the trailing cone deployment on HALO.

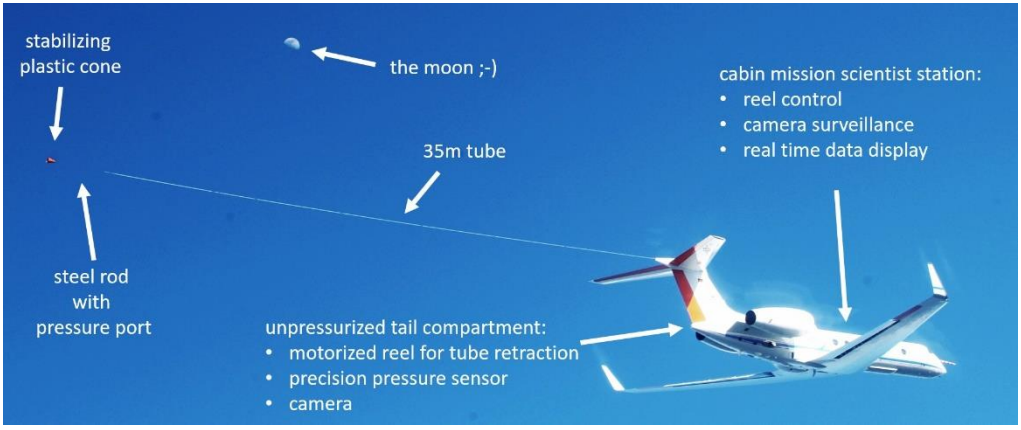

Figure 27*: Static source error calibration of the HALO nose boom air data sensor using the Trailing Cone method.*

The static pressure calibration is subject to an own report [5] which describes the method, the experimental setup, the determination of the optimum tube length, the validation of the trailing cone reference data and the final calibration of the nose boom pitot static system over the full flight envelope of HALO.
We therefore list the original result of this report only. It can be seen in in Figure 28 and Figure 29.

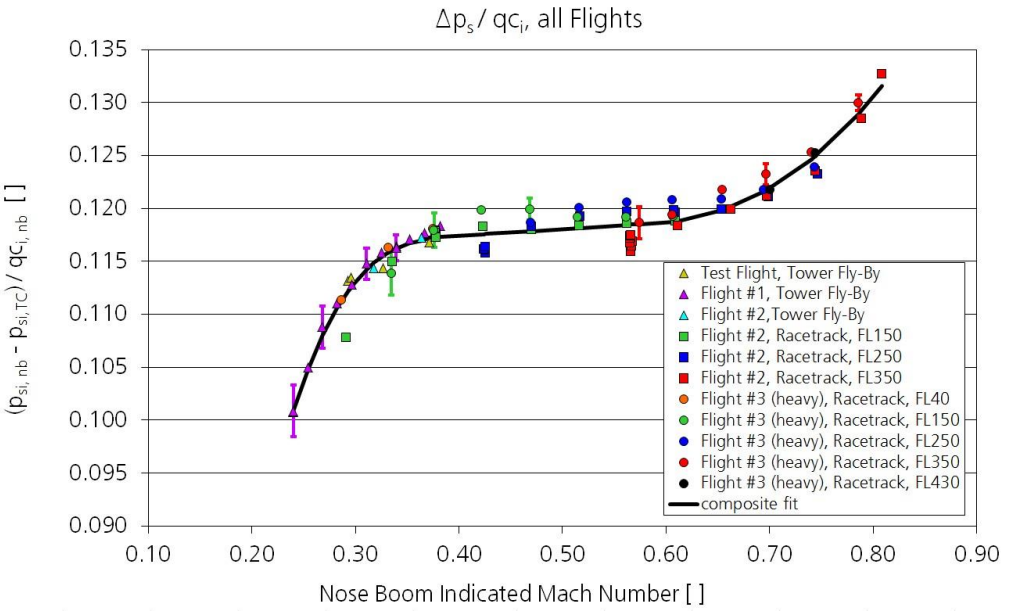

Figure 28*: Result of the nose boom static source error calibration for HALO in the clean aircraft configuration from [5]. The plot shows basically data from 3 flights: Tower Fly-By (#1), envelope expansion which was performed for a light aircraft (#2) and data taken over the complete aircraft envelope for a heavy aircraft (#3). Tower Fly-By data from an earlier test flight were added to demonstrate the repeatability of the measurement.*

As one can see the static source error is expressed as $(p_{si,nb} - p_{si,TC})/qc_{i,nb}$ where $p_{si,nb}$ is the indicated nose boom static pressure, $qc_{i,nb}$ the indicated nose boom dynamic pressure and $p_{si,TC}$ the static reference pressure from the trailing cone. This error is parameterized as a function of the indicated nose boom Mach Number M_{Ci} with a small additional correction based on indicated static pressure p_{si} and M_{Ci}. Figure 28 shows the parameterization in comparison to the measured data. The deviation of the measured static source error data from the parameterized value is shown in Figure 29. As one can see the parameterization works very well: the static source error can directly be calculated from the non-

corrected boom data with a maximum deviation of about 0.2 hPa (3σ) which is close to the instrument error of the sensors being used.
It is important to note that in the regular air data processing all input parameters must be low pass filtered in order to avoid high frequency contributions to the static source error correction.

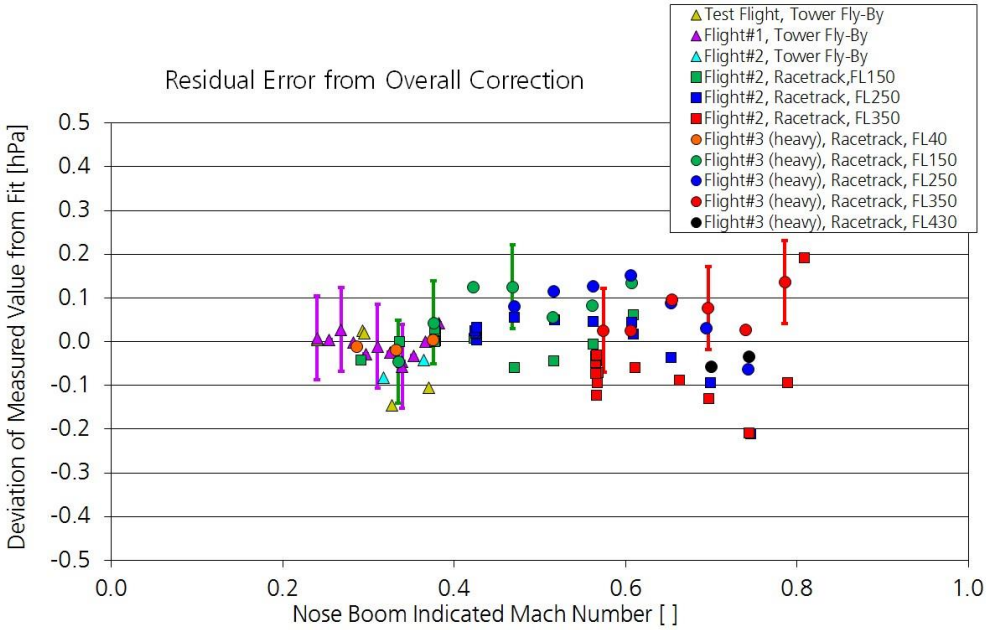

Figure 29*: Deviation between the static source error as measured directly by the Trailing Cone and the value which is calculated from indicated Mach Number and indicated static pressure from the parameterization which is shown in Figure 28. The plot from [5] contains data from test flights performed with a "light" and "heavy" aircraft configuration over the full aircraft envelope*.

The flight test plan for this experiment covered the complete aircraft flight envelope from slow tower Fly-Bys to the highest possible Mach Number of 0.88 at flight level FL350.

The experiment concerned different aircraft configurations like heavy and light aircraft. The trailing cone was also used to investigate the influence of the HALO belly pod installation on the aircraft avionic system.

Static Angle of Attack Calibration

Functional Principle

The static α calibration is based on the assumption that the **mean** vertical wind is zero. This means that the mean atmospheric flow vector has no z-component. From Figure 20 one can see that in this case the "true alpha" which is measured between "far field flow direction" and aircraft (IRS) axis is identical to the aircraft pitch θ_{IRS}. It is important to note that this comparison concerns two angles which are defined in different coordinate systems. Therefore, this assumption applies to straight level flight only. A change of flight altitude will add a vertical flow component to $\overrightarrow{TAS}$ due to the aircraft vertical motion in the atmosphere. For similar reasons the comparison does not apply during aircraft turns, where the airflow conditions are even more complicated.

Static α calibration from flight test

Figure 30 shows the result of the static α calibration for different aircraft configurations. The data comes from the trailing cone experiments (static pressure calibration) which means that the complete aircraft envelope is covered (pressure height and speed). Each data point represents a 1-2minute average which was estimated to be sufficient in order to eliminate all relevant scales of vertical wind structures.

From the plot one can see that the relation between α_i and θ_{IRS} can be parameterized by a linear fit. With the exception of the flaps/landing gear configuration different aircraft configurations lead to linear fits which are almost parallel. Aircraft weight does not seem to play a role which can be seen from Figure 31.

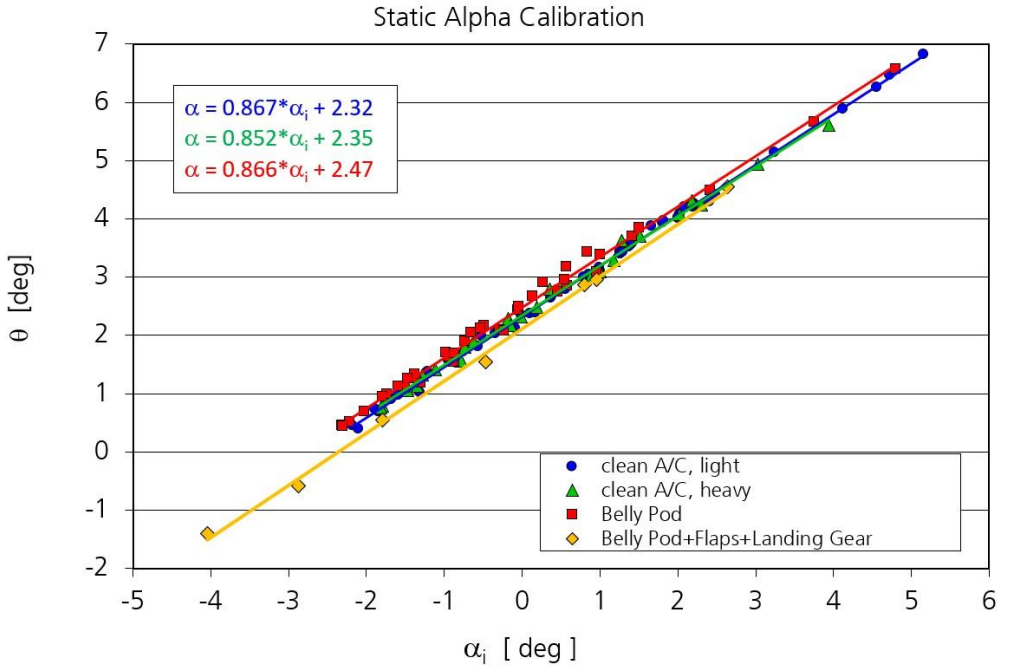

Figure 30*: Static alpha calibration. Each point represents a mean value over 1-2 minutes. The plot of aircraft pitch over indicated angle of attack can be parameterized by a linear fit. Different aircraft configurations are shown which result in individual calibration coefficients. The data covers the complete HALO envelope with Mach Numbers between 0.3-0.88 and aircraft altitudes between ground (Tower Fly-Bys) and FL430.*

The visible offset between α_i and θ_{IRS} is mostly due to the nose boom orientation (i.e. its offset from the aircraft x-axis). As a consequence, one can nicely see that the indicated airflow direction is almost centered around $\alpha_i = 0$.

From Figure 30 and Figure 31 we can also conclude that the α calibration is independent of aircraft speed and altitude (static and dynamic pressure). The 2σ accuracy of the static alpha calibration was found to be 0.15°.

In the following the calibration coefficients from this flight test are always used to calculate a "real" α_c from the indicated values α_i. However, as we see later in the document additional corrections apply to get the final value of α.

One problem arises from the fact that the relative orientation between the IRS, the nose boom and the airflow probe can change. Especially the removal of these components during maintenance or calibration can lead to a slightly different orientation after reinstallation.

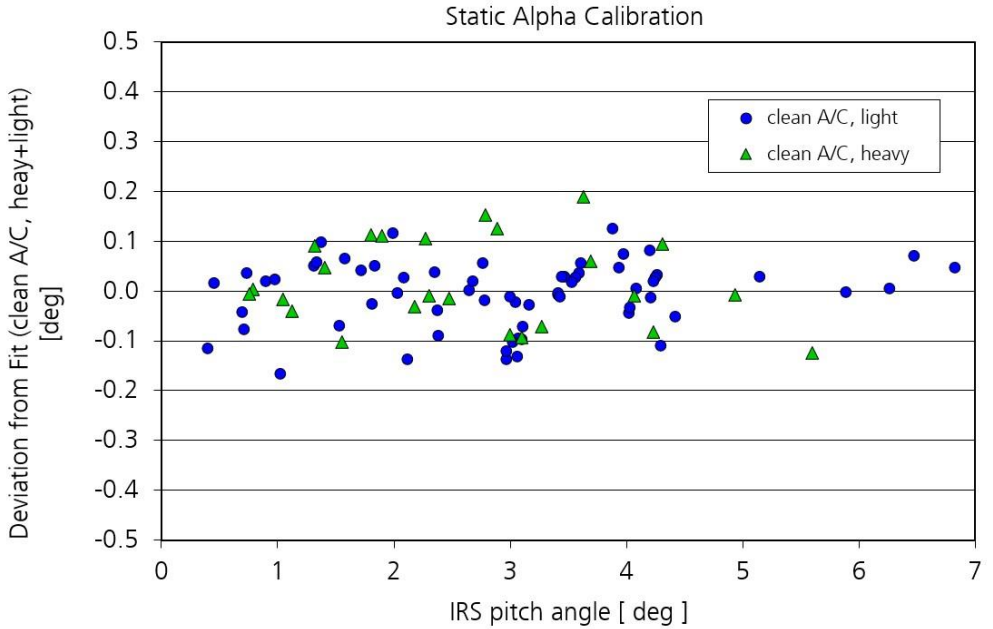

Figure 31*: Deviation of the experimental data from the parameterization of the static α calibration in* Figure 30*. A single linear fit was used for the "light" and "heavy" configuration. The 2σ error of the data shown is 0.15°.*

Therefore, a periodic check of the angular offsets of α, β and γ is necessary to avoid systematic errors in the airflow data. It turns out that for the HALO sensor α and β are more critical than γ.

Static α calibration from regular flight data

In principle the static α over Θ calibration should be possible for each flight as long as only straight level flight data is being used. Therefore, a respective "per flight" calibration has been established within the BAHAMAS data processing. The

software analyzes the flight and automatically identifies straight and levelled flight segments with a suitable minimum length. The relevant parameters in this search are aircraft vertical velocity vv and roll angle ϕ. For this subset of flight data one can then perform the same calibration procedure as demonstrated above.

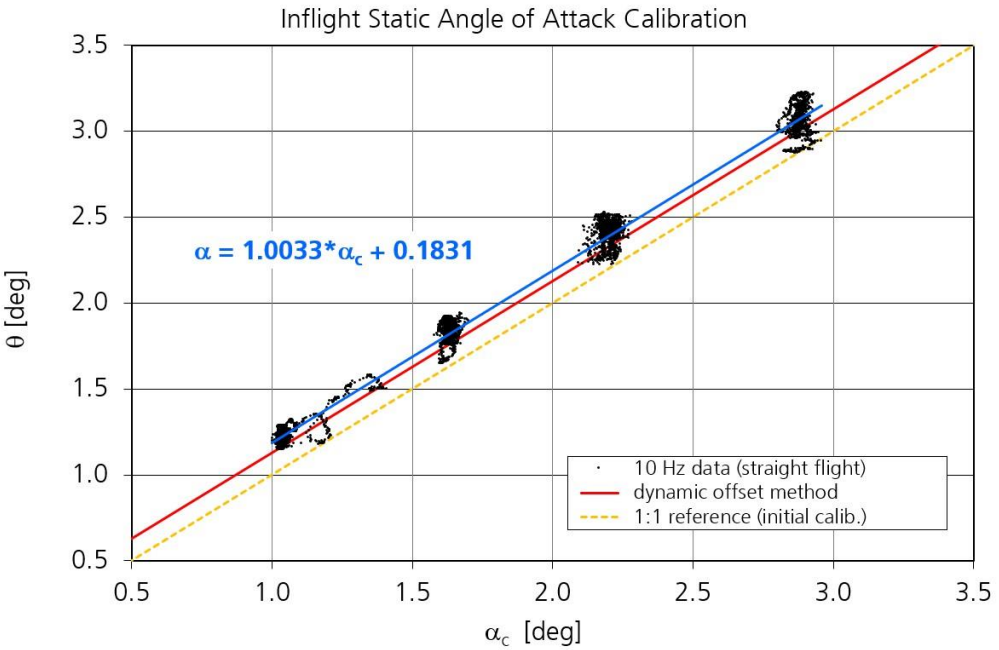

Figure 32*: Static angle of attack calibration for a research flight with dynamic maneuvers. The plot of θ_{IRS} over α_c shows only data for straight and levelled flight segments which are selected by the software. The data points represent 10Hz data. Therefore, the influence of atmospheric wind fluctuations broadens the curve. The red line shows the result of the dynamic offset method which is described later in the document.*

Figure 32 shows the result for one of the calibration flights from this project. Due to the fact that the plot shows 10Hz data one can see a broadening in the data caused by atmospheric wind fluctuations. However, the fit into the data confirms the straight-line slope which was found in the initial α_i calibration with the trailing

cone data while the angle between airflow probe and IRS shows an offset from the previous result.
Figure 32 also shows an additional calibration line which is the result of the "dynamic offset method" which will be described later in this report. Both inflight calibrations (θ_{IRS} over α_i) and dynamic offset are performed for each HALO flight in order to achieve maximum accuracy in α.
However, the 2 methods have their limitations: The θ_{IRS} over α_i fit only works well if there is enough data to perform the fit and if the available data covers an adequate data range that the fitted slope is representative.

Pressure dependency on static alpha

The question whether static pressure depends on the angle of attack is difficult to answer since the static source error is a function of aircraft speed (Mach Number) which directly controls α. This complicates the data interpretation because it is difficult to distinguish to which extend these parameters actually influence the indicated static pressure.
As mentioned above the parameterization of the static source error involves two steps: The major contribution is a function of indicated Mach Number as can be seen in Figure 28, which contains the respective fit as a black line. The difference between the experimental data from a single trailing cone flight and this fit can be seen in Figure 33.
The deviations from this fit are subject to a second correction step which depends on static pressure and indicated Mach Number. However, Figure 33 indicates on the right side that this residuum could also be parameterized as a function of α_i only.

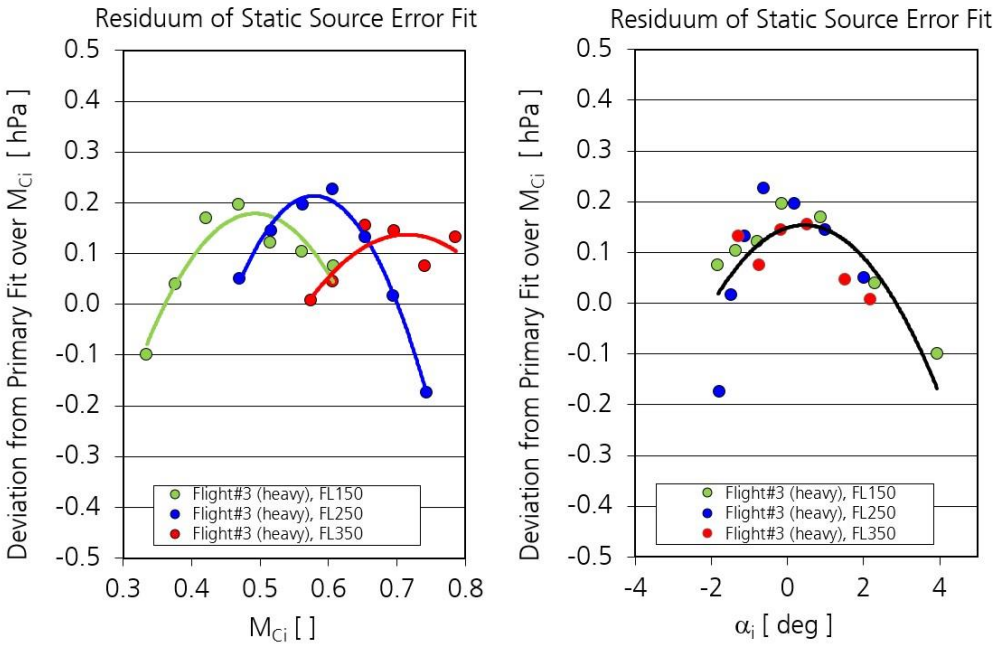

Figure 33*: Static source error calibration: Difference of experimental data from the primary parameterization of the static source error according to Figure 28. The difference is plotted as a function of indicated Mach Number (left) and indicated angle of attack (right) for a single trailing cone flight.*

The analysis for the entity of all trailing cone flights showed that the deviation of the experimental values from a parameterization over α_i was somewhat larger than than the parameterization over $p_{s,i}$ and M_i. Therefore, a direct dependency of the static source error on α_i was not considered for the pressure correction term.

Static Beta-Calibration

Functional Principle

While the α calibration by comparison to the pitch angle is easy to establish the angle of sideslip calibration during flight is more challenging. The first problem arises from the fact that the mean angle of sideslip for trimmed straight and levelled flight is zero. This means that special maneuvers are required to generate a significant aircraft sideslip. The second problem is caused by the fact that there is no direct reference for β during flight.
[11] shows how a reference value β_{ref} can be determined from aircraft data while flying steady sideslip maneuvers. The method is briefly described in the following.

Figure 34 shows the effect of a steady sideslip maneuver on the airflow and wind data measurements. As one can see the sideslip angle causes a lateral true air speed component TAS_y in the aircraft fixed coordinate system which does not exist during trimmed straight flight conditions. This component can be calculated from TAS as

$$TAS_y = TAS \cdot \sin(\beta) \qquad \textbf{Equation 9}$$

If one can determine TAS_y during the maneuver then a reference angle of sideslip β_{ref} can be calculated from Equation 9.
The determination of TAS_y can be achieved by using the wind Equation 2 for a known wind vector during the maneuver. While the wind triangle fails under these conditions the exact solution according to Equation 2 will always work - even during a sideslip maneuver. This is demonstrated in Figure 35 where both methods are compared during a steady sideslip maneuver with different values for β.

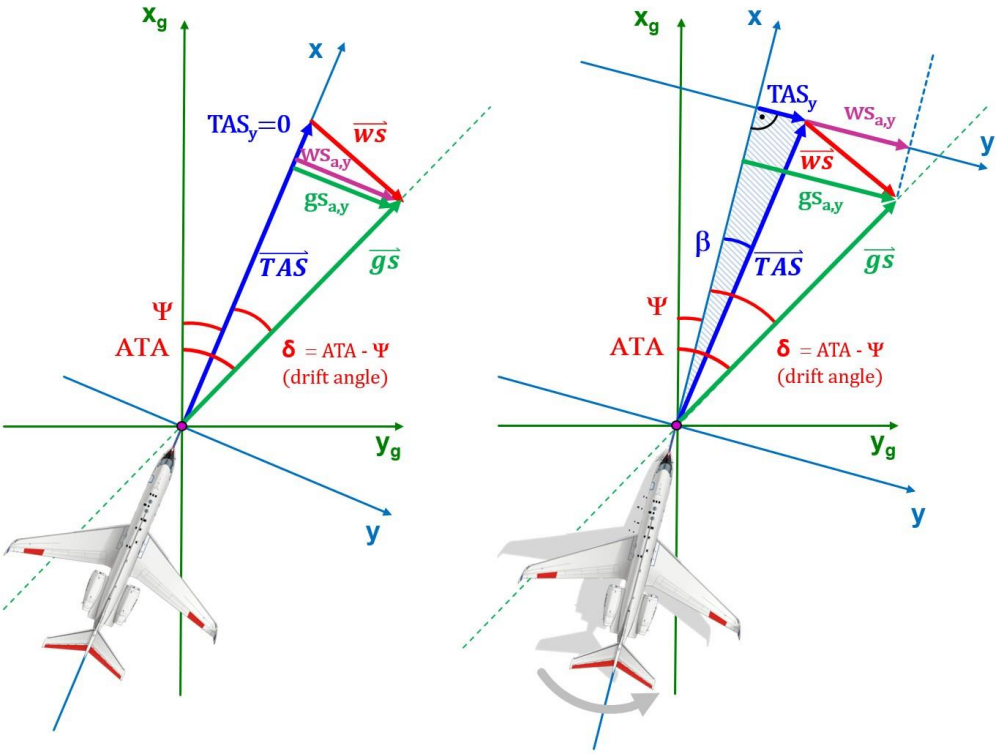

Figure 34*: Static angle of sideslip calibration using steady sideslip maneuvers. The left plot shows the aircraft in trimmed and straight flight while the right plot shows the conditions during a steady sideslip maneuver. The sideslip generates an artificial y-component of the wind in the aircraft fixed coordinate system which can be used to calculate a reference angle of sideslip.*

For the β_{ref} determination the wind equation is required in the aircraft fixed coordinate system (in which TAS is defined). In this case the wind equation must be written as:

$$\overrightarrow{ws_a} = \overrightarrow{gs_a} - \overrightarrow{TAS} \qquad \textbf{Equation 10}$$

Please note that according to Equation 6, the rotational speed component $\vec{v}_{rot,g}$ is part of $\overrightarrow{gs}$ already. Therefore, $\vec{v}_{rot}$ is included in $\overrightarrow{gs}_a$ in the above equation.

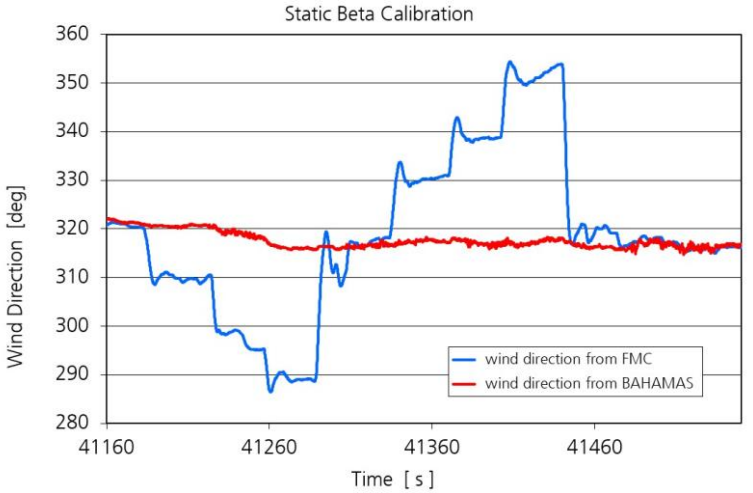

Figure 35*: Effect of steady sideslip maneuver on wind measurements. The wind data from the aircraft Flight Management Computer (FMC) is calculated by the wind triangle method while BAHAMAS uses the exact solution. Note that the corrections from the dynamic maneuver calibration are not contained in the data yet.*

While the aircraft ground speed is determined directly by the IRS during the maneuver the wind data must be determined from the atmospheric measurements before and after the maneuver. This wind data estimation should include smoothing and interpolation and requires stabilized reference test points before and after the actual β maneuvers. An evaluation of the wind variability before and after the maneuver helps to also estimate the uncertainty of the data during the maneuver. In any case, the natural variability of $\overrightarrow{ws}$ will cause statistical noise in β_{ref} which can only be handled by performing multiple sideslip maneuvers in order to get some statistics for the β calibration results.
The data handling of this calibration method contains the following steps:

The measured ground speed and the mean wind speed are transferred into the aircraft fixed coordinate system along the flight path by using the inverse matrix C^{-1} of C from Equation 1:

$$\overrightarrow{ws_a} = \begin{bmatrix} ws_{a,x} \\ ws_{a,y} \\ ws_{a,z} \end{bmatrix} = C^{-1} \cdot \overrightarrow{ws} \qquad \textbf{Equation 11}$$

and

$$\overrightarrow{gs_a} = \begin{bmatrix} gs_{a,x} \\ gs_{a,y} \\ gs_{a,z} \end{bmatrix} = C^{-1} \cdot \overrightarrow{gs} = C^{-1} \cdot \begin{bmatrix} nsv \\ ewv \\ -vv \end{bmatrix} \qquad \textbf{Equation 12}$$

with

nsv	north-south aircraft ground velocity from IRS
ewv	east-west aircraft ground velocity from IRS
vv	aircraft vertical velocity from IRS (positive: upwards!)

The y-component of Equation 10 thus yields:

$$ws_{a,y} = gs_{a,y} - TAS_y \qquad \textbf{Equation 13}$$

And from Equation 9 the value of β_{ref} can be calculated as:

$$\beta_{ref} = arcsin\left(\frac{gs_{a,y} - ws_{a,y}}{TAS}\right) \qquad \textbf{Equation 14}$$

Flight test

Due to the limited flight test time each flight had to be precisely planned in order to achieve an optimum and efficient schedule. As an example for this preparation Table 5 shows the original flight test plan and the required flight time for the static β calibration flight (test flight #3, 09.12.2016, compare to Table 7).

Test Flight #3 (09.12.2016)

Item	Estimated Time [min]
Startup	10
Climb, access to test area, approaching start coordinates (FL150, 250 KIAS)	10
1 leg yaw step maneuvers	5
Level change, approaching start coordinates (FL300, $V_1=V_{ref}$+20kts, $V_2=0.8M_C$)	15
1 leg yaw step maneuvers, V_1	5
180° turn	3
1 leg yaw step maneuvers, V_1	5
180° turn	3
1 leg yaw step maneuvers, V_2	5
180° turn	3
1 leg yaw step maneuvers, V_2	5
180° turn	3
1 yaw + 1 pitch oscillation maneuver 1 leg: 3xREF (20s), 2xTest Point (TP) (120s)	6
level change, approaching start coordinates (FL400, $V=V_2=0.8M_C$)	15
1 leg yaw step maneuvers, V_2	5
descent + landing	15
estimated total flight time:	**113**
Required flight time for the real flight	**111**

Table 5: ***Original flight test schedule and actual flight time for test flight #3 (09.12.2016, yaw step maneuvers).***

Figure 36 shows one of the steady sideslip maneuvers from the HALO flight trials. Three beta steps (2°, 3°, 4°) were performed in each direction. A single test point with a stable β_i was about 10s long while the whole maneuver took about 5 minutes. The wind vector used in Equation 11 was derived by smoothing the BAHAMAS wind data with a 5min time interval over the complete time series.

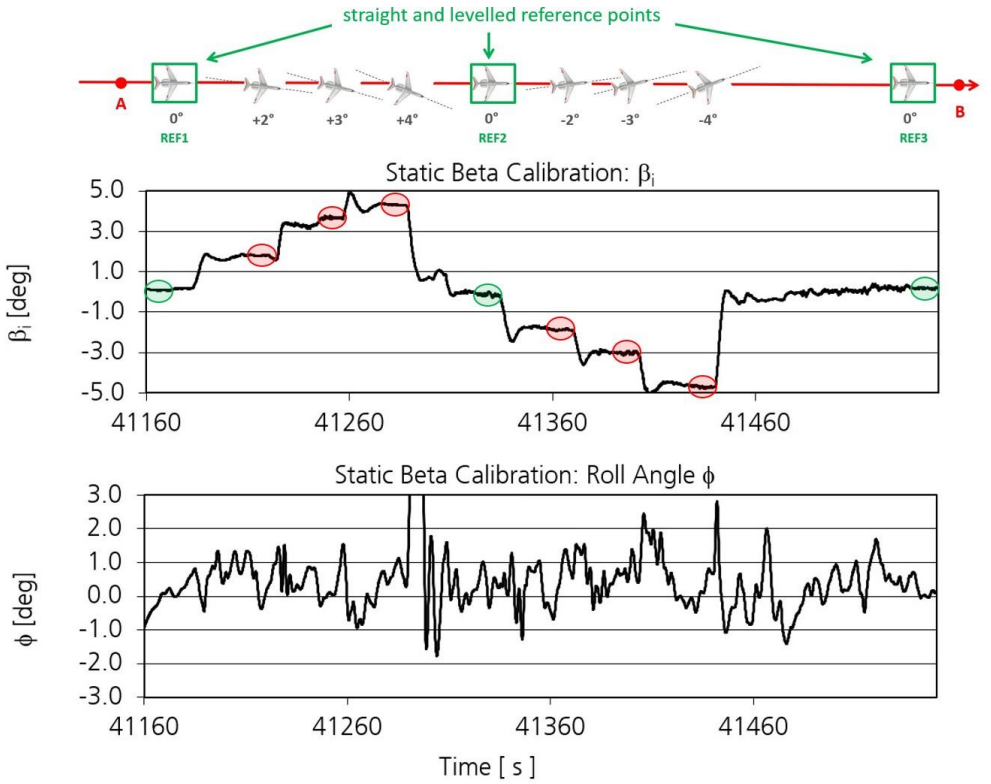

Figure 36*: Static angle of sideslip calibration. The uncorrected β_i data during the step maneuver is shown together with the planned test points above. The data used for the actual calibration is marked by red (data point) and green (reference point) circles. A single test point is about 10s long. The little variations in the roll angle prove the quality of the test points. The plot shows the same data set as Figure 35.*

The flight test was planned to cover a significant part of the aircraft envelope as required by Table 4. As can be seen from Table 6 the test points covered different flight altitudes and speeds as well as identical conditions in order to check the reproducibility of the data. The 1% qc_i specification refers to the maximum static pressure error caused by a large flow angle (between -8° to +8°).

Static Beta Calibration by Yaw Step Maneuvers				
Test Point	Aircraft altitude	Mach Number	True Air Speed	1% qc_i
Maneuver #1	FL 150	0.50	162 m/s	0.9 hPa
Maneuver #2+#3	FL 300	0.56	172 m/s	0.7 hPa
Maneuver #4+#5	FL 300	0.80	242 m/s	1.4 hPa
Maneuver #6	FL 400	0.80	231 m/s	0.9 hPa

Table 6: ***Test points of the static beta calibration.***

Result of β calibration

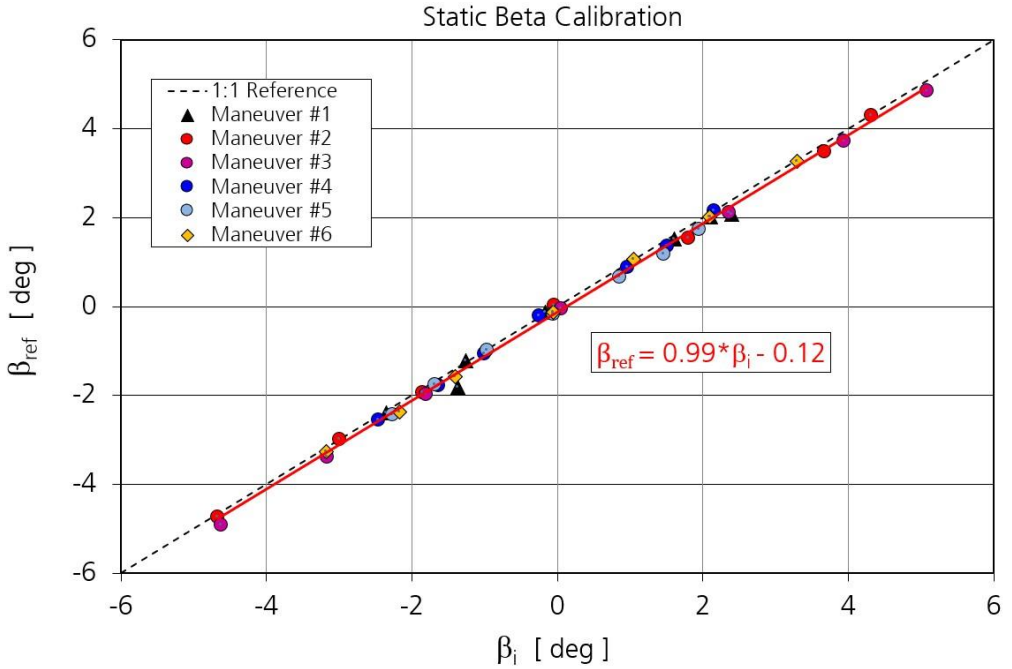

Figure 37*: Result of static angle of sideslip calibration on HALO by steady sideslip maneuvers. The data from the 6 maneuvers listed in Table 6 are shown. As one can see β_i which is measured directly by the five-hole probe is almost identical to the "real β" as described by the reference value β_{ref}.*

Figure 37 shows the result of the calibration for the 6 maneuvers listed in Table 6 which were flown under 3 different flight conditions. From the data we conclude that:

- The indicated β_i is almost identical to the reference value β_{ref}. This result is surprising especially when compared to the static α calibration where offset and slope prove that the data differs significantly from the indicated values.
- The calibration shows no dependence on flight parameters like speed and altitude, which can be seen from Figure 38

- Test points with identical flight conditions agree excellent with each other. This proves that the method works well, the sensor accuracy is very good and that atmospheric effects like wind variability did not have a significant impact on the data.
- The 2σ value of 0.22° for the mean deviation of the experimental data from the fit proves the excellent data quality of the sensors

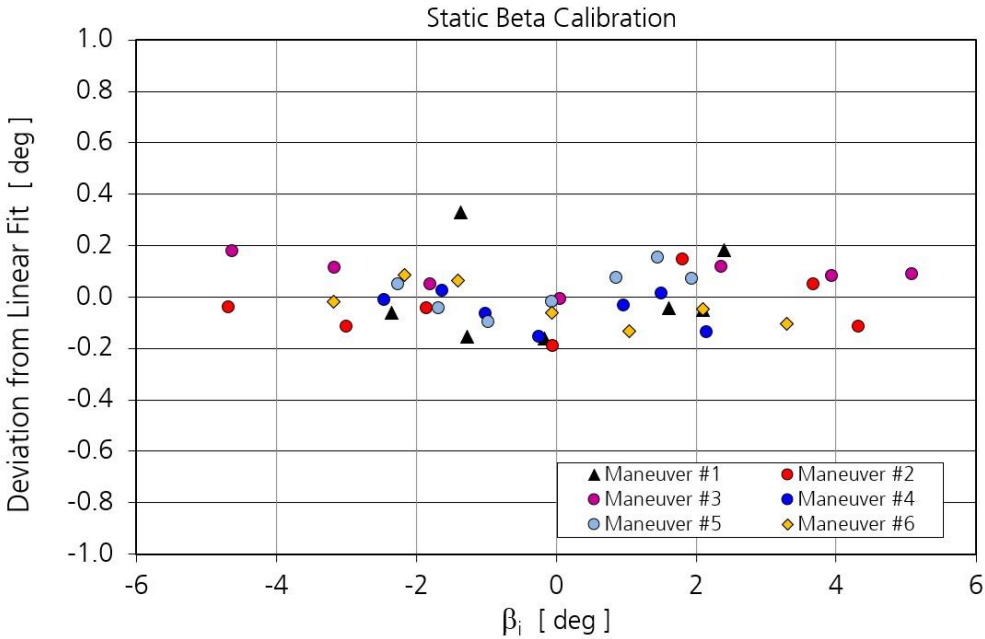

Figure 38*: Static angle of sideslip calibration: Difference of the experimental data from the fit shown in Figure 37. The 2σ deviation is 0.22° and no systematic deviation for any of the 6 test points can be detected.*

Pressure dependency on β_i from static beta calibration

The dependency of the static pressure measurement on β_i can not be detected directly in the indicated pressure measurement as one can see from Figure 39. The visible variations of ps are caused by small changes in aircraft altitude while the

effect of the sideslip angle is very small and "hidden" in the data. The dominant pressure modulations correspond to the change of atmospheric pressure with height (barometric height formula) which must be removed from the original data before a potential β_i dependency can become visible. With a known air density ρ calculated from the aircraft meteorological data (pressure, temperature) and the local gravitational constant g this pressure change dp can be calculated along the flight path as

$$dp = \rho \cdot g \cdot dz \qquad \textbf{Equation 15}$$

The time series of dp is used to correct the aircraft static pressure i.e. to reference all pressure data to a single height. This method is explained in detail in [5].
The correction is applied to the pressure data from the steady sideslip maneuvers.

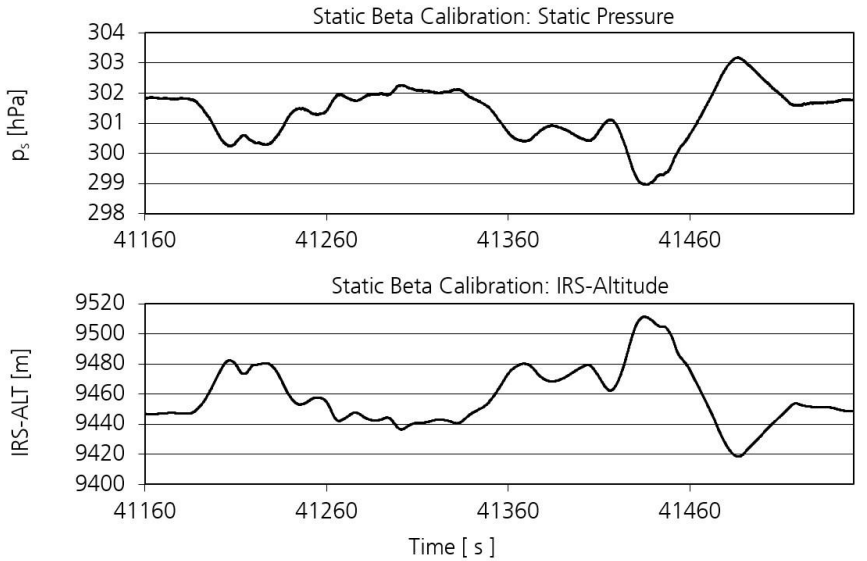

Figure 39*: HALO static pressure and aircraft altitude data from IRS during the steady sideslip maneuver shown in Figure 36. The pressure data has been corrected for static source error already. As one can see the major pressure variations can be attributed to changes in aircraft altitude.*

Additionally, the linear trend between the pressure reference measurements before and after the sideslip maneuvers (outer green circles in Figure 36) was removed to account for a possible change of the isobar height along the flight path.

The corrected static pressure data was then plotted over β_i. The result can be seen in Figure 40. It was parameterized by means of a polynomial fit. The deviations between the experimental data and the fit can be seen in Figure 41.

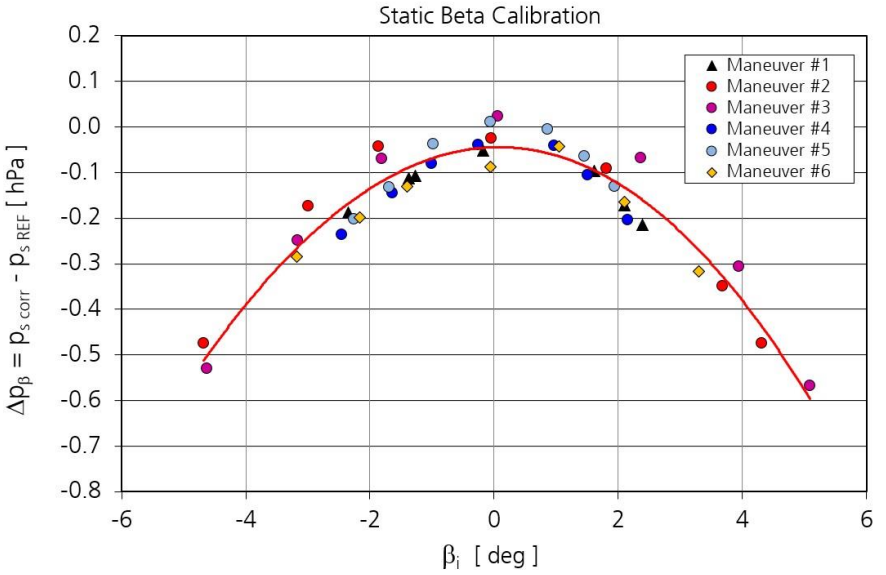

Figure 40*: Dependence of aircraft static pressure measurement on the indicated angle of sideslip β_i. The pressure data which has been corrected for static source error and aircraft altitude variations is compared to a reference value which is calculated from the pressure measurements during steady straight flight before/after the maneuver assuming a possible linear trend in the atmospheric pressure data along the flight path.*

From the results we conclude:

- The influence of a constant sideslip maneuver on the aircraft pressure measurement is relatively small (<1hPa)

- The pressure effect is independent of aircraft speed and altitude
- Test points with identical flight conditions agree excellent with each other which proves that the calibration is reproducible and the accuracy of the sensors is very good.
- The small 2σ value of 0.08 hPa shows the excellent data quality of the pressure measurement on HALO.
- It is not clear whether the observed static pressure error is caused by flow line deflection around the aircraft fuselage or by the five-hole probe itself. According to Table 6 the maximum pressure error for an indicated flow angle β_i of 8° is in the right order of magnitude to explain the effect.

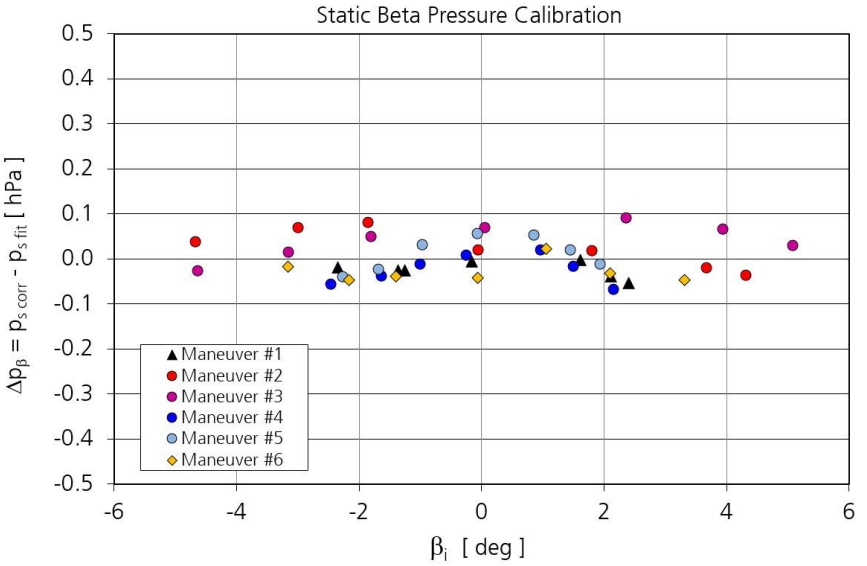

Figure 41*: Deviation of experimental data from the polynomial fit into the complete data set as shown in Figure 40. The 2σ value of the deviations is 0.08 hPa.*

In the regular HALO air data processing the input parameters to this pressure correction are low pass filtered in order to suppress undesired high frequency contributions.

Dynamic calibration of HALO airflow sensor

Dynamic Offset Calibration for α and β

The dynamic offset method determines the angular offsets of the five-hole probe axis with respect to the IRS (i.e. to the aircraft if the IRS is properly aligned). The procedure does not represent a true dynamic calibration where specific maneuvers are applied in order to determine the respective offset data. However, the method is an inflight calibration which requires that the aircraft is flying turns as part of its flight pattern.

Bögel and Baumann [1] introduced two offset angles:

- ε_b which is the angle of attack for $\alpha_i = 0$ ($dp_\alpha = 0$)
- η_b the angle of sideslip for $\beta_i = 0$ ($dp_\beta = 0$).

It is clear that an exact knowledge about the offset angles ε_b and η_b is essential for the determination of good wind data. Any misalignment between flow sensor and IRS will immediately result in wind errors since common velocity contributions in $\overrightarrow{TAS}$ and $\overrightarrow{gs}$ caused by aircraft motion will not properly cancel out in Equation 2 anymore. This results in artificial wind data.

The dynamic offset method is based on two assumptions:

I. The mean vertical wind speed during a flight is zero: $\langle w \rangle = 0$. Any artificial offset ε_b in the angle of attack data will result in a permanent vertical $\overrightarrow{TAS}$ component of $TAS_z = TAS \cdot \sin(\varepsilon_b)$ during levelled flight. This leads to an offset in the (mean) wind data. Therefore, the requirement $\langle w \rangle = 0$ leads to the determination of ε_B, the offset in α_i.

II. There shall be no correlation between vertical wind w and roll angle ϕ during turns. It is clear that the wind vector must be independent of aircraft motion. However, a misaligned nose boom or flow angle sensor

will result in airflow "crosstalk" between aircraft main axes which generates exactly such correlations. The postulated independence of *w* and ϕ means mathematically that the covariance of *w* and $\sin(\phi)$ is zero: $Cov(w, \sin(\phi)) = 0$. This condition delivers η_b.

These two requirements can be "translated" into mathematical formulations which are used to calculate the two offset angles $\varepsilon_b$and η_b. The most important formulas are listed in the following. In order to achieve maximum accuracy, the determination of ε_b and η_b is performed iteratively in running the calculation with the updated values of ε_b and η_b multiple times (preceding iteration ="old"):

$$\eta_b = \eta_{b,old} + d\eta_b$$

$$\varepsilon_b = \varepsilon_{b,old} + d\varepsilon_b$$

Equation 16

The correction to the preceding angular offsets is calculated from

$$d\eta_b = -\frac{Cov(w_{old}, \sin(\phi))}{Cov(\partial w/\partial \eta_b\,, \sin(\phi))}$$

for small roll angles (no turns)

$$d\varepsilon_b = -\frac{\langle w_{old}\rangle}{\langle \partial w/\partial \epsilon_b\rangle}$$

during turns ($\phi > 10°$)

Equation 17

where $Cov(w_{old}, \sin(\phi))$ is the covariance between w_{old} and $\sin(\phi)$. $\langle w_{old}\rangle$ is the mean value of w_{old}. As stated in Equation 17 these values have to be determined from flight segments with different roll angles. The partial derivatives are given by:

$$\partial w/\partial \eta_b = TAS \cdot [cos(\alpha)\sin(\beta)\sin(\theta) + \cos(\beta)\sin(\phi)\cos(\theta) - \sin(\alpha)\sin(\beta)\cos(\phi)\cos(\theta)]$$

Equation 18

$$\partial w/\partial \varepsilon_b = TAS \cdot [sin(\alpha)\cos(\beta)\sin(\theta) + \cos(\alpha)\cos(\beta)\cos(\phi)\cos(\theta)]$$

The method and the derivation of the above equations are described in detail in [11].

Figure 32 shows the result of the dynamic offset method in comparison with the static inflight α calibration. As one can see the results of these two methods agree very well. However, this is not always the case. Both methods depend on the available flight data:

- The static α inflight calibration requires a significant data range in α_i in order to calculate a robust fit
- The dynamic offset method requires a certain amount of turns in the flight pattern to calculate a representative η_b.

On HALO $\varepsilon_b$and η_b are determined for each flight and it is an individual decision which method is chosen for the determination of η_b. In very few cases with insufficient data for a proper determination of theses offset angles the values of $\varepsilon_b$and η_b are copied from the preceding flight.

Dynamic Calibration: Strategy and Flight Test Plan

A total of only 3 flights with a duration of 2 hours each were available for these flight trials. Therefore, the experiment required a proper and efficient test plan which had to address the following issues:

- Define optimum maneuvers
- Cover relevant part of the flight envelope
- Check for reproducibility of the results
- Determine the dominant dependencies from aircraft data
- Establish an appropriate data handling for the airflow sensor data in order to correct the maneuver impact on the data

The three flights also had to cover the static beta calibration described above.

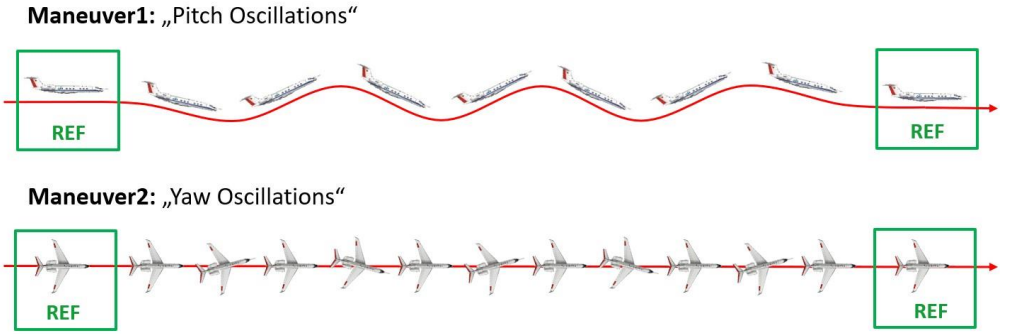

Figure 42*: Inflight maneuvers for the dynamic calibration. Harmonic oscillations in pitch and yaw are applied to the aircraft while the actual flight track angle remains constant. The mean aircraft altitude and aircraft speed should be kept constant. A reference measurement (REF) with straight and levelled flight is performed before and after each test point.*

As explained above two maneuvers were flown for the dynamic calibration of the flow sensor. Figure 42 shows the dynamic pitch and yaw maneuvers. Each of them makes up a single test point. The maneuver starts with a reference measurement where the aircraft is in stabilized straight flight with the chosen flight parameters (speed and pressure height) for the respective test point. The reference

measurements require about 20s of stabilized flight and deliver accurate mean data for pressure, temperature and wind at the start and the end of the oscillations. This helps to identify atmospheric trends along the flight track and to provide accurate reference data for thermodynamic calculations.

In order to systematically study the interaction between the maneuver data and the wind the flight tracks were oriented along and across the mean horizontal wind direction as indicated by the aircraft avionic system. The duration of a single oscillation maneuver was about 2 minutes.

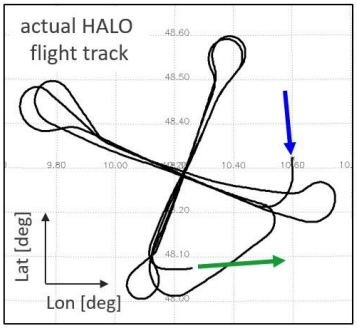

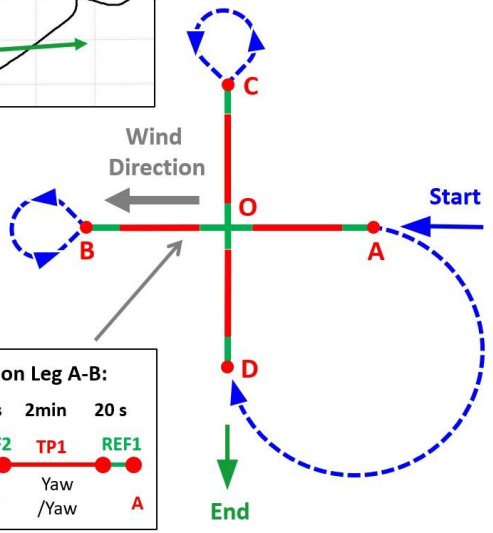

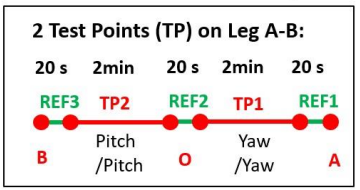

Track	wind direction	Section	TP #	Maneuver
Entering level, determining wind direction				
A-B	back	REF1		reference
		TP1	1	pitch oszillation
		REF2		reference
		TP2	2	yaw oszillation
		REF3		reference
180° Turn				
B-A	front	REF3		reference
		TP2	3	yaw oszillation
		REF2		reference
		TP1	4	pitch oszillation
		REF1		reference
180° Turn				
A-B	back	REF1		reference
		TP1	5	pitch oszillation
		REF2		reference
		TP2	6	yaw oszillation
		REF3		reference
180° Turn				
B-A	front	REF3		reference
		TP2	7	yaw oszillation
		REF2		reference
		TP1	8	pitch oszillation
		REF1		reference
270° Turn to D				
D-C	right	REF1		reference
		TP1	9	pitch oszillation
		REF2		reference
		TP2	10	yaw oszillation
		REF3		reference
180° Turn				
C-D	left	REF3		reference
		TP2	11	yaw oszillation
		REF2		reference
		TP1	12	pitch oszillation
		REF1		reference
180° Turn				
D-C	right	REF1		reference
		TP1	13	pitch oszillation
		REF2		reference
		TP2	14	yaw oszillation
		REF3		reference
180° Turn				
C-D	left	REF3		reference
		TP2	15	yaw oszillation
		REF2		reference
		TP1	16	pitch oszillation
		REF1		reference

Figure 43*: Planned flight pattern for the dynamic inflight calibration. The actual HALO flight track from 17.03.2016 (flight #1) shows a case where each leg of the cross was flown 4 times according to the test plan on the right side.*

The final flight test plan is shown in Figure 43. The basic flight pattern is a cross which is aligned with the wind direction. A single leg of the cross contains two test points (yaw and pitch) with identical flight parameters and a common reference measurement in the middle of the cross. The pitch and yaw oscillations are arranged in a way that a single test point is flown two times immediately after each other with the same maneuver but opposite heading.

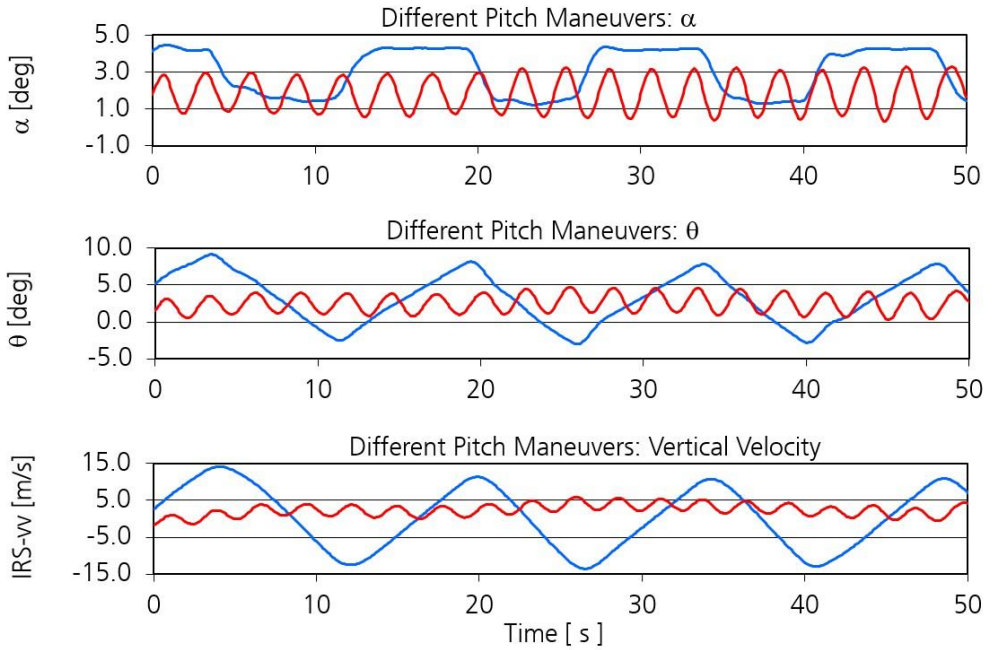

Figure 44: ***Different amplitudes and frequencies were tested for the dynamic inflight calibration. The plot shows two extreme examples (red/blue) of pitch oscillation maneuvers from different calibration flights.***

An important question concerns the choice of an appropriate frequency and amplitude for the pitch and yaw oscillations. In order to find the optimum parameters, the HALO flight tests covered a wide spectrum of these parameters. Figure 44 shows two extreme examples for a pitch oscillation maneuver with respect to amplitudes and frequency. However, it must be clear that a correction

of airflow data for these dynamic effects should be independent of maneuver frequency or amplitude.
It is clear that a detailed data analysis after the first flight is necessary in order to understand the main dependencies in the data, to establish a suitable correction scheme and to define an efficient flight test plan for the following flights which focusses on the "right" flight parameters. Therefore, the first test flight aimed at the provision of a suitable data set for this analysis.
Table 7 lists the test flights for this experiment as well as the strategy and planned test points for the single flights. The table shows that the second test flight took place more than 6 months after the first one for the reasons mentioned above. The last flight was also performed much later in order to cover a different aircraft configuration.

The test plan in Table 7 also lists a flight pattern "full circle" which was performed with different roll angles and turning direction. It turned out that this maneuver was not suitable for the inflight calibration of the flow angle sensor and the data from this maneuver is not presented in this report.

In order to detect possible trends in the calibration, to check for the reproducibility of the results and to improve the flight envelope coverage of the calibration data it was established that yaw and pitch maneuvers became a mandatory part of every HALO measurement campaign which uses high frequency wind data. The data gained from these campaigns is included in this report in order to complete the data set and to prove the reliability of the results determined from this initial flight test campaign.

Flight	Pattern	Flight Conditions	Goal
FLT#1: 17.03.2016 (BP+VF)	pitch + yaw oscillations, along/across wind direction (16 test points)	FL230, 220kts CAS	• demonstration of method • definition of appropriate maneuvers • reproducibility of a single TP • accuracy check • atmospheric influence
	full circles ϕ=20° (1x) ϕ=40° (2x)		• definition of appropriate maneuvers
Data analysis: Evaluate the results. Establish an appropriate calibration. Analyze dependency on flight parameters. Define test strategy for following flights.			
FLT#2-a 27.10.2016 (BP+VF)	pitch + yaw oscillations, along/across wind direction	FL430, 225kts CAS FL150, 225 kts CAS	• dependence on flight parameters (a/c envelope)
	FLT #2 had to be aborted due to a health incident. The programme was completed on a short second flight (FLT#2-b)		
FLT#2-b 28.10.2016	pitch + yaw oscillations, along/across wind direction	FL150, 225 kts CAS	• completion of test points from preceding flight • flight to flight reproducibility (i.e. to FLT#2-a)
	full circles ϕ=30° left+right turn		• dependence on flight parameters
FLT#3 09.12.2016 (clean)	yaw step maneuvers	FL150, 250kts CAS FL300, 210kts CAS FL300, M_C=0.8 FL400, M_C=0.8	• static β calibration • dependence on flight parameters (a/c envelope)
	pitch + yaw oscillations, along/across wind direction	FL300, M_C=0.7 different frequencies pitch: 3 frequencies yaw: high frequency	• dependence on flight parameters (a/c envelope) • dependence on aircraft configuration • maneuver frequency dependence

Table 7: ***Plan for the flight test of the dynamic maneuver calibration. A total of three flights with 2h flight time each were planned for this experiment. The steady sideslip maneuvers which are described in the static calibration chapter above were also part of this flight test. BP+VF refers to the aircraft configuration with Belly Pod and Ventral Fin.***

Dynamic Calibration Basic Considerations

The inflight calibration uses wind data which is measured by BAHAMAS and processed by the Instrumentation and Data Science Group of the DLR Flight Experiments Facility. The aircraft data was processed by the "Research Aircraft Meteorological Data Evaluation Software" (RAMSES). RAMSES was developed by this group and represents a modular software package which is used for all meteorological research aircraft operated by DLR.

The aircraft airflow, pressure and wind data shown in the following has been processed by RAMSES with

- a time resolution of 10Hz
- the static source error correction of the pressure data as determined in the trailing cone experiment
- a dynamic offset calibration for α and β
- the static beta calibration as shown above
- post processed data from the experimental IRS for aircraft position, speed and attitude. Reference location is the IGI IMU in the aircraft nose
- a regular timing check between IRS and flow sensor data which confirms a max. deviation of dt<0.01s for the whole flight (i.e. no time shift correction has been applied to any data)

Dynamic angle of attack calibration

The Lenschow Criterion: First Results

Figure 45 shows the data from the first calibration flight on 17.03.2016. The time series of more than 1h length shows the vertical wind speed w and the aircraft vertical speed vv for 8 pitch oscillation test points as described by flight plan in Figure 43.

The vertical wind variation at FL230 is relatively small (<0.5 m/s). The impact of the pitching maneuver on the wind data is visible and in the same order of magnitude.

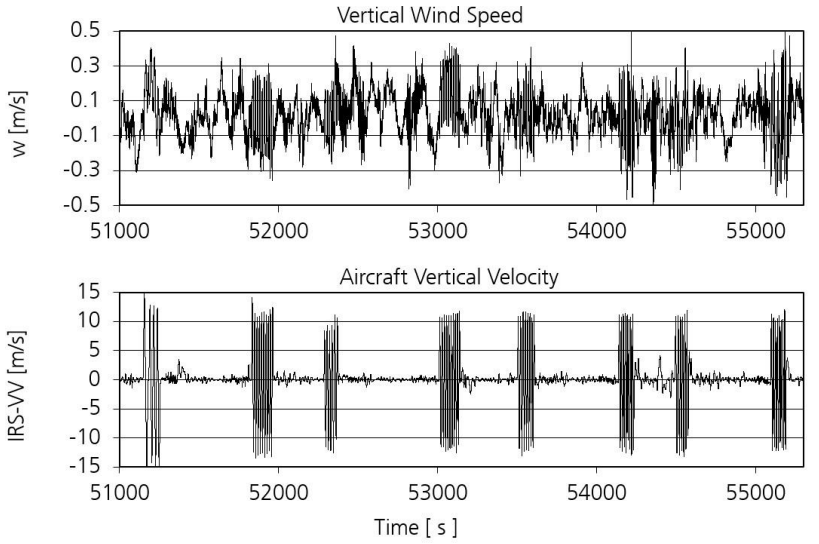

Figure 45*: Vertical aircraft velocity (IRS-VV) and wind vertical velocity (w) for the complete cross pattern of flight #1 (17.03.2016).*

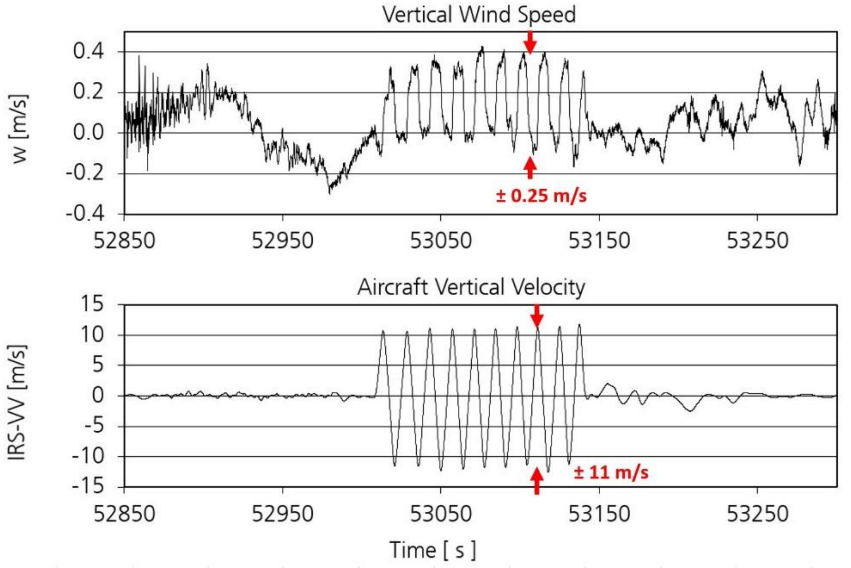

Figure 46*: Initial check of the Lenschow Criterion for a single test point from the time series shown in Figure 45.*

Figure 46 shows a single pitching maneuver from this flight. As one can see the Lenschow Criterion is well fulfilled. This means that the HALO wind measurement system together with a standard data processing can be treated as "good" for atmospheric research.
However, the clear signature of the pitching maneuver in the vertical wind data gives reason to investigate whether it is possible to further minimize this effect.

Impact of Maneuver Frequency

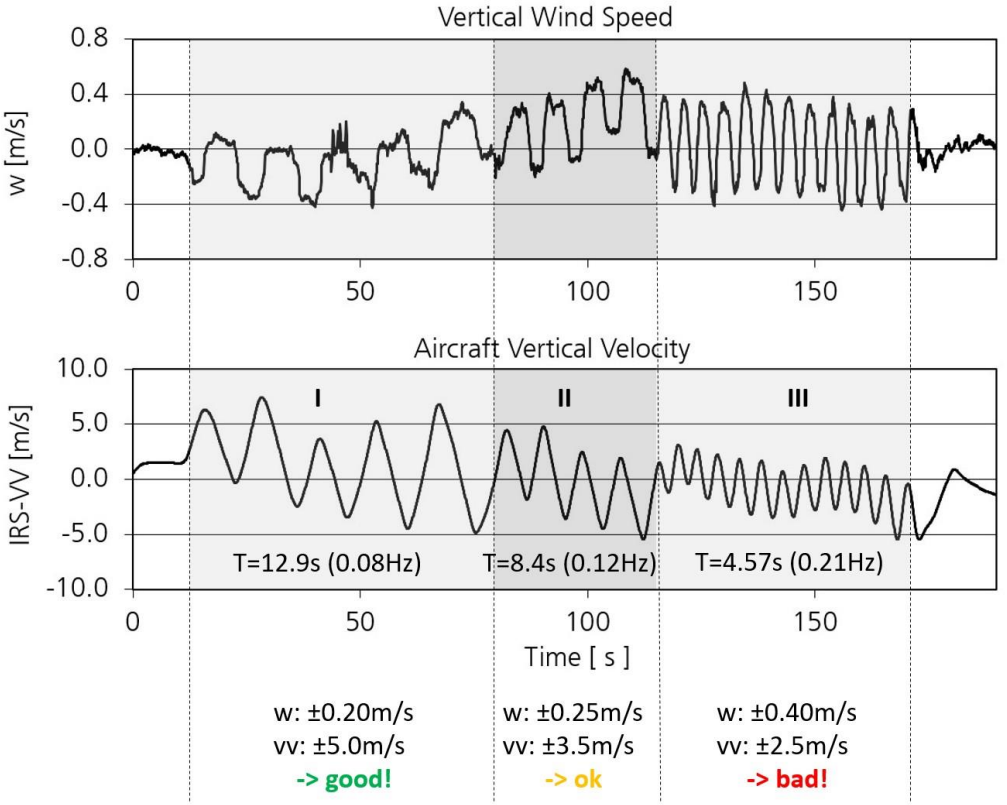

Figure 47*: Check of the Lenschow Criterion for a pitch maneuver with varying pitching frequency. While the data looks good for slow maneuvers the Lenschow Criterion is violated at high pitching frequencies.*

The pitch maneuvers shown in Figure 45 were flown with extreme amplitudes and a low pitching frequency (blue line in Figure 44). During the following flights additional testing included pitching oscillations with different frequencies. Figure 47 shows a case where the pitch rate was changed two times during a maneuver. The comparison of vertical aircraft speed and vertical wind speed gives a surprising result. Although aircraft speed and altitude are kept constant during the complete maneuver the Lenschow Criterion is fulfilled at lower pitching rates but violated at higher frequencies.

This means that **the Lenschow Criterion is frequency dependent and can therefore not be treated as a good benchmark for airborne wind measurement systems any more.**

As a consequence, we have to focus on a correction for the data which minimizes the impact of aircraft maneuvers on the wind measurement.

Improve the Vertical Wind Measurement: Strategy

As explained above the following parameters are excluded from a search for this correction:

- Time delays between the different data sources: This effect can be excluded due to the systematic timing checks between the IRS and the analog data acquisition.
- Errors in the IRS data (time response issues or measurement errors in the speed and attitude data): The data processing of this experiment uses only post processed IRS data. The error bars of the processed data are significantly smaller than the margins which could explain the artificial wind modulations
- Errors in the TAS absolute value measurement which are caused by errors in the pressure measurement of p_{si} (and qc_i). As we see later this error is also too small to explain the effect.

Therefore, we conclude that the main error source for the vertical wind modulation during the pitch maneuvers must be the **airflow angle measurement**.

In order to investigate this issue, we have to understand the impact of a modified α on the artificial vertical wind modulations during the maneuvers. In order to find an optimized α we propose to minimize the existing cross talk in the wind data by „optimizing“ α in the following way:

1) Modify α:
    - Apply a variable linear correction factor k_α to the original α
    - Apply a variable offset correction $d\alpha$ to α , i.e.

$$\alpha_{new} = k_\alpha \cdot \alpha_{orig} + d\alpha \qquad \textbf{Equation 19}$$

2) Determine the correlation between α_{new} and w as a function of k_α and $d\alpha$. This is achieved by calculating the vertical wind for each α_{new} according to Equation 19 and determining the correlation coefficient $CC(w, \alpha_{new})$ between α_{new} and w.
3) Analyze $CC(w, \alpha_{new})$ as a function of k_α and $d\alpha$. Search for a minimum of the correlation coefficient absolute value in order to get the optimum correction factors for k_α and $d\alpha$.

We will present this method for two cases from the first calibration flight which can be seen in Figure 48. “Case A” shows a test point with a homogeneous and calm atmosphere where the artificial modulation of w dominates the signal. “Case B” shows a stronger atmospheric variance with low frequency contributions along the time series. In both cases one can nicely see how the “real” atmospheric signal superimposes the dominant modulations which are caused the maneuver.

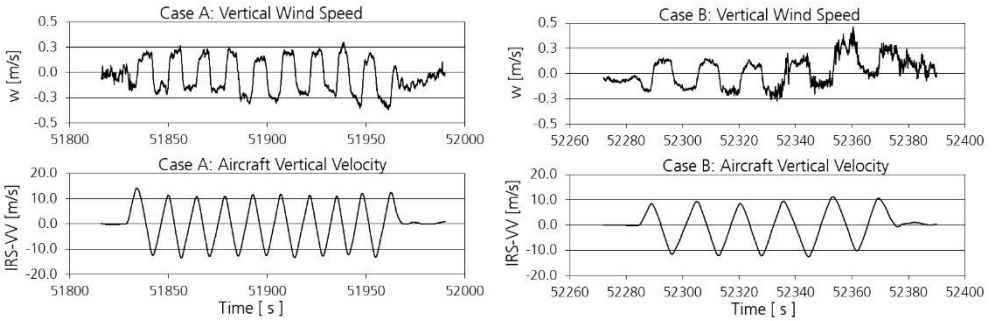

Figure 48*: Original vertical wind data for the two pitch oscillation maneuvers which are analyzed in this section.*

The plot of the absolute value of $CC(w, \alpha_{new})$ over k_α was used to determine the "best" k_α where the correlation is found to be minimal. The same procedure was applied to the offset value $d\alpha$.

As a first result we have to state that **the search for a "best" offset $d\alpha$ was not successful**, no dependence of $CC(w, \alpha_{new})$ on this parameter could be observed. Therefore, we do not further discuss $d\alpha$ in this investigation.

However, in case of k_α the result was completely different. Figure 49 shows the absolute value of the correlation coefficient between w and α as a function of k_α. One can immediately see that this correlation vanishes almost completely for $k_\alpha \approx 1.05$ in both cases (the sharp minimum is due to the fact that $CC(w, \alpha_{new})$ has a zero crossing at this point). We conclude that α is underestimated during the maneuvers at this test point. A 5% increase of the α values eliminates the artificial vertical wind modulations by the maneuver. Figure 50 shows the vertical wind speed as calculated from the corrected alpha. The influence of the maneuver on the vertical wind data is completely removed and the natural variability of w can be seen over the full frequency range.

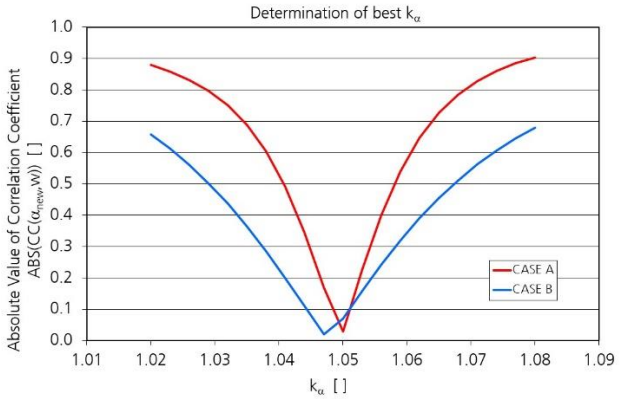

Figure 49*: Determination of an optimum correction factor k_α in Equation 19 which minimizes the absolute value of the correlation factor $CC(w,\alpha)$ between vertical windspeed and α during pitch oscillation maneuvers.*

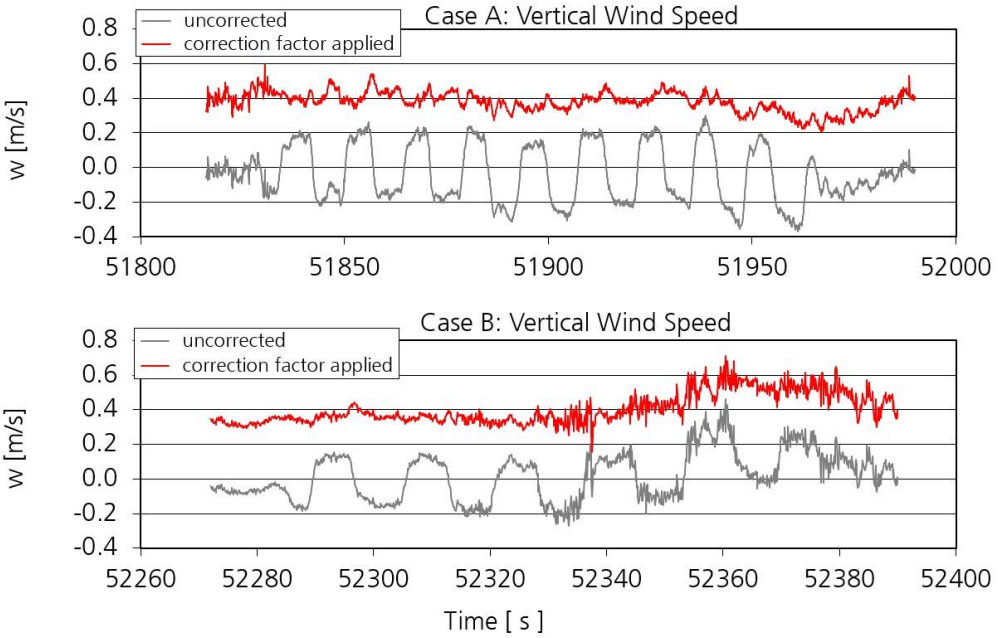

Figure 50: The application of a "best" k_α eliminates the artificial w variation from the maneuvers but causes a mean offset of w.

However, Figure 50 also demonstrates that the correction of α with a constant factor leads to another problem. The corrected vertical wind speed now shows a systematic offset i.e. the mean w is no longer zero.
It is immediately clear, that an additional scaling factor violates the existing static α calibration according to Figure 30 or Figure 32. The basic idea behind this calibration was the assumption that the mean α must be identical to the aircraft pitch θ because the mean vertical wind is zero. Therefore, the systematic 5% increase of alpha must be interpreted as a constant vertical wind.
This finding is complicated by the fact that the value for the optimum k_α is not constant. It varies with changing flight conditions as we will see later in this report. This means that the vertical wind data would show different offsets at different aircraft speed and altitude settings.

Trimmed Alpha

Since the mean w on a flight leg must remain zero and should not depend on flight conditions we propose the following solution:

1. We accept the result from the static calibration where the mean α is compared to the mean θ under the assumption that the mean vertical wind is zero.
2. We assume that only sudden changes i.e. the **dynamical** part of α is not scaled properly by the results from the **static** calibration. We propose to apply a correction only to the deviations from a "typical" α which is characteristic for the respective flight state and which is depending on aerodynamic parameters.

The determination such a "typical" α from other independent parameters which describe the aircraft aerodynamic state is the main challenge for this solution. The pitch angle is not a suitable solution any more since θ is a geometric unit. Furthermore, the pitch angle systematically deviates from α during aircraft vertical motion which is the case for the pitch oscillations maneuvers.
Bögel and Baumann [1] propose in their paper on calibration of the DLR Falcon aircraft a "trimmed angle of attack" which is used to parameterize the impact of

α variations on pressure data. Starting with the lift equation for trimmed horizontal flight they introduce a "trimmed alpha" and show that this unit is proportional to the inverse dynamic pressure qc:

$$\alpha_{trim} \sim \frac{1}{qc} \qquad \textbf{Equation 20}$$

Based on this result we propose to determine α_{trim} from a linear fit between α and $^1/_{qc}$ for those sections of a flight where the aircraft is in trimmed horizontal flight.

Determination of α_{trim}

A disadvantage of the proposed solution is given by the fact that the planned fit uses final data i.e. the values of α and qc which have already been corrected for all other aerodynamic effects. This would require to process the aircraft data two times. Therefore, we investigated the possibility to apply this procedure to the indicated values of flow angle and dynamic pressure as measured directly by the sensor, i.e.

$$\alpha_{i,trim} \sim \frac{1}{qc_i} \qquad \textbf{Equation 21}$$

As we will see below this procedure is completely equivalent with the original proposal.

Figure 51 shows this fit for different data sets from the trailing cone experiment. The examples cover the complete aircraft flight envelope and represent mean data from test points with stabilized horizontal flight conditions. Therefore, most of the α_i fluctuations caused by vertical wind are eliminated. As one can see the basic relation between α_i and $^1/_{qc_i}$ can be well represented by a linear fit on a single flight leg. However, one can also see that this fit depends on aircraft configuration

and aircraft altitude. Therefore, we conclude that the fit should be performed individually for each flight and each single flight leg (altitude).

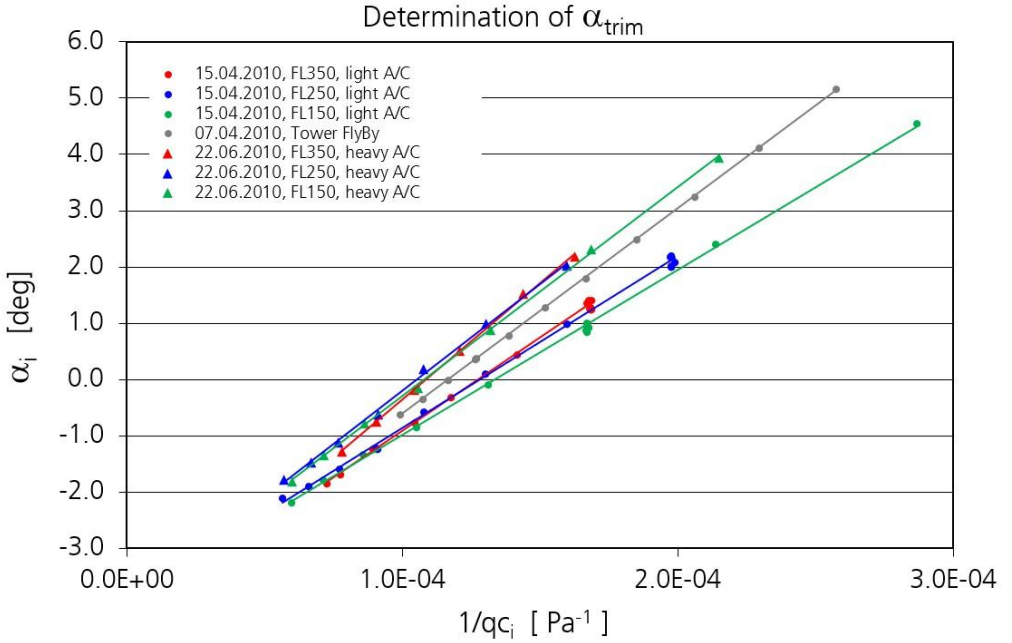

Figure 51*: Determination of $\alpha_{i,trim}$ from a fit of α_i over $^1/_{qc_i}$. The data set from the trailing cone flight trials shows the respective result for different aircraft configurations and flight levels. The test points on a single flight level represent the complete speed range of HALO at that height.*

Another problem in the determination of $\alpha_{i,trim}$ becomes obvious when regarding the aircraft data from a very long flight leg. Figure 52 shows such a case from a HALO research flight. As one can see the angle attack decreases over time which is due to the change of aircraft weight caused by the burned fuel. It is obvious that qc_i will not show a comparable time trend. Therefore, it is necessary to take this trend into account before applying the fit between α_i and $^1/_{qc_i}$.

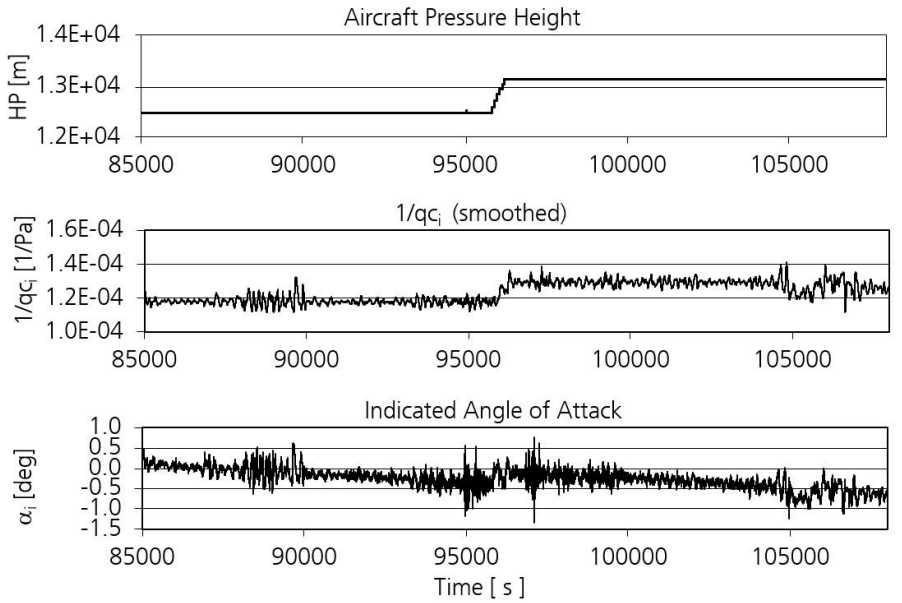

Figure 52*: Time series of α_i and $^{1}/_{qc_i}$ for a flight leg of 6.3h duration. The qc_i data was smoothed over 2s. Most of the data represents straight and levelled flight since the data contains only one flight level change and one turn (on the first height level).*

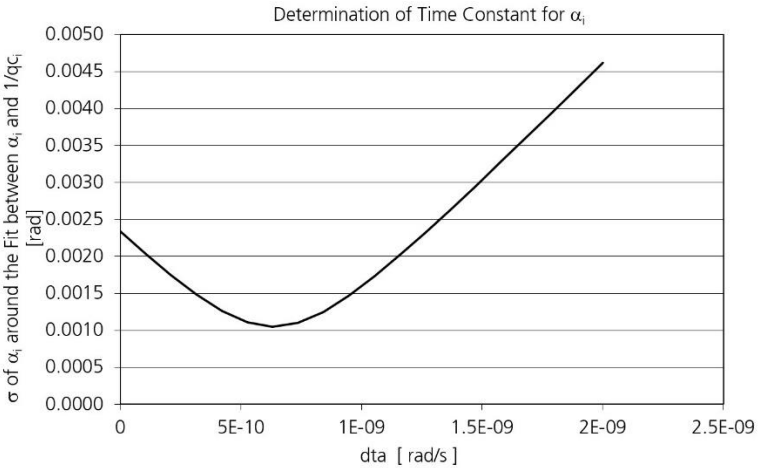

Figure 53*: Determination of the time trend constant dta by minimizing the variability of α_i with respect to $\alpha_{i,trim}$.*

This is done by assuming that the time trend in α_i can be represented by a linear trend with a fixed slope (dta).
The fit between α_i and $^1/_{qc_i}$ is then calculated for different dta. A result from each fit is the standard deviation σ of α_i with respect to this fit. The plot of σ over the time constant dta yields a minimum for the best value of dta. This can be seen in Figure 53.

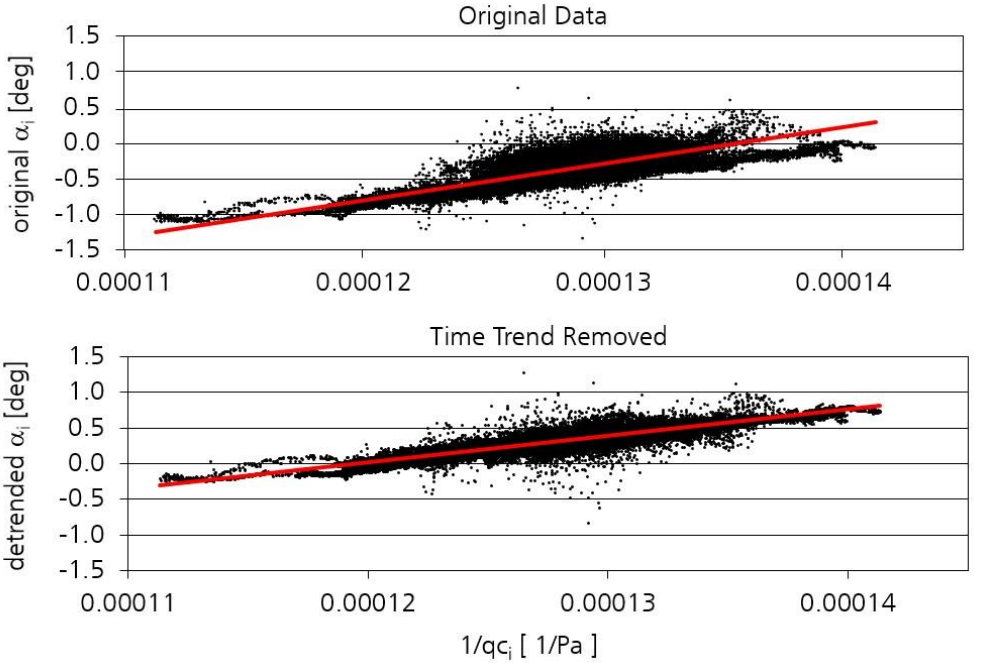

Figure 54*: Effect of time trend removal in α_i for the fit of α_i over $^1/_{qc_i}$. The plot shows the data from the right (higher) flight level in Figure 52 which represents a straight and levelled flight leg of more than 3h. The upper plot shows the fit for the uncorrected data of α_i and $^1/_{qc_i}$ while the lower one shows the same fit after the time trend of α_i was removed. The standard deviation σ of α_i around this fit is plotted in Figure 53 as a function of dta.*

Figure 54 shows how the systematic deviations of α_i from $\alpha_{i,trim}$ (i.e. the fit) are reduced with the right choice of dta. The remaining scatter represents high frequency variations of α_i caused by vertical wind modulations which will be subject to the dynamic angle of attack correction with k_α.

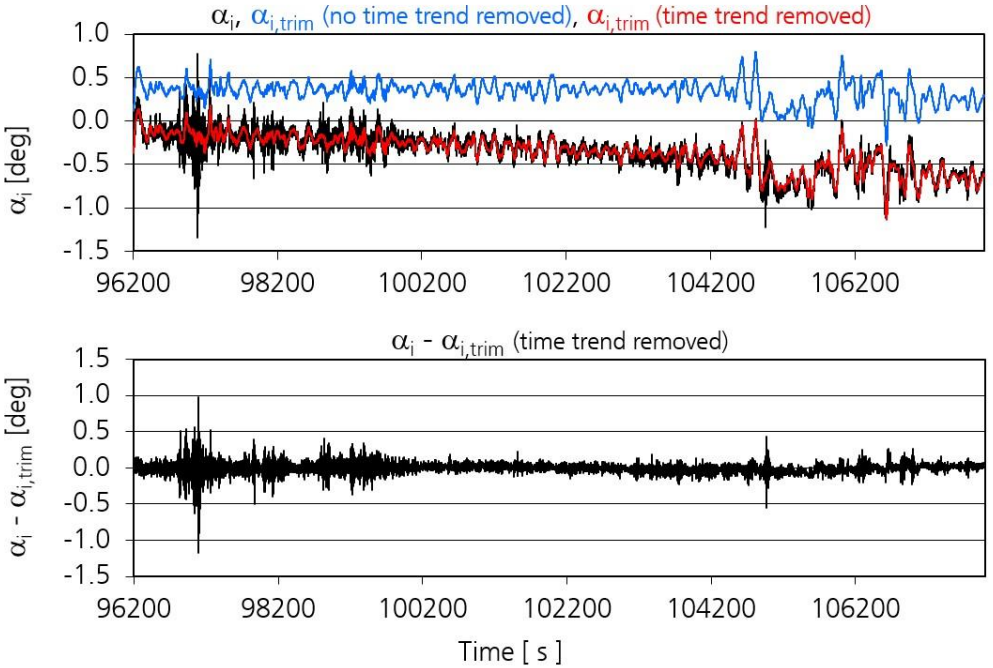

Figure 55*: Time series of α_i and $\alpha_{i,trim}$ for the same flight leg as in Figure 54. The upper plot shows the effect of time trend removal in $\alpha_{i,trim}$ (the original $\alpha_{i,trim}$ is plotted with an offset). The lower plot shows the difference between the original α_i data and the time trend corrected $\alpha_{i,trim}$. One can nicely see that the wind induced high frequency variations lie symmetrically around the $\alpha_{i,trim}$ curve.*

Figure 55 shows the respective results for the right flight leg in Figure 52. One can see that most of the low frequency fluctuations in α_i can be explained by modulations of qc_i. This means that the α correction with k_α concerns mostly the high frequency modulations as shown in the lower plot which can be associated

with vertical wind fluctuations. Figure 56 shows how α_i, $\alpha_{i,trim}$ and their difference look like during the pitch maneuvers of the 2 selected examples.

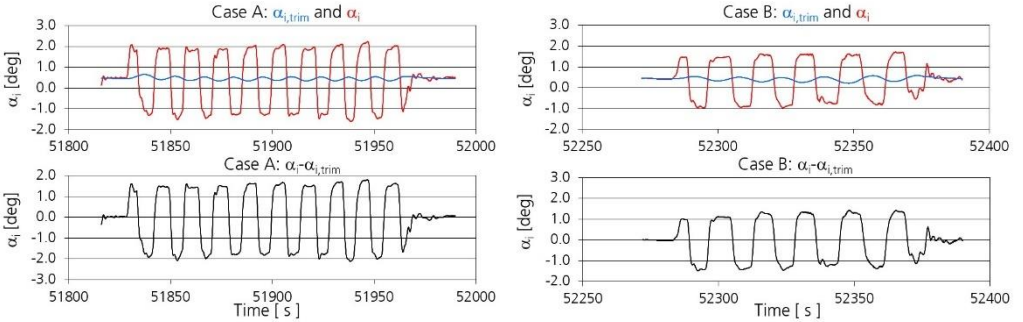

Figure 56*: Time series of α_i and $\alpha_{i,trim}$ for the two cases from the first flight. The lower plot shows the difference between these two units which is subject to the correction with k_α.*

$\alpha_{i,trim}$ for other flight conditions

We have shown that the establishment of a trimmed alpha seems to work very well during straight and levelled flight. A critical point concerns the limitation of this concept to horizontal levelled flight only.

We cannot prove the validity of the correction scheme for other flight conditions but the presentation of a comparison between α_i and $\alpha_{i,trim}$ helps to understand systematic effects during other parts of the flight. Figure 57 to Figure 60 show this comparison for the first two calibration flights and one can immediately see common effects.

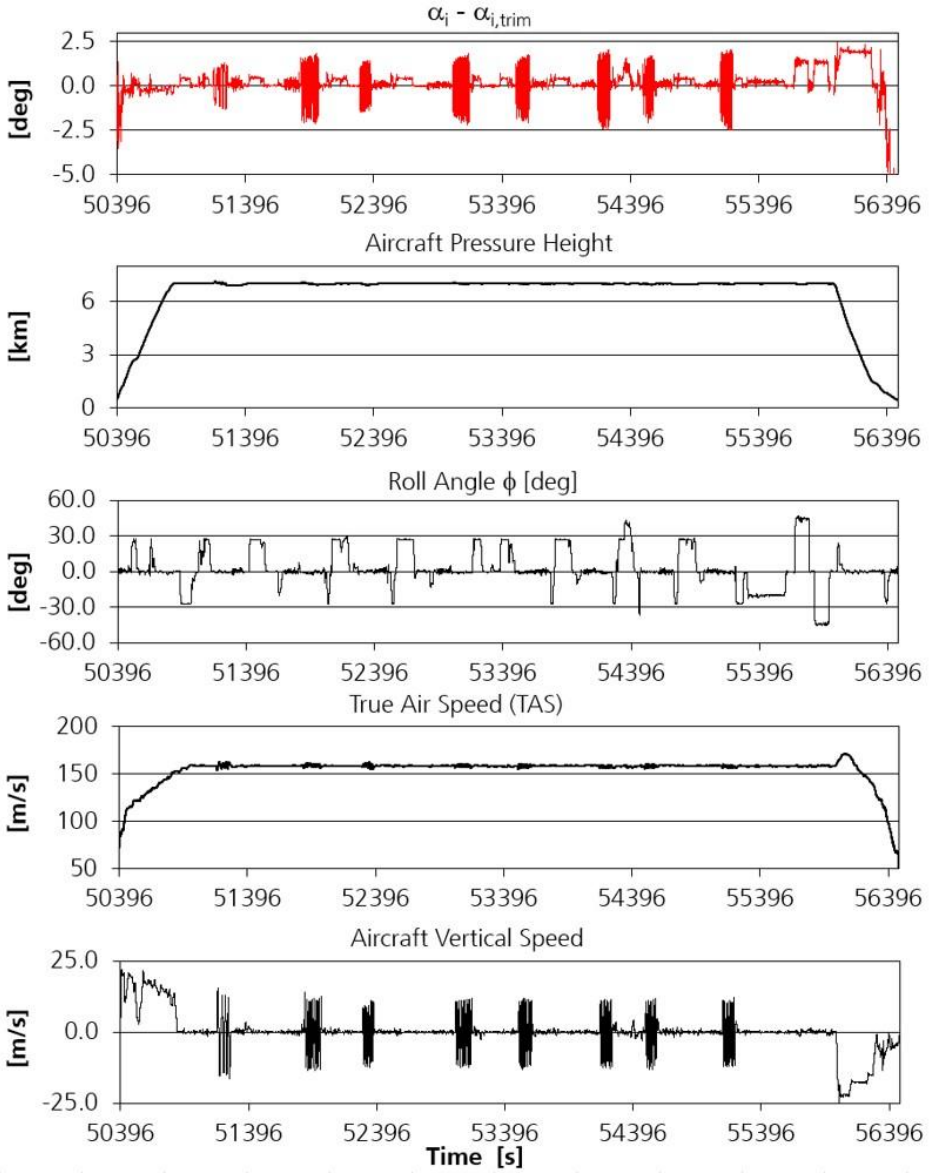

Figure 57*: Difference between α_i and $\alpha_{i,trim}$ and the most important flight parameters for the complete first calibration flight. $\alpha_{i,trim}$ was calculated with a single parameterization which was determined on the main flight level (FL230).*

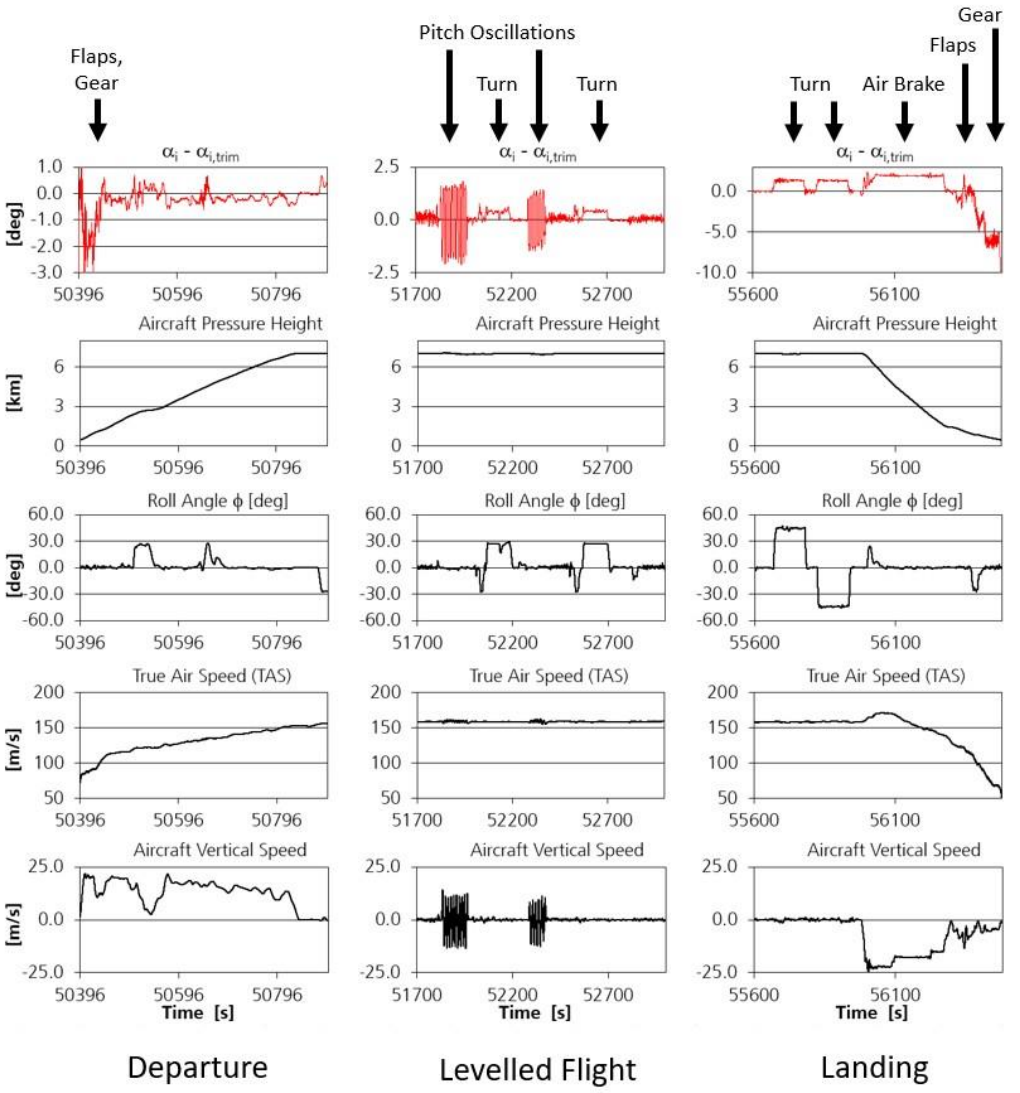

Figure 58*: Difference between α_i and $\alpha_{i,trim}$ and the most important flight parameters for three different flight states (departure, test points on flight level, landing) of the first calibration flight.*

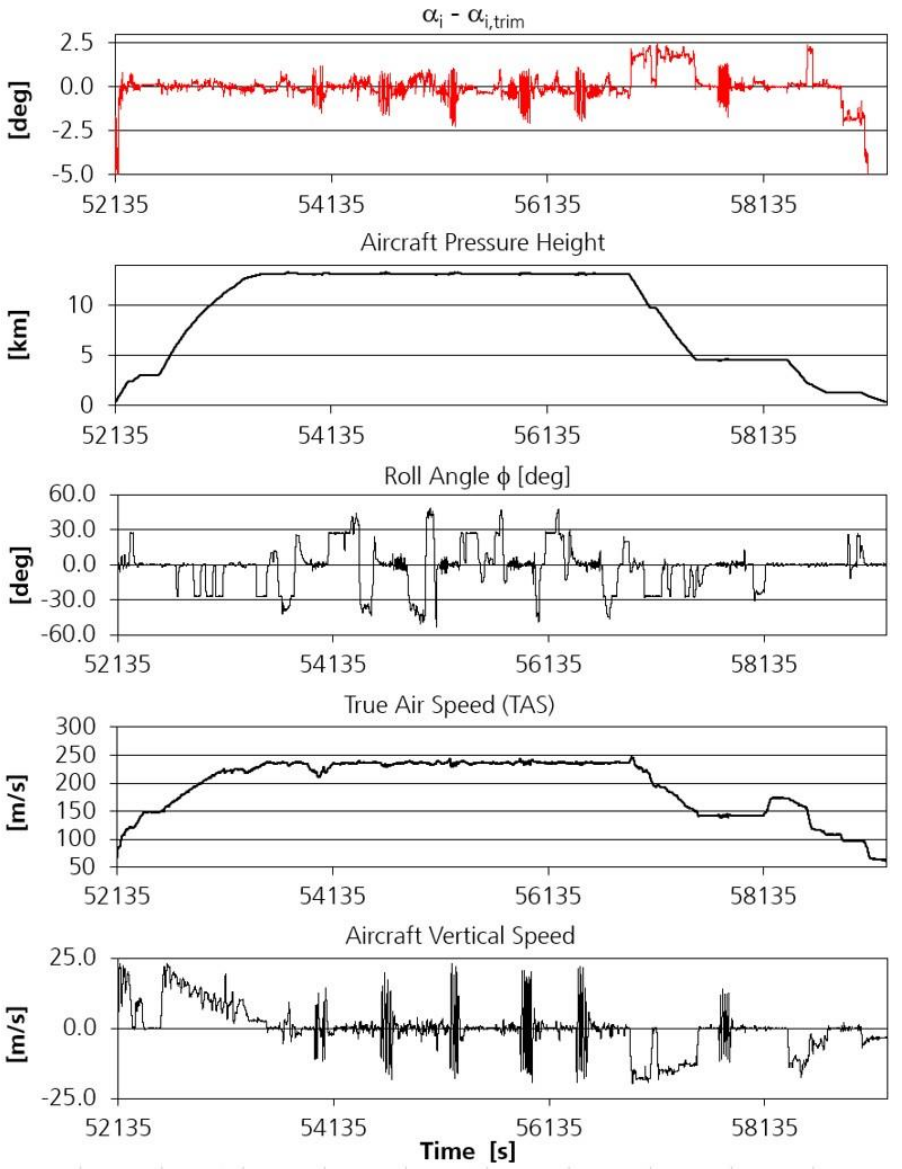

Figure 59*: Difference between α_i and $\alpha_{i,trim}$ and the most important flight parameters for the complete second calibration flight. $\alpha_{i,trim}$ was calculated with a single parameterization which was determined on the lower flight level (FL150).*

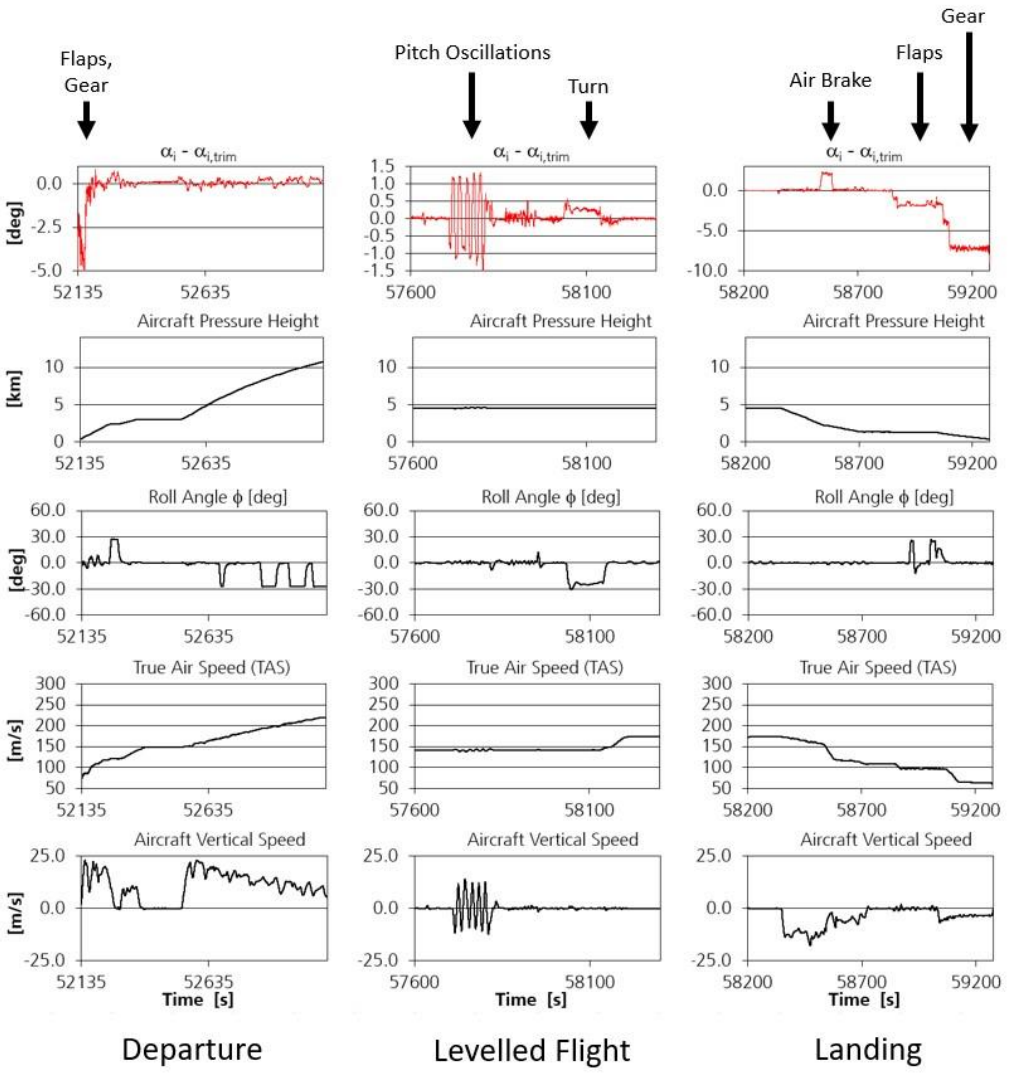

Figure 60*: Difference between α_i and $\alpha_{i,trim}$ and the most important flight parameters for three different flight states (departure, test points on flight level, landing) of the second calibration flight.*

We conclude

- During the pitch maneuvers α_i is symmetrically centered around $\alpha_{i,trim}$, which is in good agreement with the initial idea behind the introduction of $\alpha_{i,trim}$
- An $\alpha_{i,trim}$ parameterization which was calculated for a certain flight level is still close to the expected values for other levels, i.e. $\alpha_{i,trim}$ seems to be a robust parameter.
- During turns α_i shows a systematical positive offset from $\alpha_{i,trim}$
- During ascents and descents $(\alpha_i - \alpha_{i,trim})$ is relatively small as long as the aircraft air brakes, flaps and gear are not deployed.
- Air brakes, flaps and gear have a significant impact on $(\alpha_i - \alpha_{i,trim})$ which becomes very large for these flight states. This is in good agreement with the observed deviations in the α calibration data as shown in Figure 30.

Correction of α

With a properly parameterized $\alpha_{i,trim}$ we can now apply the correction factor k_α to the difference $(\alpha_i - \alpha_{i,trim})$ in the following way.

$$\alpha_{i,new} = \alpha_{i,trim} + k_\alpha \cdot (\alpha_{i,orig} - \alpha_{i,trim}) \qquad \textbf{Equation 22}$$

The result of this correction for the two cases "A" and "B" can be seen in Figure 61. As one can see the final solution according to Equation 22 shows no more offset in the vertical wind data as calculated without these corrections. However, the w modulations caused by the pitch maneuvers have completely vanished and no steps or other signature from the maneuvers are detectable. The natural vertical wind fluctuations now dominate the time series. As one can see this concerns the fast as well as the slow modulations.

Please note that the complete data set on this flight level was processed at once:

- one single $\alpha_{i,trim}$ parameterization from a fit of α_i over qc_i on this level one single time constant dta

- one value for k_α

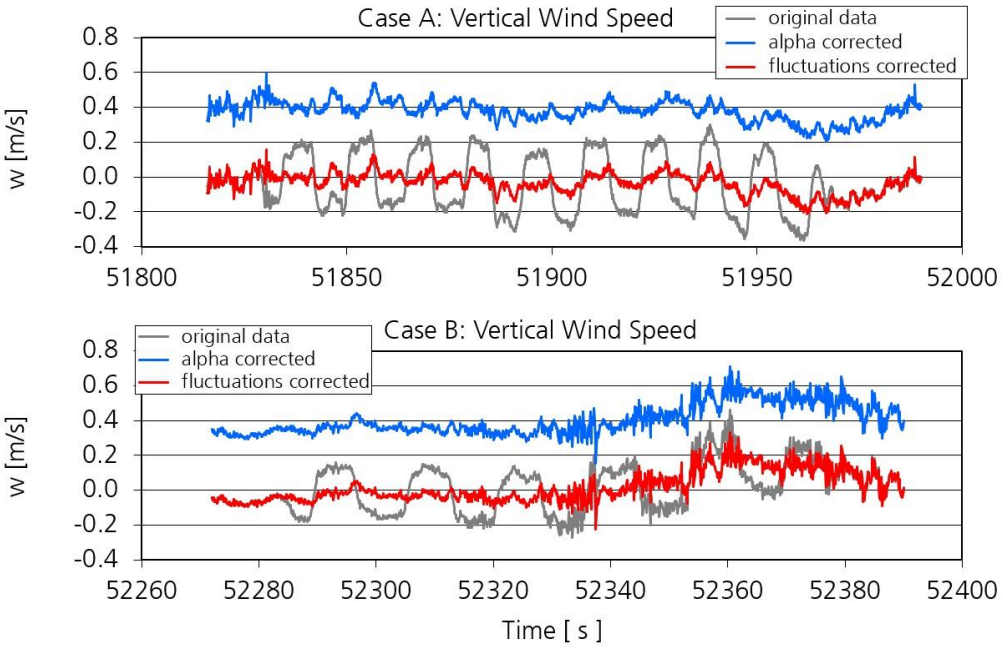

Figure 61*: Final result of the vertical wind data w for the two cases "A" and "B" after application of the complete correction scheme for α_i. The plot shows the original w data, the effect of the k_α correction if applied directly to α and the final solution according to Equation 22 ("fluctuations corrected").*

Parameterization of k_α

As shown above k_α can be defined in different ways:

- acting directly on α (leading to an offset in w)
- acting on the corrected values of the angle of attack, i.e. on $(\alpha - \alpha_{trim})$, where α_{trim} is calculated from a fit of α over qc
- acting on the indicated values of the angle of attack, i.e. on $(\alpha_i - \alpha_{i,trim})$, where $\alpha_{i,trim}$ is calculated from a fit of α_i over qc_i

In all cases the above procedure (minimizing the correlation between vertical wind speed and angle of attack) is applied in order to determine the optimum value for the correction factor k_α.
In order to compare the k_α values from these different cases with each other one must also consider whether the angle of attack was calibrated using the "dynamic angle of attack calibration" which determines just an offset for α or the "static α calibration from regular flight data" which also corrects the slope between α and θ. In this case ("static α calibration from regular flight data") the k_α value found from the data must be corrected with the slope a_1 from that fit.

		k_α applied directly to α		k_α applied to $(\alpha - \alpha_{trim})$		k_α applied to $(\alpha_i - \alpha_{i,trim})$
		α-offset per dynamic offset calibration (ε_b)	α-offset per inflight calibration (a_0, a_1)	α-offset per dynamic offset calibration (ε_b)	α-offset per inflight calibration (a_0, a_1)	α-offset per dynamic offset calibration (ε_b)
TP #	**M_{Ci}**	**k_α (=k1)**	**$k_\alpha \cdot a_1$ (=k2)**	**k_α (=k3)**	**$k_\alpha \cdot a_1$ (=k4)**	**k_α (=k5)**
1	0.4822	1.048	1.049	1.044	1.048	**1.044**
4	0.4830	1.050	1.050	1.048	1.050	**1.048**
5	0.4825	1.048	1.049	1.045	1.048	**1.045**
8	0.4817	1.045	1.046	1.044	1.047	**1.044**
9	0.4811	1.039	1.039	1.038	1.039	**1.038**
12	0.4801	1.050	1.050	1.048	1.049	**1.048**
13	0.4810	1.045	1.046	1.044	1.046	**1.044**
16	0.4798	1.050	1.050	1.048	1.050	**1.048**

Table 8: *k_α values from all test points of flight #1 for different correction schemes.*

Table 8 and Figure 62 prove, that the k_α values from these three options are almost identical i.e. that the correction factor is very robust. Due to this finding it was decided that the complete correction scheme for the angle of attack and the value of k_α refer to **indicated values** which greatly simplifies the data processing.

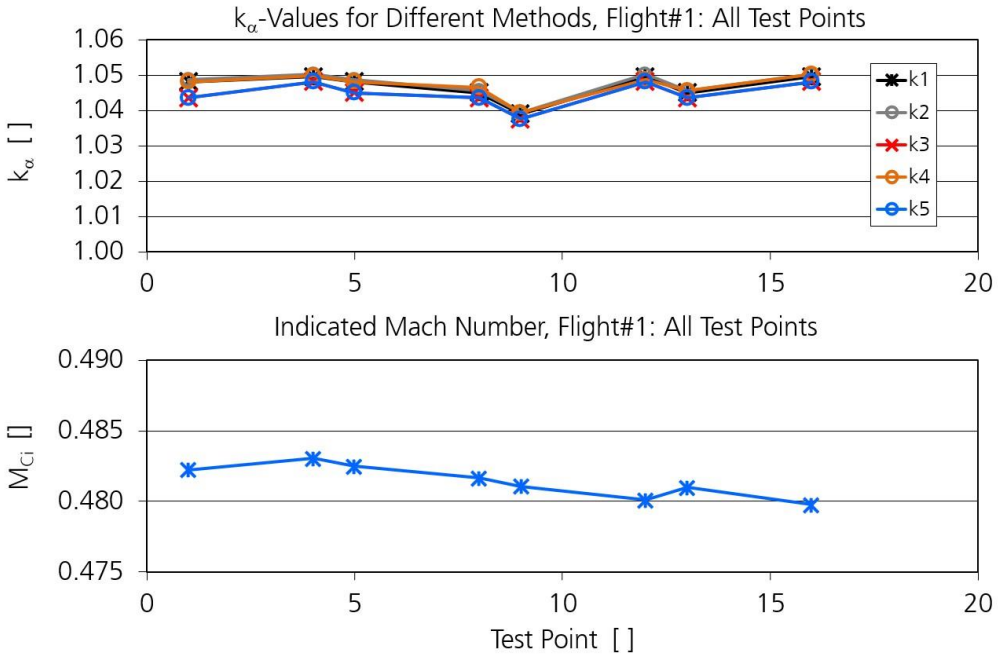

Figure 62*: Comparison of k_α values from different methods and indicated Mach Number M_{Ci} according to Table 8 for flight #1 (17.03.2016).*

As already mentioned above the value of k_α is not constant but depends on the flight conditions. Figure 63 shows the data from all three calibration test flights together with the results from 4 other flight trials where pitch oscillations were flown. The data covers a time period of more than 5 years and contains the test points shown in Figure 62.

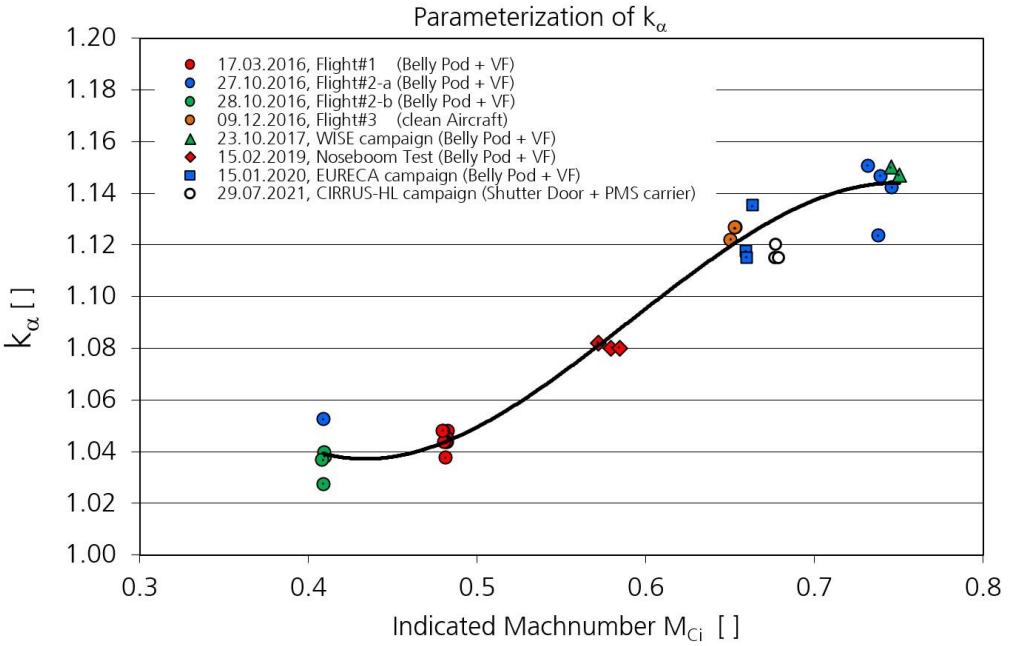

Figure 63*: Parameterization of k_α as a function of the indicated Mach Number M_{Ci}. The plot contains results from other inflight calibration experiments and different aircraft configurations (VF= Ventral Fin). Data from the 2021 CIRRUS-HL campaign is shown for comparison but has not been considered in the parameterization.*

The analysis leads to the following conclusions:

- k_α can be parameterized as a function of the indicated Mach Number M_{Ci}. However, we want to emphasize that different speed parameterizations (true air speed) would also work.
- The data shown covers a time period of almost 4 years. Despite this long time period, the k_α values could be reproduced with a relatively small scatter. This proves that the results are stable and reproducible.
- The little data from other aircraft configurations (clean aircraft, aircraft with belly pod and ventral fin) indicates that aircraft configuration doesn't have a significant influence on the correction factor.

- The result for k_α seems to be independent of the way the maneuvers are flown. Even the two extreme cases of pitch maneuvers shown in Figure 44 do not lead to different results in the determination of k_α.
- The data range of k_α proves that the angle of attack fluctuations as measured directly by the nose boom are **underestimated** by 4-15%. Vertical wind variability generally grows after the correction. This effect becomes larger with increasing aircraft speed.
- Below $\mathrm{M_{Ci}} = 0.4$ the value of k_α is assumed to be constant

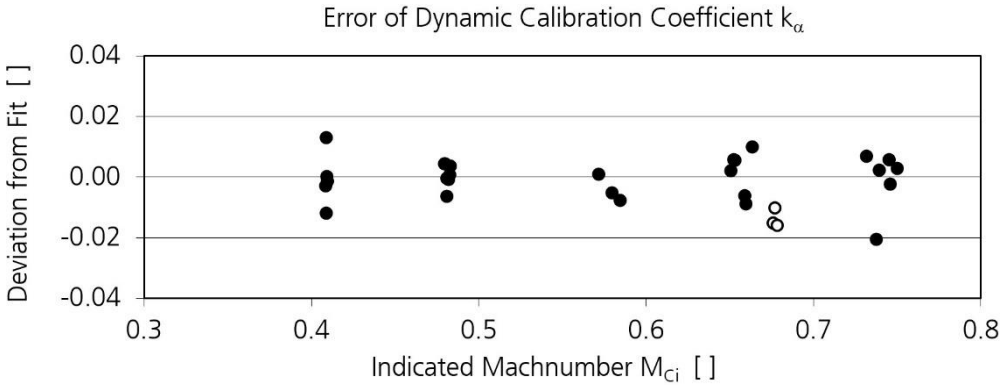

Figure 64*: Deviation of k_α values from the fit in* Figure 63*. The white circles represent data from the 2021 CIRRUS-HL campaign which has not been used for the parameterization.*

Figure 64 shows the deviation between the k_α values which are calculated from the maneuver data and the parameterization (polynomial fit) as shown in Figure 63. This deviation can be treated as the error of k_α since the deviation contains the statistical error of k_α itself as well as possible systematic deviations from a "wrong" parameterization.

The 2σ deviation is found to be 0.0069 (0.69%). This value leads to a $0.69\% \cdot (\alpha_i - \alpha_{i,trim})$ error which is small when compared to the (absolute) error from the static angle of attack calibration which was found to be 0.15° (2σ) over an α_i range of 7°.

Examples for Angle of Attack correction

The following plots show the effect of the presented correction scheme on HALO vertical wind data for the different test flights performed in this study.
The pitch maneuvers can easily be detected in the angle of attack time series. They are also marked with a color overlay.

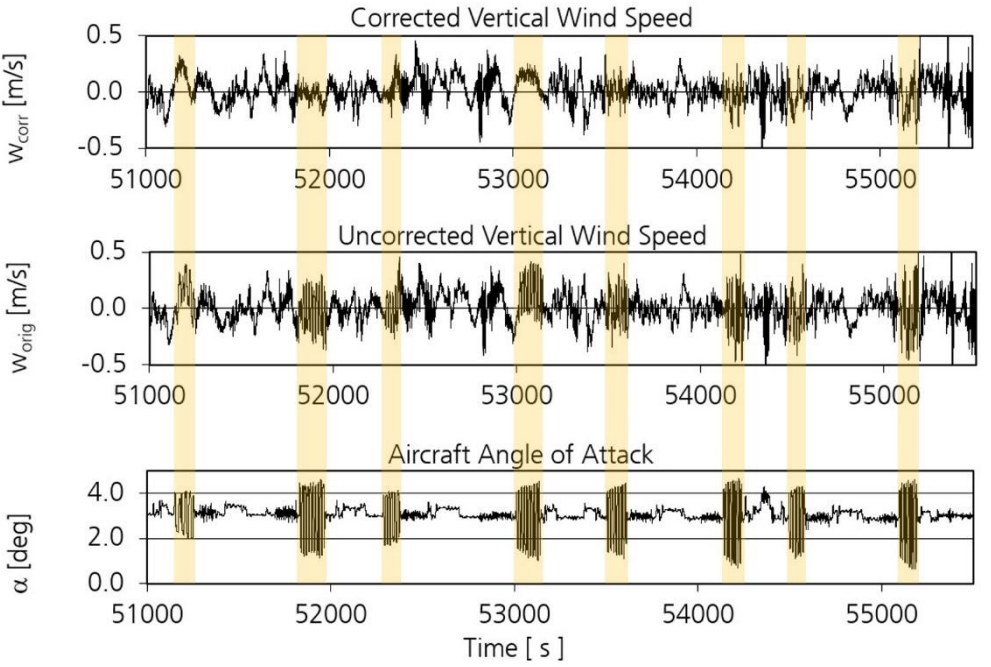

Figure 65*: Original and corrected vertical wind data for the test points of the inflight calibration test flight #1 (according to Table 7). The single test points are marked in yellow. The vertical wind data was corrected using the parameterized k_α as shown in Figure 63. The calculation of α for this flight uses the "dynamic offset calibration".*

The dynamic correction which has been applied to the original data is based on an individual determination of $\alpha_{i,trim}$ and dta for the respective flight level. For short flight levels a typical value of dta had to be chosen instead. The correction always used the general parameterization of k_α as shown in Figure 63.

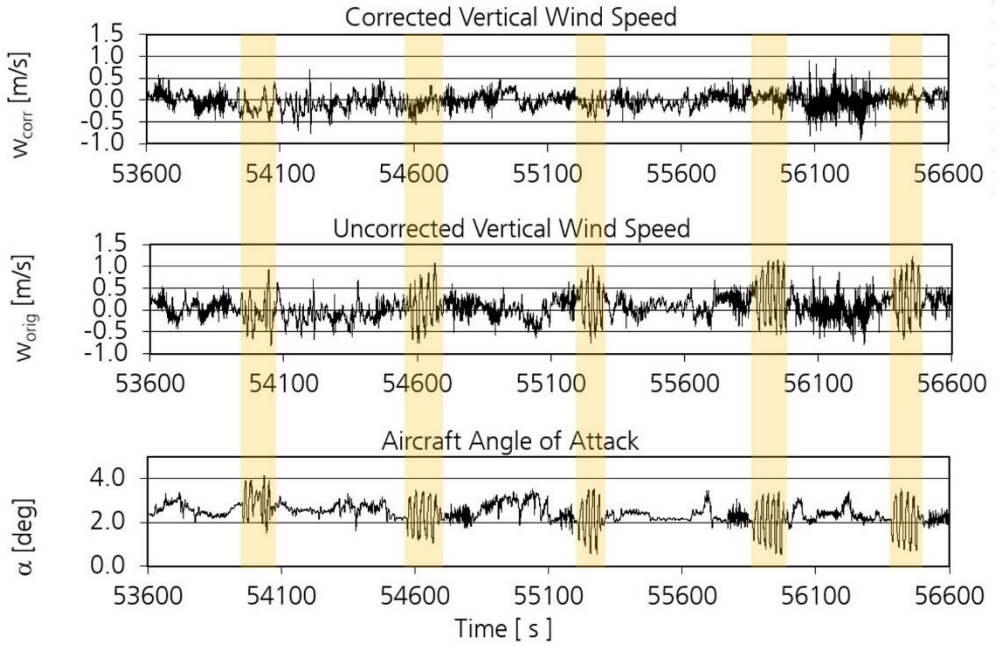

Figure 66*: Original and corrected vertical wind data for the test points of the inflight calibration test flight #2-a (according to Table 7). The single test points are marked in yellow. The vertical wind data was corrected with the parameterized k_α as shown in Figure 63. The calculation of α for this flight uses the "dynamic offset calibration".*

As one can see the procedure works very well. The maneuver induced variations of w are almost completely removed by the correction. This finding is independent of the way the maneuver was flown or the level or shape of the "natural" vertical wind fluctuations.

However, we want to emphasize that the expectation was not to completely remove the complete influence from the maneuver. The main goal of this investigation was to correct the data in a way that all test points satisfy the Lenschow Criterion. As we can see this criterion is well fulfilled by the presented solution. Data from test flight #4 is not shown here, because the flight aimed at the static β calibration and contains only one dynamic yawing and pitching maneuver.

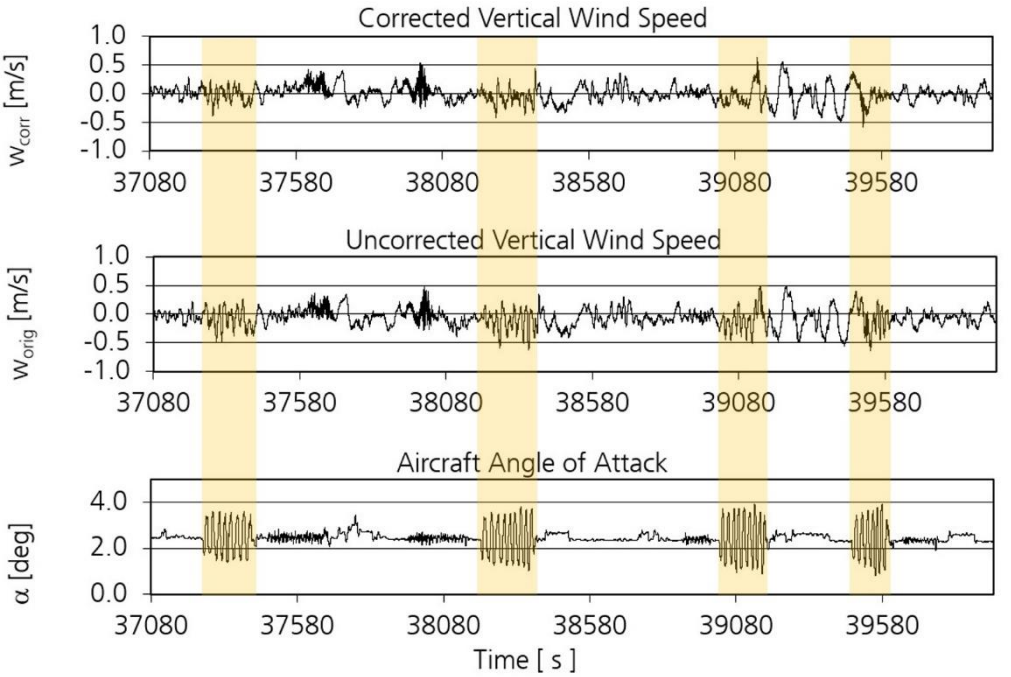

Figure 67*: Original and corrected vertical wind data for the test points of the inflight calibration test flight #2-b (according to Table 7). The single test points are marked in yellow. The vertical wind data was corrected with the parameterized k_α from Figure 63. The calculation of α for this flight uses the "static α calibration from regular flight data".*

A final check concerns the special case shown in Figure 47. Different frequencies of the pitch oscillations for otherwise identical flight conditions led to different results for the Lenschow Criterion.

The respective result can be seen in Figure 68. The first finding is that the value of k_α found for the three different pitch frequencies is identical. The correction obviously doesn't make a difference about how the maneuver is actually flown. If the correction scheme is applied to the data (as mentioned above $\alpha_{i,trim}$ and dta were calculated only once for the whole flight leg and k_α is taken from the general parameterization) we can see that the vertical wind oscillations are

removed from all three sections of this data set. We conclude that the correction scheme works independently of maneuver frequency as well as amplitude and can be treated as a very robust method.

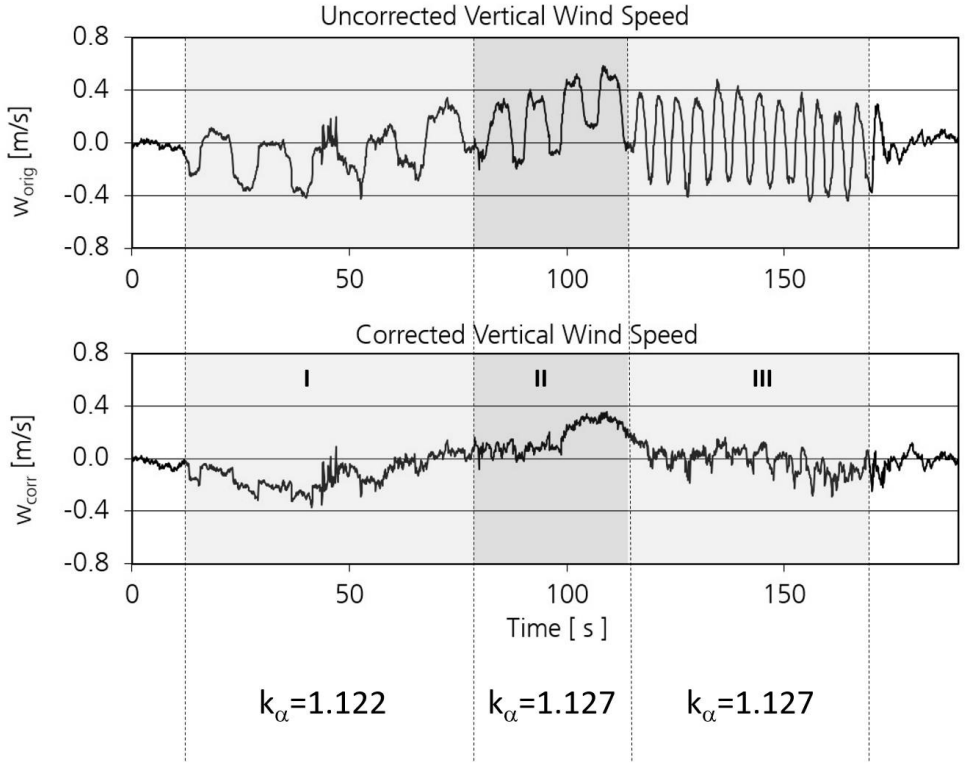

Figure 68*: Original and corrected vertical wind data for the test point shown in Figure 47. The values of k_α for the different pitch maneuver frequencies are found to be identical. Little impact from the maneuvers can be seen in the corrected vertical wind data since the correction is based on the parameterized k_α as shown in Figure 63 and not on the individual value of k_α for this test point.*

Pressure dependency on dynamic alpha

A final investigation of the pitch oscillation test points concerned the impact of dynamic maneuvers on the aircraft static pressure measurement. This can be done after removing the pressure variations caused by the changes in aircraft altitude according to Equation 15. The corrected static pressure data during the maneuver is then compared to the values taken from the reference measurements at the start and end of the test point (as shown in Figure 42 and Figure 43). The assumption of a linear trend between these two points further decreases the influence of atmospheric variations on the reference data.

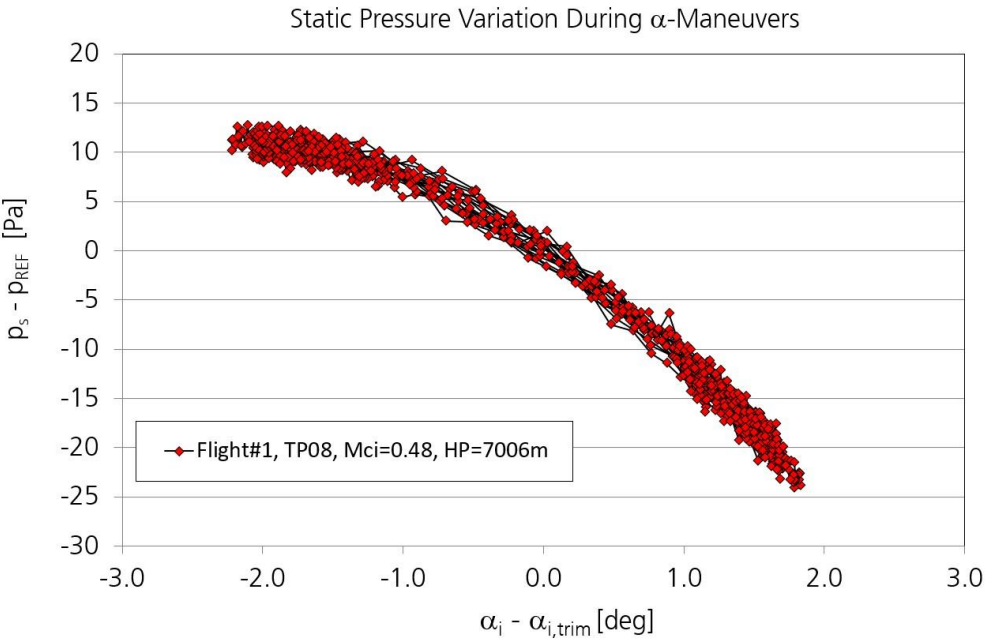

Figure 69*: Dependence of static pressure on $(\alpha_i - \alpha_{i,trim})$. The plot shows 10Hz data from a single test point of the first calibration flight. The data points represent the deviation of the static pressure which has already been corrected for static source error, static beta dependence and altitude changes (according to Equation 15) from the reference pressure measured just before/after the actual maneuver (HP = pressure height).*

It is important to note that the static pressure data must be corrected for static source error and static beta dependence before this analysis.
Figure *69* shows the respective 10Hz data for a single pitch oscillation test point of the first test flight. Please note that the data contains several "swings" through the shown data range.

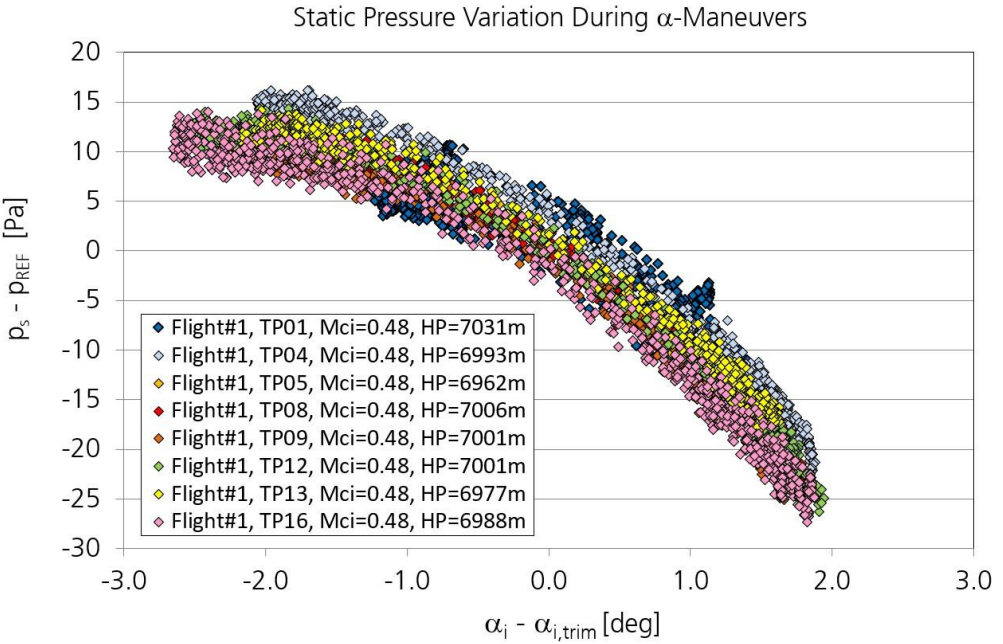

Figure 70*: Dependence of static pressure on* $(\alpha_i - \alpha_{i,trim})$***. The plot shows the same data as* Figure 69 *but includes all test points on this height level. All test points were flown with the same flight parameters (speed and altitude).***

From the data we can conclude:

- A systematic dependency of the static pressure on $(\alpha_i - \alpha_{i,trim})$ can be observed during the pitch oscillations.
- The data shows the extreme accuracy of the BAHAMAS instrumentation: The noise level (deviation of data from the fit through the curve in Figure *69*) is 1.9Pa (2σ value). This means that the IRS altitude data (used in the

height correction of the pressure) and the pressure sensors (stability/drift and noise level) do not cause a significant statistical error in the data.

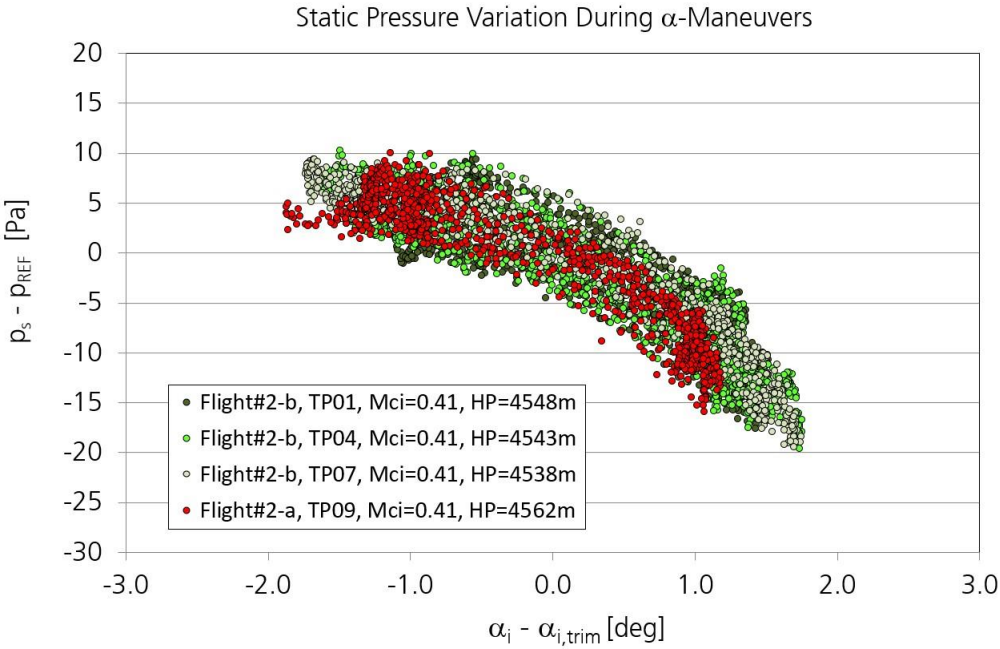

Figure 71*: Dependence of static pressure on $(\alpha_i - \alpha_{i,trim})$ for identical test points from different flights*

Figure 70 shows the respective result for all 8 test points from this flight which were flown under identical flight conditions. As one can see the reproducibility of the result is excellent.

Figure 71 proves that the results do not change from flight to flight and can be seen as reliable and representative.

However, we can see from Figure 72 that the relation between $(p_s - p_{REF})$ and $(\alpha_i - \alpha_{i,trim})$ depends on flight conditions. At different speed and/or altitude the shape of the relation changes. However, the available data set does not allow to parameterize this relation.

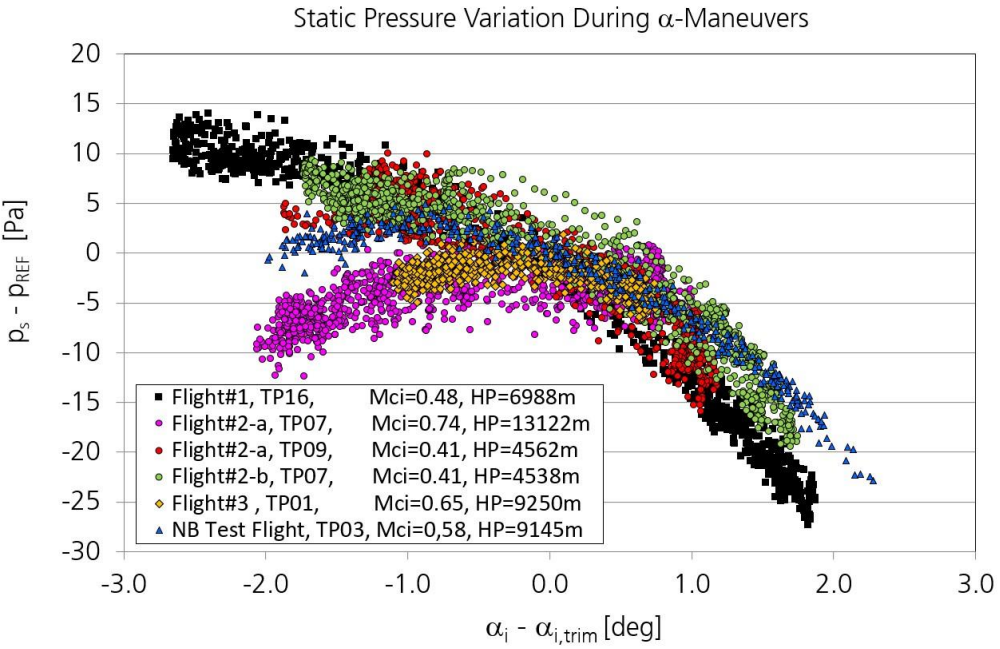

Figure 72*: Dependence of static pressure on $(\alpha_i - \alpha_{i,trim})$ for test points flown under different flight conditions and on different days. "NB Test Flight" is data from another experiment.*

As one can see from the flight test data (for example Figure 55) the observed range of $(\alpha_i - \alpha_{i,trim})$ during flight is very small, a typical value is $\pm 0.5°$ during regular flight conditions. Even under turbulent conditions in a convective boundary layer this difference rarely exceeds $\pm 1°$. As can be seen in Figure 72 the respective static pressure change is smaller than 15Pa, which is the same order of magnitude as the calibration limit of the pressure sensors on HALO. Therefore, we can state that the major contribution to the angle of attack pressure correction is given by the static calibration.

Dynamic Beta-Calibration

The strategy for the dynamic angle of sideslip calibration follows the ideas which were developed for the angle of attack. The goal is to reduce the existing crosstalk of the sideslip maneuvers into the **horizontal** wind data by „optimizing" β_i according to

$$\beta_{i,new} = k_\beta \cdot \beta_{i,orig} + d\beta_i \qquad \textbf{Equation 23}$$

As in case of α we apply the correction factor directly to the indicated value β_i. However, some differences to the angle of attack procedure are obvious:

- Since the mean angle of sideslip is zero, an "offset problem" from the k_β application to $\beta_{i,orig}$ does not exist. There is no need for a $\beta_{i,trim}$ and k_β can be applied directly to β_i. This greatly simplifies the correction.
- The determination of k_β by minimizing the correlation between β_{new} and "the horizontal wind" offers multiple options since the horizontal wind is 2-dimensional. We decided to analyze the correlation of β_{new} with the two units "wind speed" ws and "wind direction" (wind angle) wa.

As for the angle of attack we will present the results for two different test points from the first test flight. The two cases have a different heading with respect to the horizontal wind direction: along ("Case A") and perpendicular ("Case B").

Flow Angle Calibration

Figure 73 shows the data from the two cases (test points 2+11 from flight #1) before any correction has been applied to the data. One can see that the impact of the maneuver on the wind data depends on the relative orientation between aircraft heading and the horizontal wind direction. When the aircraft flies along the wind an impact of the β oscillations can only be seen in the horizontal wind direction data while the wind speed shows no visible oscillation. If the aircraft flies perpendicular to the horizontal wind the effect is reversed. The oscillations are

present in the wind speed data while the wind direction does not seem to be influenced by the maneuver at all.

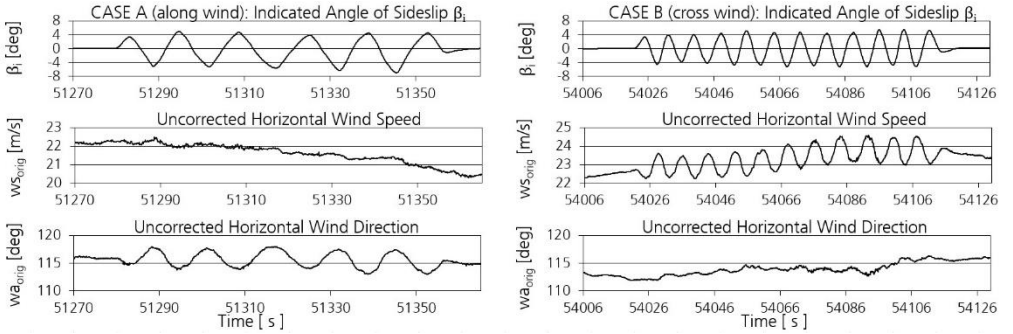

Figure 73*: The effect of β maneuvers on horizontal wind data. The effect strongly depends on the relative orientation of horizontal wind direction and aircraft heading.*

As in case of the angle of attack the determination of an optimum correction for β_i proved that the introduction of an offset $d\beta_i$ did not give useful results and that k_β turned out to be the sensible parameter. Figure 74 shows the result of the correlation analysis.

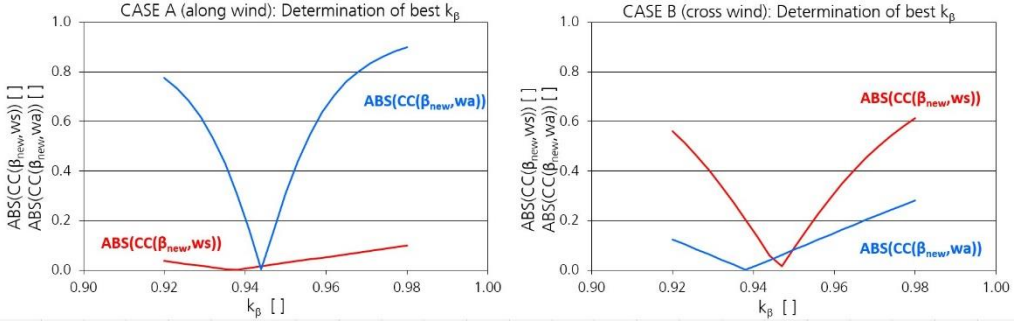

Figure 74*: Determination of an optimum correction factor k_β in Equation 23 which minimizes the absolute value of the correlation factor between β_i and the horizontal wind speed ws ($CC(\beta_i, ws)$) and/or the horizontal wind direction wa ($CC(\beta_i, wa)$) during yaw oscillation maneuvers.*

From Figure 73 it becomes clear that the correlation $\mathrm{CC}(\beta_i, \mathrm{wa})$ is the sensible correlation for flight legs along the wind direction while $\mathrm{CC}(\beta_i, \mathrm{ws})$ should be used for the cross-wind legs. However, it is remarkable that in both cases the "weaker" correlation also yields a shallow minimum for a k_β in the vicinity of the value found from the dominant parameter.
The effect of the β correction on the wind data can be seen in Figure 75 and Figure 76. In all cases k_β is directly applied to β_i.

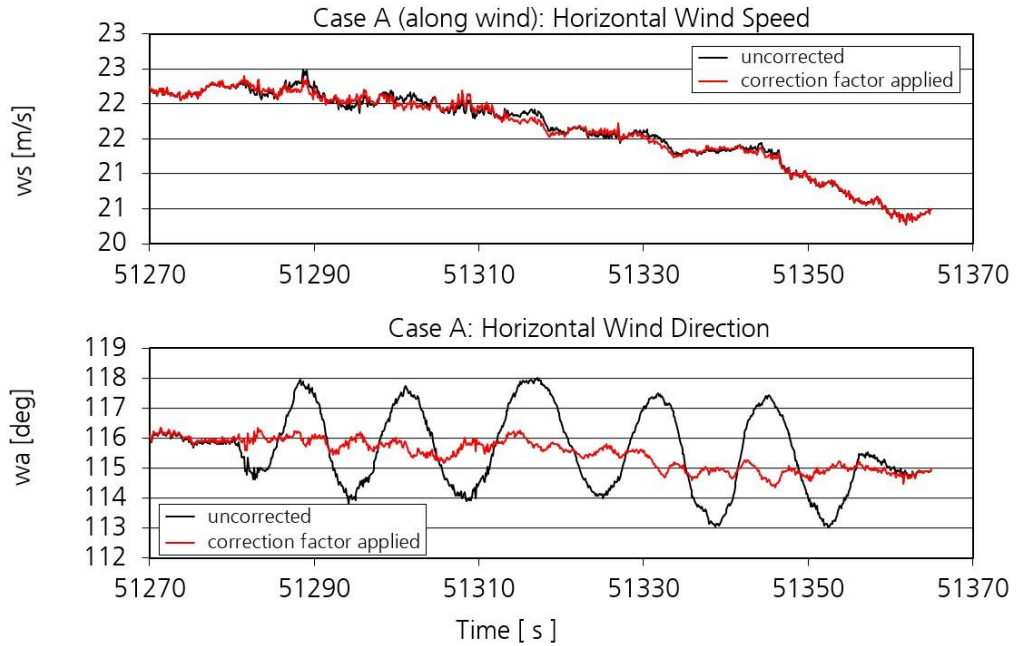

Figure 75: ***Effect of dynamic angle of sideslip correction on horizontal wind data for test point #2 from the first calibration flight. The aircraft is flying along the horizontal wind.***

On the flight track along the wind the application of the correction factor k_β eliminates almost completely the modulations in wind direction data which were caused by the maneuver while the corrections in the wind speed data remain very small. The atmospheric high frequency variations of ws and wa become visible in

the data while the mean values of wind speed and wind direction are not changed by the correction.

The result for the cross-wind leg is similar: The modulations in horizontal wind speed vanish almost completely while the wind direction data shows only small changes. However, one can see in both plots that a small "ripple" remains in the corrected data. This is due to the extreme sideslip maneuvers which were flown during this first test flight. The aircraft reached angles of sideslip of up to 7° which is way beyond the typical data range of β during a regular flight. We will later see that for typical values of β the correction leaves practically no maneuver footprint in the data.

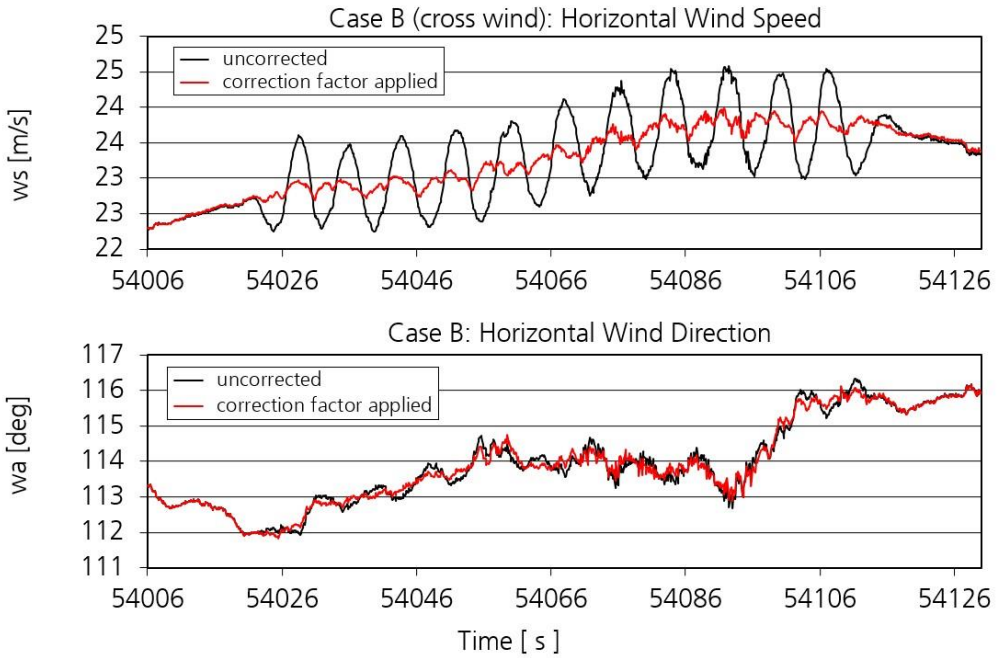

Figure 76*: Effect of dynamic angle of sideslip correction on horizontal wind data for test point #11 from the first calibration flight. The aircraft is flying perpendicular to the horizontal wind.*

It is interesting to note that the value of k_β found for the test points of flight #1 means that β and therefore the horizontal wind fluctuations are overestimated which is in contradiction to the result for α which was found for the same flight conditions.

Parameterization of k_β

During the 8 test points of flight #1 which were flown under identical conditions k_β was found to be constant. Table 9 lists the results for all test points.

TP #	horizontal wind direction	Determination of k_β from correlation with	M_{Ci}	k_β
2	back	wind direction	0.4804	**0.944**
3	front	wind direction	0.4826	**0.946**
6	back	wind direction	0.4837	**0.946**
7	front	wind direction	0.4828	**0.944**
10	right	wind speed	0.4832	**0.946**
11	left	wind speed	0.4839	**0.946**
14	right	wind speed	0.4838	**0.945**
15	left	wind speed	0.4833	**0.941**

Table 9: *$k_\beta$values from all test points of flight #1.*

Figure 77 shows the small variation of k_β between the different yaw oscillation maneuver test points of flight #1.

One can see from Table 9 the systematic relation between relative wind direction and sensible wind parameter in the correlation analysis as well as the small k_β variance. Again, the correction seems to be very stable and the results significant. Figure 77 visualizes this result and indicates that the remaining variation of k_β can be attributed to changes in the aircraft indicated Mach Number M_{Ci} which was less obvious in case of k_α (Figure 62).

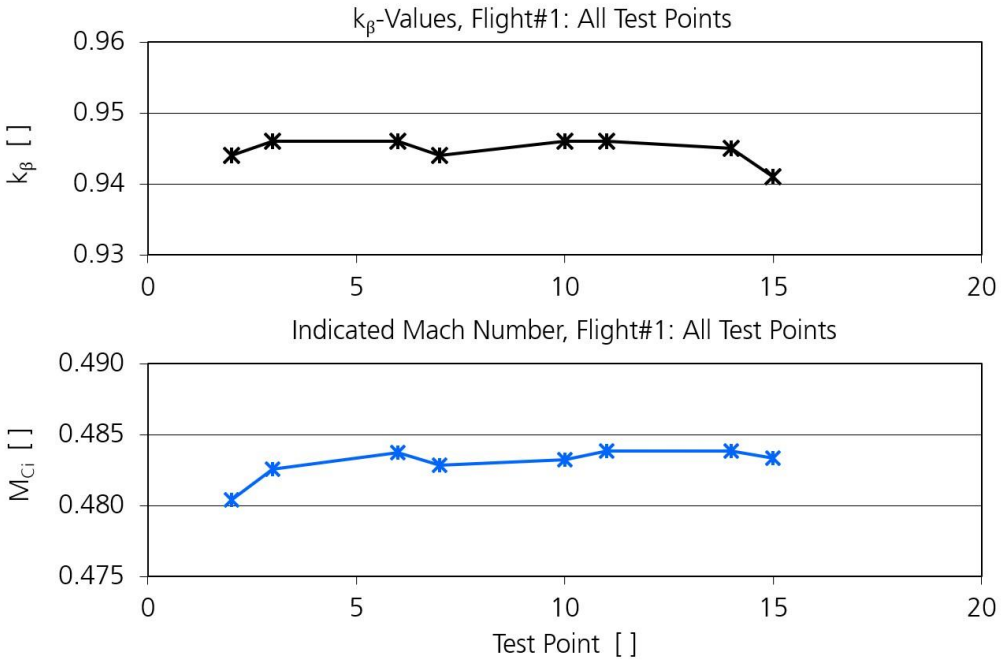

Figure *77: Comparison of k_β from different test points of Flight #1 (17.03.2016) and the respective indicated Mach Numbers M_{Ci} according to Table 9.*

As already found for the angle of attack the correction factor k_β is not constant but changes with the flight conditions. Again, it was decided to parameterize k_β as a function of M_{Ci}.

Figure 78 shows the result of this parameterization. The plot contains data from this flight test as well as from other inflight calibration campaigns with HALO over a time period of more than 5 years. One can see that the relation between k_β and M_{Ci} is almost linear and thus different from the result found for the angle of attack. At low Mach Numbers the directly measured value of β_i is overestimated while at high speeds β_i is too large. Figure 78 also proves that the data can well be reproduced even from flights which took place one year later than the other ($@\ M_{Ci} = 0.6$). The large scatter at high Mach Numbers is explained by the fact

that the maneuver is very difficult to perform at high altitude and high Mach Numbers. However, further flight testing is required to reduce the uncertainty in this speed range.
For indicated Mach Numbers below 0.4 the linear relation is extrapolated.

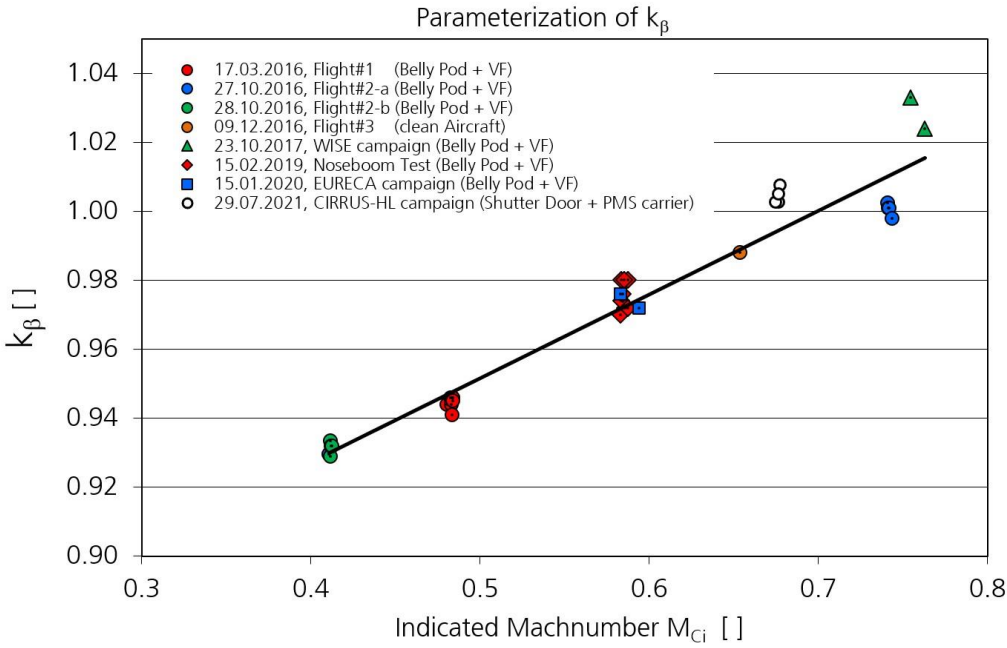

Figure 78*: Parameterization of k_β as a function of the indicated Mach Number M_{Ci}. The plot contains results from other inflight calibration experiments and different aircraft configurations (VF= Ventral Fin). Data from the 2021 CIRRUS-HL campaign is shown for comparison but has not been considered in the parameterization.*

The determination of a dynamic correction for β means that β_i is scaled twice with a linear correction factor. The first time with the result from the static calibration according to Figure 37 and a second time with the k_β from the dynamic calibration. It is important to emphasize that the dynamic correction applies to dynamic changes only which are caused by wind fluctuations and deviate from

the mean β_i (which is usually zero). If the aircraft flies a steady sideslip k_β must not be applied to β_i which is for example the case during the yaw step maneuvers of the static β calibration. However, during regular flight conditions all non-zero values of β_i can usually be attributed to fast wind fluctuations and are therefore subject to the dynamic correction.

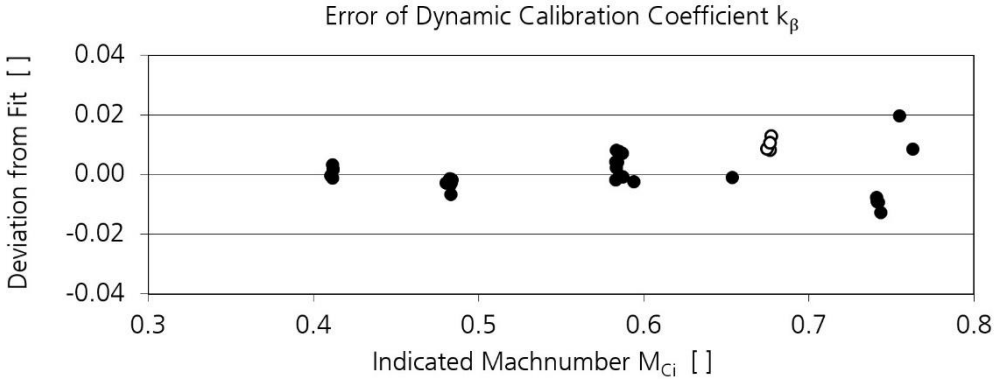

Figure 79*: Deviation of k_β values from the fit in* Figure 78*. The white circles represent data from the 2021 CIRRUS-HL campaign which has not been used for the parameterization.*

Figure 79 shows the deviation between the k_β values which are calculated from the maneuver data and the parameterization (linear fit) as shown in Figure 78. As stated above for k_α the 2σ value of this plot is treated as the error of k_β. It was found to be 0.0064 (0.64%). As shown above the absolute error from the static β calibration was found to be 0.22°.
We can therefore state that the uncertainty from the dynamic correction of $0.64\% \cdot \beta_i$ is small when compared to the result from the static angle of sideslip calibration of 0.22° (2σ) over a β_i range of 10°.

Examples for Angle of sideslip correction

We now want to present the effect of the dynamic calibration for other beta maneuvers from this flight test. Please note that all following plots show data

which was subject to a standard dynamic correction of α and β based on the general parameterization of $k_\alpha$and k_β as shown in Figure 63 and Figure 78 (This was also the case for the plots shown in Figure 65 - Figure 68 before). The only flight specific calculation concerns $\alpha_{i,trim}$ i.e. the determination of dta and the fit between α_i and β on the respective flight level.

Figure 80 gives an overview on the yaw oscillation test points of flight #1 (it also contains all pitch oscillation maneuvers which have no impact on the horizontal wind).

The plot visualizes the above result that the test points with aircraft heading along the main wind direction (TP 2,3,6,7) impact the wind direction only while the cross-wind maneuvers (TP 10,11,14,15) create a modulation in wind speed.

Figure 80 also indicates that the test flight took place in a heterogeneous atmosphere with prominent horizontal and (as we see later) vertical structures in the wind field. Strong horizontal wind speed gradients can be seen in the data and the plot indicates that this structure seems to be stationary for at least the second half of the test flight.

The structure can be used to check the quality and reproducibility of the aircraft wind measurements. We therefore analyze the right-hand side of Figure 80 which contains 8 test points (TP 9-16). The 30 min section of the test flight consists of four cross wind flight legs with 1 pitching + 1 yawing maneuver each and three 180° turns. This allows to also investigate the effect of opposite heading maneuvers on the HALO wind speed measurements.

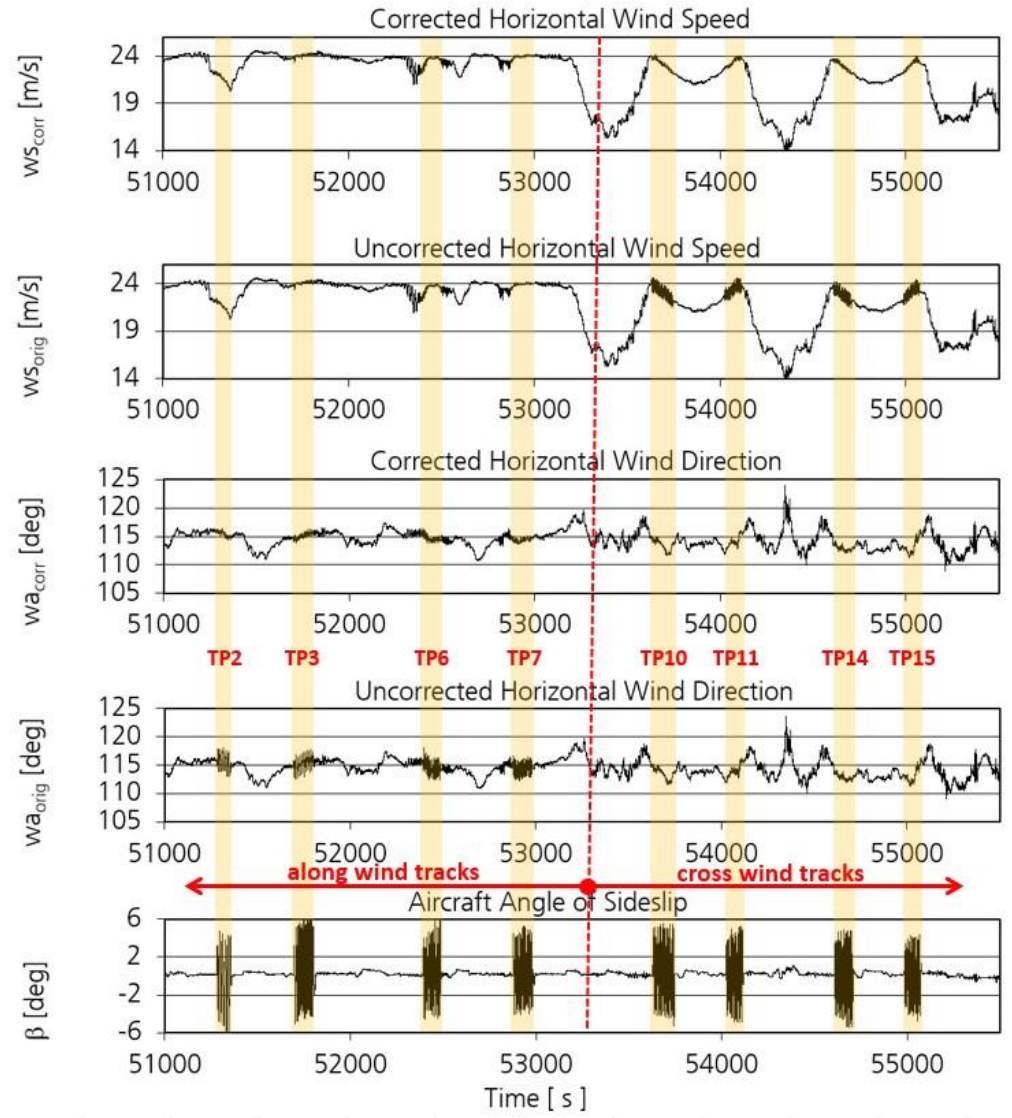

Figure 80*: Original and corrected horizontal wind data for the test points of the inflight calibration test flight#1 (according to Table 7). The single test points are marked in yellow. The wind data was corrected with the parameterized values of k_α and k_β from Figure 63 and Figure 78.*

Figure 81 shows the result of the wind speed measurement during the following maneuvers:

- wind from behind: α-oscillation, β-oscillation, 180° turn
- wind from front: β-oscillation, α-oscillation, 180° turn
- wind from behind: α-oscillation, β-oscillation, 180° turn
- wind from front: β-oscillation, α-oscillation

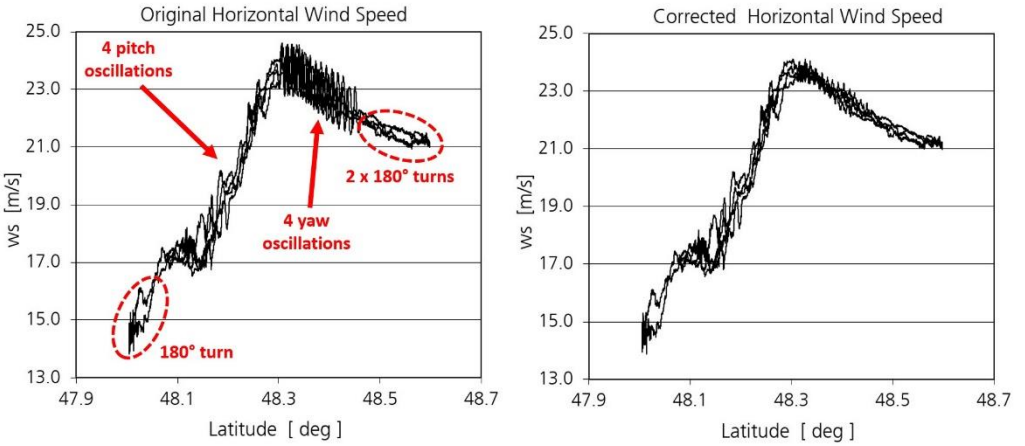

Figure 81*: Horizontal wind data for all 4 cross wind legs of flight #1 plotted over geographic latitude. The 30 min data set contains four flight legs, eight test points with oscillation maneuvers and three 180° turns.*

Figure 81 shows the original wind data and the result from the dynamic correction of the airflow angles based on the general parameterization of k_α and k_β . From the plot we conclude that

- The horizontal wind field was mostly stable during the time interval of the investigation, some temporal variations are visible in the strong gradient between 48.1° and 48.2° latitude.
- The aircraft wind measurement is able to reproduce the wind data with an accuracy of at least 0.5m/s. This number includes possible deviations caused by wind variations during the measurement.
- The result is independent of opposite heading measurements

- The parameterized correction eliminates almost all of the horizontal wind speed variations.
- No impact of the pitching maneuvers on horizontal wind measurements can be seen in the data.
- The wind measurement does not seem to be influenced by the 180° turns. The turns at lower latitude are subject to temporal variations of the horizontal wind field (as already found above). At high latitude the wind structure shows no impact from the turn. It seems that the correction further reduces the error of the wind measurement since the corrected data matches better than the original wind measurement.

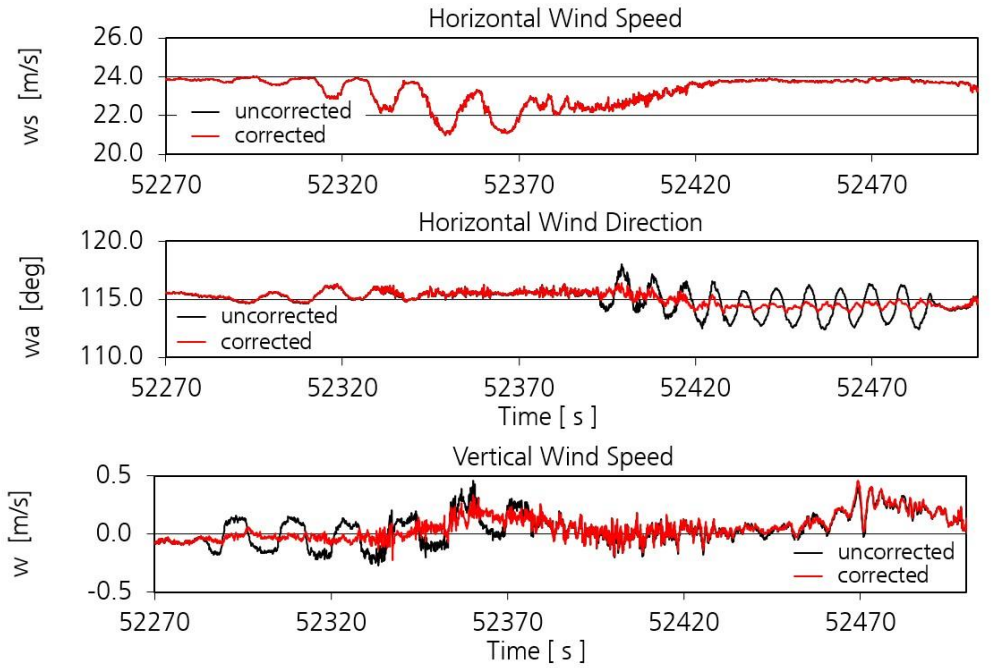

Figure 82*: Original and corrected wind data from the test points TP5 (pitching oscillation) and TP6 (yawing oscillation) of test flight #1.*

Keeping in mind that the atmospheric wind field cannot be completely stationary this is an excellent result which proves the quality of the HALO wind measurement system.

A second interesting case from flight #1 are the test points TP5 (pitching oscillation) and TP6 (yawing oscillation) on the same (wind from behind) leg. Figure 82 shows original and corrected horizontal and vertical wind data during both maneuvers. The surprising observation is that all three wind parameters show a harmonic modulation during the pitch maneuver. However, the dynamic correction works on the vertical wind data only while the modulation in horizontal wind data during the maneuver remains unchanged. The following yawing oscillation gives the expected result: only horizontal wind direction is influenced by the maneuver and the correction scheme eliminates this signature in the data.

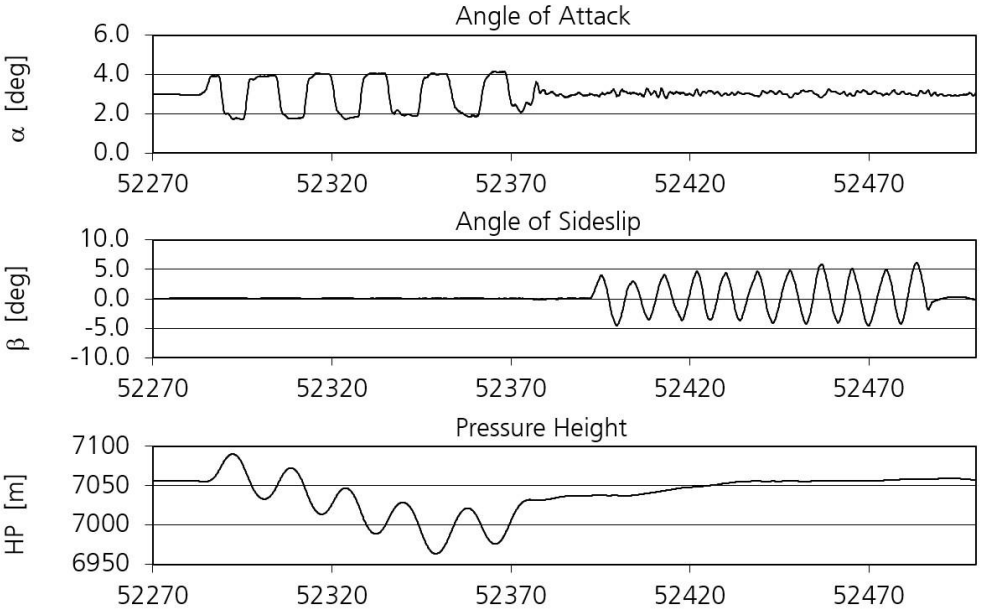

Figure 83*: Flow angles and aircraft altitude during the time interval of Figure 82.*

In order to analyze this phenomenon, we have to check the aircraft state during the maneuver which is shown in Figure 83. The data proves that the oscillation maneuvers were flown properly: no mixing of airflow angle during a single test point occurs which would explain a signature in all three wind parameters. However, one can see that the aircraft lost height during the pitch oscillations.
An analysis of the vertical atmospheric wind structure provides the explanation for the observed data. Figure 84 shows that the test flight took place in a strong vertical wind speed gradient. Therefore, the loss of altitude during the pitch maneuver led to a harmonic variation in wind speed and direction.

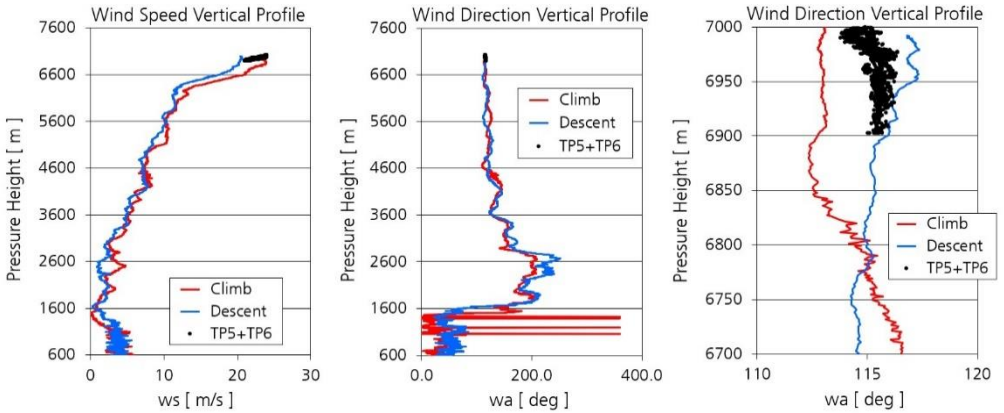

Figure 84*: Vertical structure of the atmosphere during the first test flight. The wind direction data from the pitch oscillation maneuver is shown in the right plot in order to prove the plausibility of the data.*

Despite the fact that the atmospheric conditions were not optimum during the experiment the case proves the robustness of the calibration method and the correction scheme. The calibration factors of $k_\alpha$and k_β from these two test points are consistent with the data from the other flights.

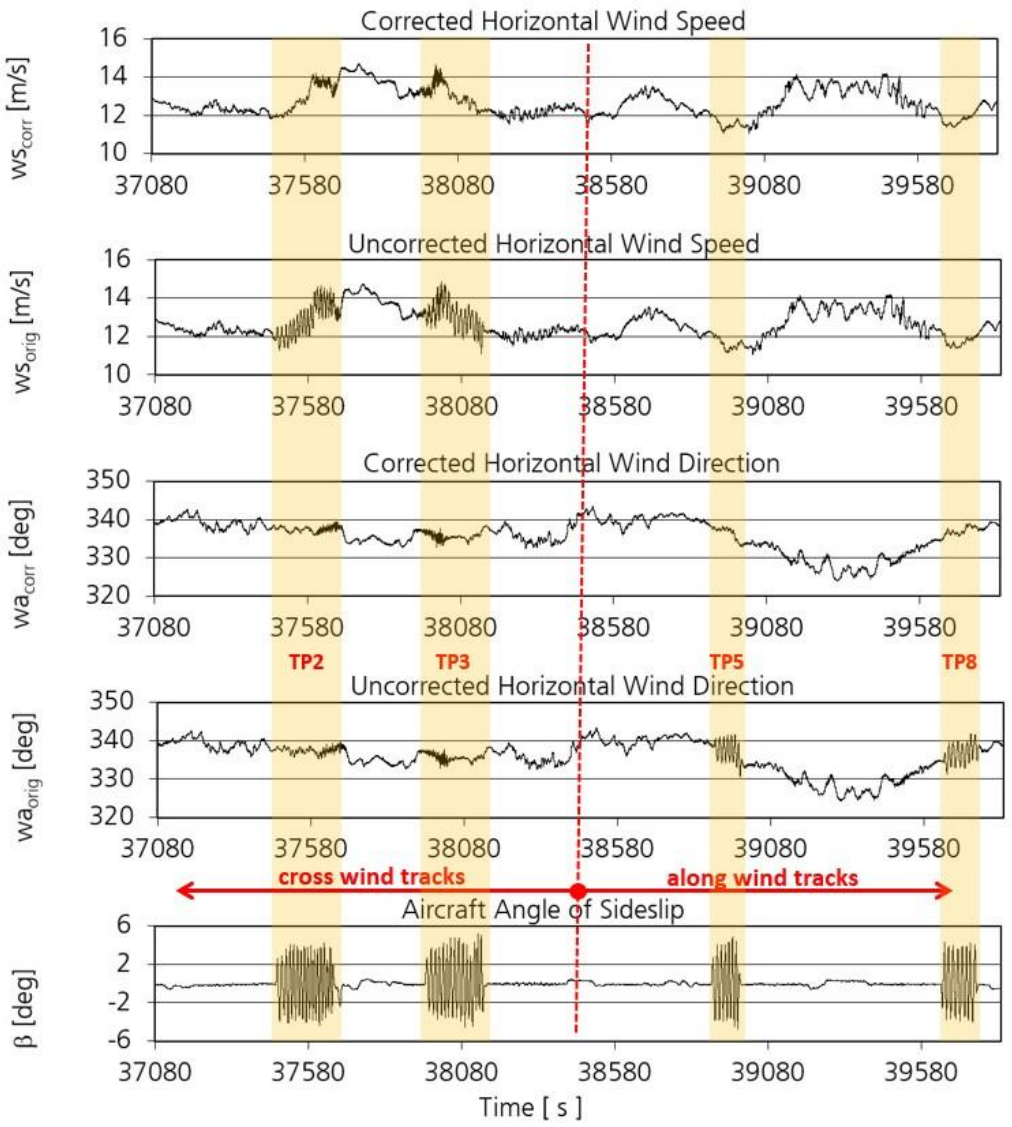

Figure 85*: Flight #2-b Original and corrected horizontal wind data for the test points of the inflight calibration test flight#2-b (according to Table 7). The single test points are marked in yellow. The wind data was corrected with the parameterized values of k_α andk_β from Figure 63 and Figure 78.*

The overview plot for Flight #2-a (similar to Figure 80) is not shown here. As can be seen from Figure 78 all test points from this flight were flown for identical flight parameters (M_{Cl}=0.74) where the value of k_β was found to be 1. This means that no modulation from the β oscillation maneuver could be found in the wind data of Flight #2-a and that the correction did not change the original time series.
The respective data for Flight #2-b can be seen in Figure 85. As mentioned before this data set uses the "static α calibration from regular flight data". Again, the impact of the relative wind direction on the different horizontal wind data parameters can clearly be seen in the time series. The correction works well and the artificial modulation of the wind speed and wind direction seems to be completely removed.
However Figure 85 indicates an increased residual variance after correction during parts of the test points TP2 and TP3 (A similar phenomenon can be observed in Figure 80 during the test points TP3 and TP6). In order to investigate this observation, we plot the respective wind data with/without the correction as a function of a geographic coordinate (longitude) which is shown in Figure 86. From this plot it becomes immediately clear that the observed "roughness" in the wind data is a real local wind structure associated with atmospheric turbulence.

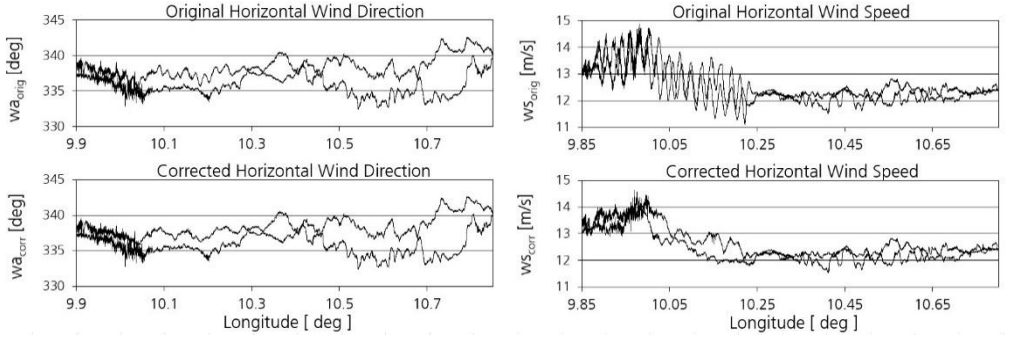

Figure 86*: Plot of the horizontal wind data from the cross-wind legs in Figure 85 over geographical longitude. The plot proves that the visible roughness in wind speed and direction is a spatial effect which has nothing to do with the aircraft maneuvers. Note the removal of the small wind angle modulations (cross wind leg!) by the dynamic correction.*

The data also shows that the cross-wind maneuver creates a small signature in the wind direction which is removed by the correction. A closer look into the data explains this observation. The maneuvers of these test points were not flown exactly perpendicular to the wind direction but with an offset of 10°. In this case the correlation analysis for wind direction and wind speed will give separate results. Figure 87 shows both correlations for TP3. The minima of both curves are close to each other which again proves the robustness of the method.

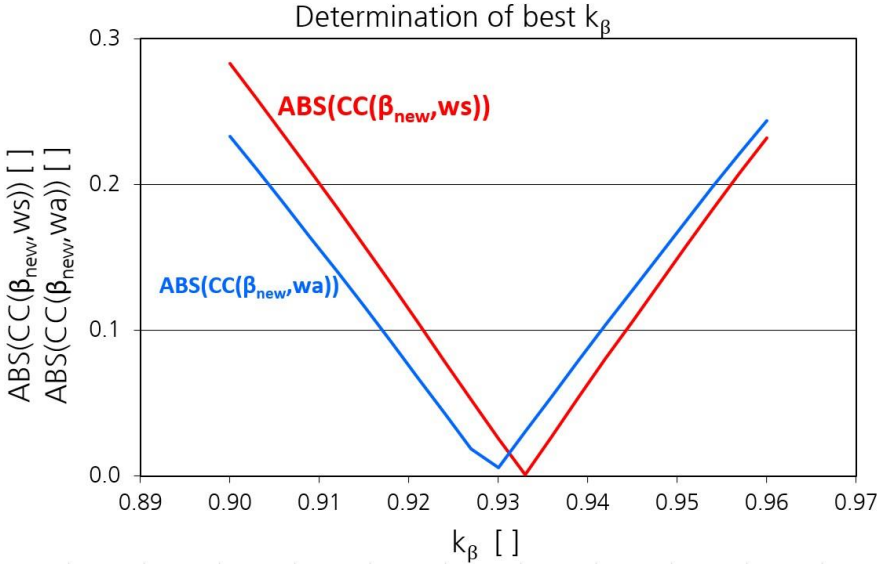

Figure 87*: Determination of k_β for a flight where the heading is not perfectly aligned with the horizontal wind direction.*

However, the minimum of the wind speed modulation was chosen to determine the right value for k_β since the relative wind direction is much closer to a cross wind scenario.

Figure 88 shows the wind data of TP3 before and after the correction. One can nicely see the effect of the correction on both wind parameters. The correction works for wind speed and wind direction simultaneously and leaves the natural variations in the time series only.

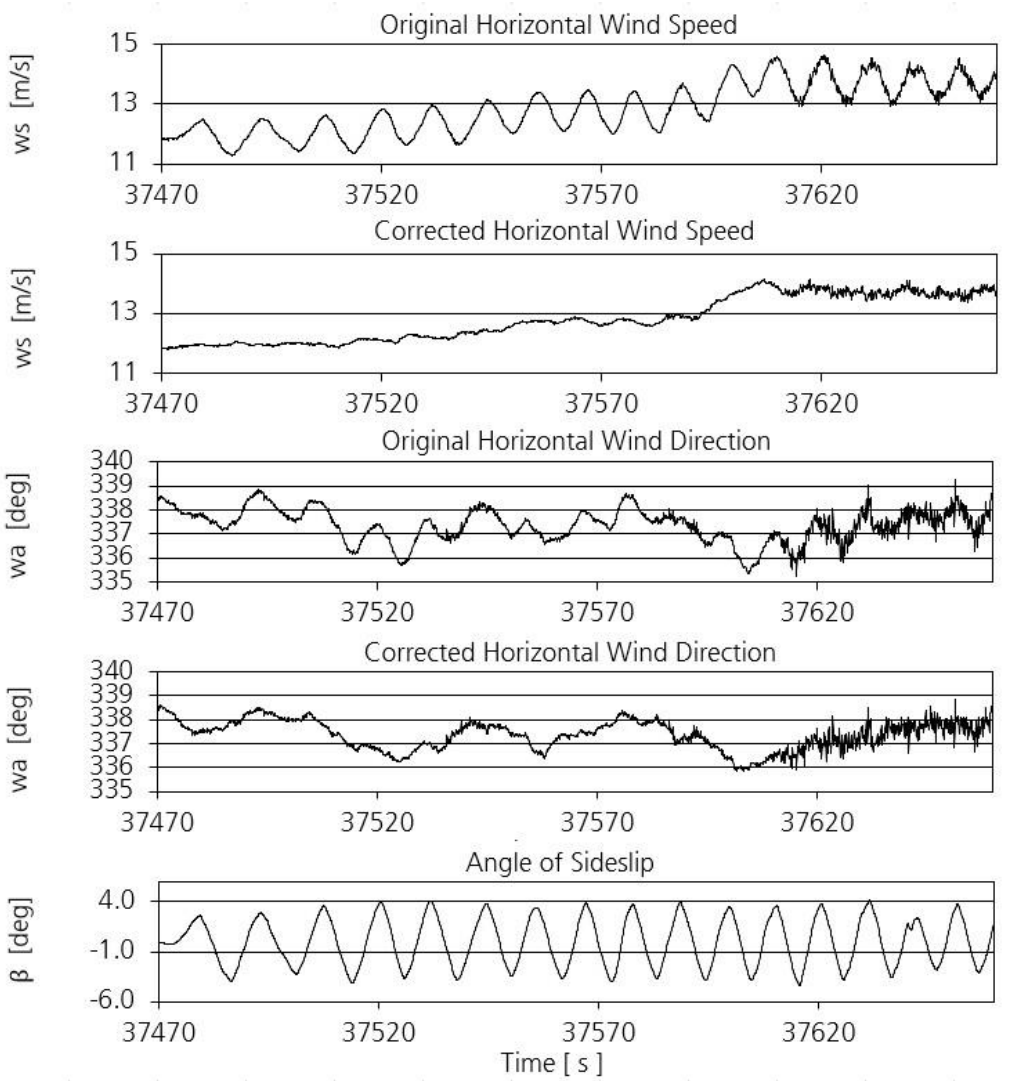

Figure 88*: Dynamic correction for a cross wind test point (TP3 of flight #2-b) which is not perfectly aligned with the main horizontal wind direction. A 10° directional offset also results in a visible oscillation in wind direction. However, the correction scheme works simultaneously on both wind parameters with the same value of* k_β*.*

As already mentioned in the analysis of test flight #1 the significantly smaller β amplitudes and smoother oscillation maneuvers during this flight allow for a complete correction of the artificial wind modulations.

Pressure dependency on dynamic beta

The investigation on the influence of dynamic β maneuvers on the static pressure measurement were performed the same way as for the angle of attack. The pressure changes caused by aircraft altitude variations were removed in order to relate the pressure data to the value determined during the reference measurement taken before and after the actual test point.

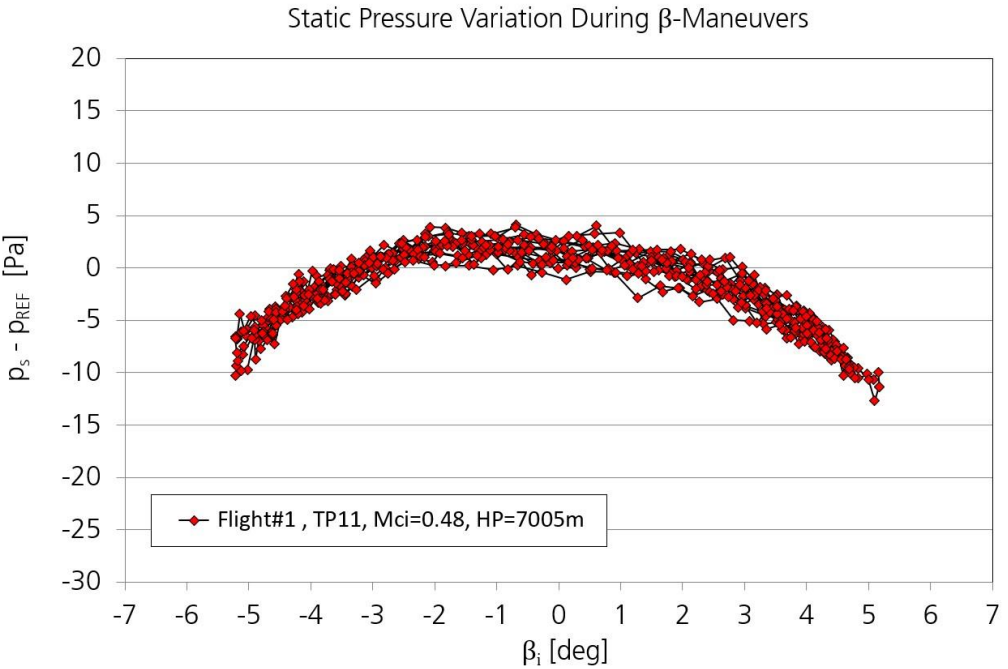

Figure 89*: Dependence of static pressure on β_i. The plot shows 10Hz data from a single test point of the first calibration flight. The data points represent the deviation of the static pressure which has already been corrected for static source error, static beta dependence and altitude changes (according to Equation 15) from the reference pressure measured before/after the actual maneuver.*

Figure 89 shows the result for a single test point of flight #1. Again, the data shows a clear relation between the angle of sideslip and the static pressure during the maneuver. Figure 90 presents the same data for all 8 test points from this flight which were flown with the same flight parameters. Again, the reproducibility of the result for identical flight conditions is excellent.

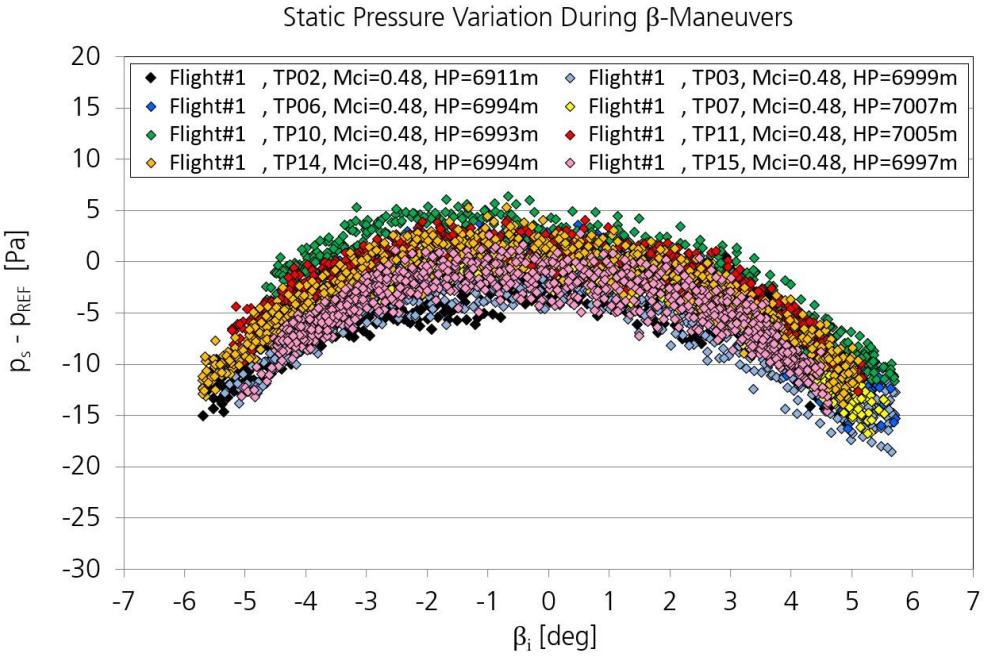

Figure 90*: Dependence of static pressure on β_i. The plot shows the same data as* Figure 89 *but includes all test points on this height level. All test points were flown with the same flight parameters (speed and altitude).*

From the data we can conclude:

- A systematic dependency of the static pressure on β_i can be observed during the yaw oscillations.
- The pressure data again proves the accuracy of the BAHAMAS instrumentation: The noise level (deviation of data from a fit through the curve in Figure 89) is 2.3Pa (2σ value).

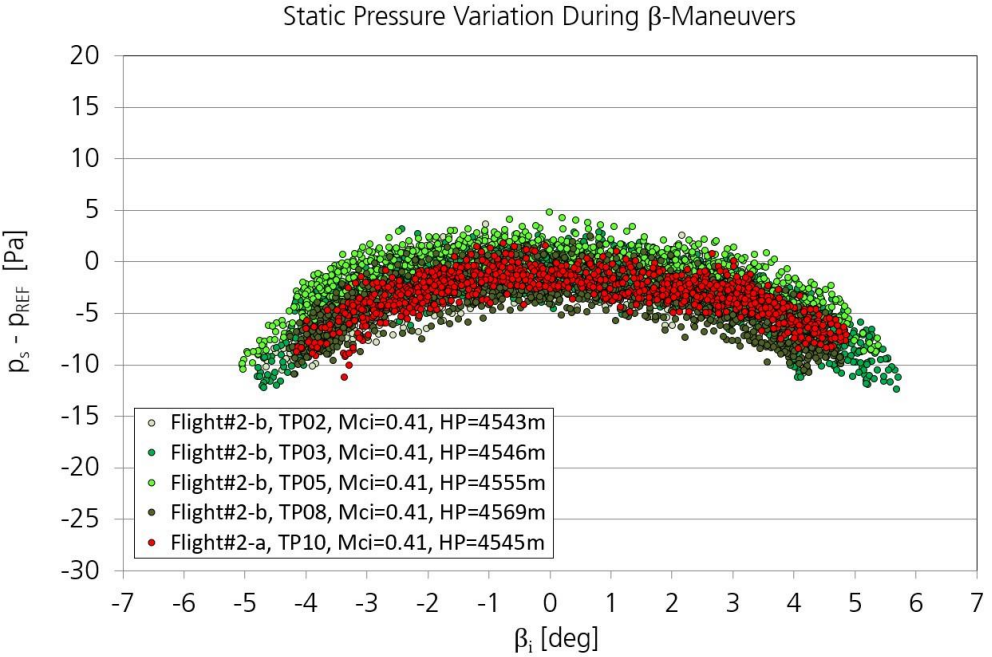

Figure 91*: Dependence of static pressure on β_i for identical test points from different flights*

Figure 91 proves that the results do not change from flight to flight and can be seen as reliable and representative.

And similar to the results from the angle of attack maneuvers we can see from Figure 92 that the relation between $(p_s - p_{REF})$ and β_i depends on flight

conditions. As in case of α we must state that the available data set does not allow to properly parameterize this dependency.
However, since the data range of β_i during regular flight conditions is typically around $\pm 1°$ we can see from Figure 92 that such a parameterization would not add a significant correction of the static pressure measurement. We therefore state that the major contribution from the angle of sideslip pressure correction is given by the result from the static calibration.

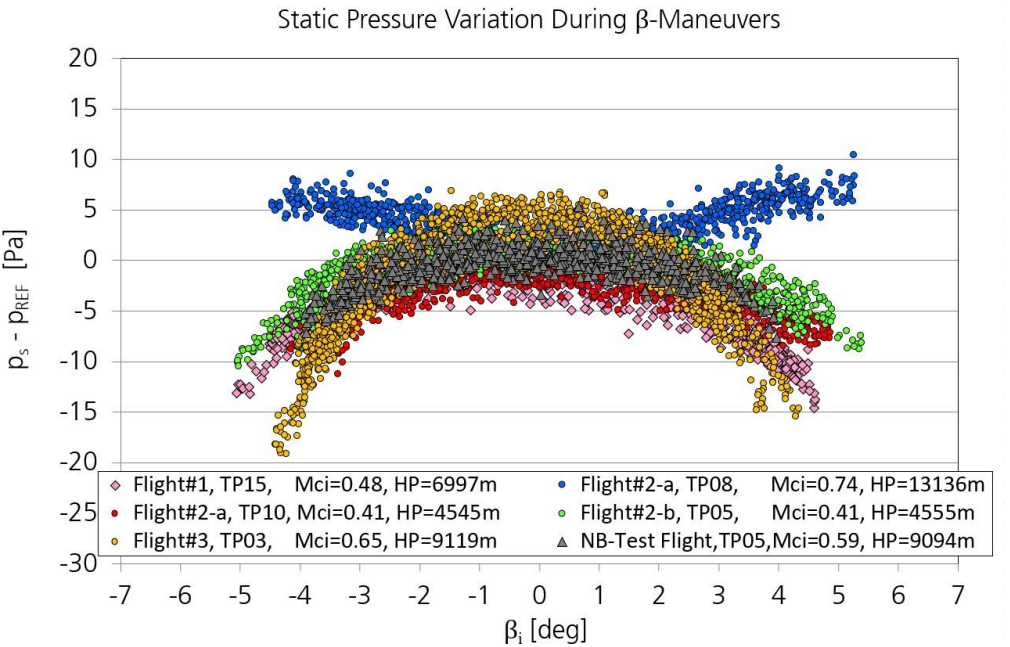

Figure 92*: Dependency of static pressure on β_i for test points flown under different flight conditions and on different days. "NB Test Flight" is data from another experiment performed in February 2019.*

Flight Envelope Coverage

As mentioned above the test points must cover the aircraft flight envelope to allow for a proper and representative parameterization of the correction and to ensure that the results apply to all possible flight conditions.

Figure 93 shows the distribution of the test points for the dynamic flow angle calibration and the static β calibration. The data also contains results from later experiments and proves that the relevant aircraft envelope ($k_\alpha$and k_β are parameterized as a function of the indicated Mach Number M_{Ci}) is covered. Figure 94 shows the relation between indicated and real Mach Number.

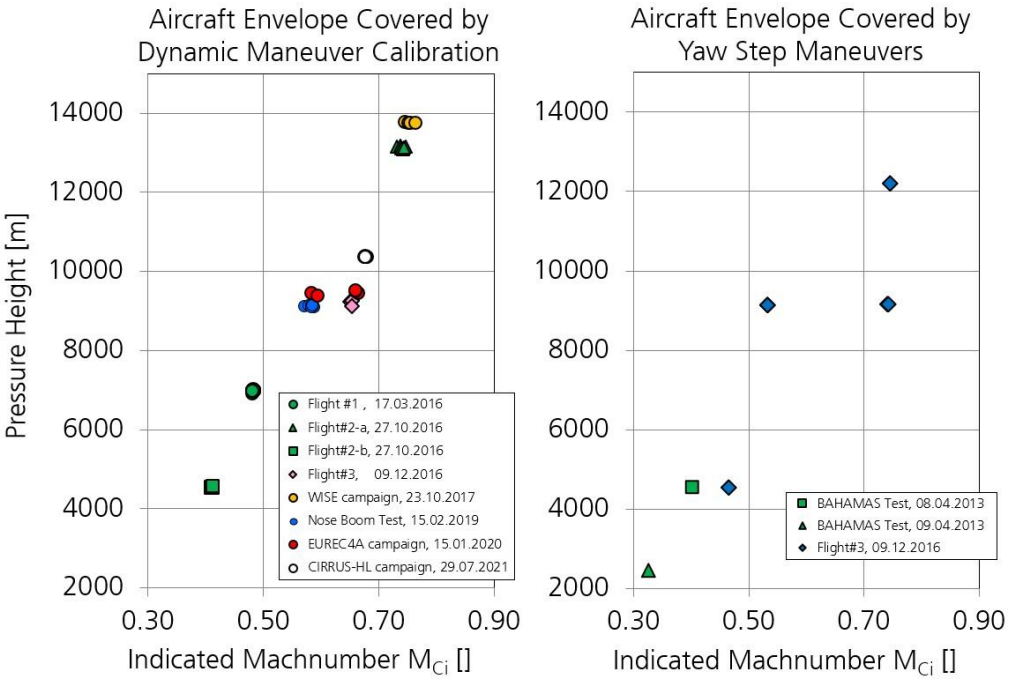

Figure 93*: Aircraft envelope covered by the dynamic inflight flow angle calibration maneuvers and the static β calibration.*

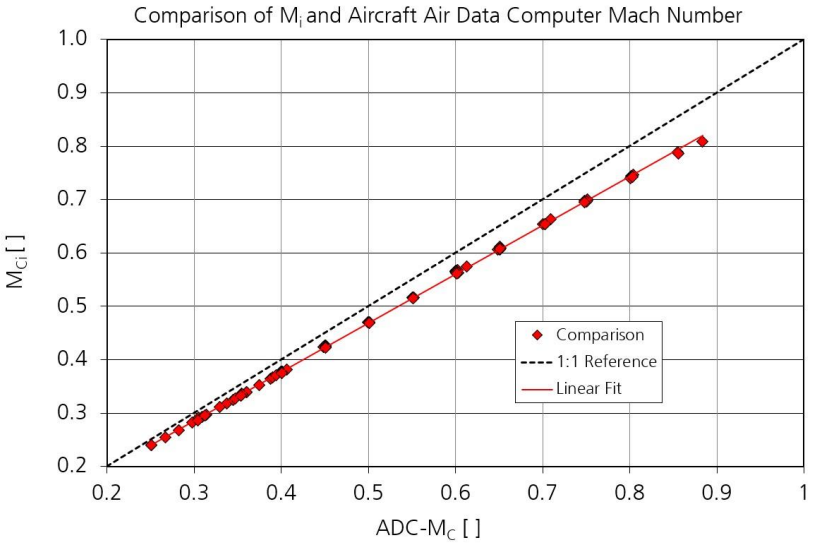

Figure 94*: Relation between indicated Mach Number M_{Ci} and the Mach Number M_C as provided by the aircraft Avionic system.*

Roll Angle Offset

A last calibration concerns the possible angular offset between the inertial reference system and the flow angle sensor with respect to a rotation around the aircraft x-axis (as defined by the IRS). Any installation of the flow angle sensor on HALO includes an adjustment which uses a theodolite but the data processing itself does not include a process to detect a possible misalignment.

The flow angle sensor is basically a cylinder which is fastened at the tip of another cylinder (the nose boom). A possible misalignment between the two x-axes is subject to the "Dynamic Offset Calibration" which has been introduced above. This calibration provides two angles ε_b and η_b which describe the offsets around the aircraft y and z-axes. However, a rotational misalignment around the aircraft x-axis (caused by a rotation of the two cylinders with respect to their common main axis) is not included in the data processing yet.

For simplicity and as long as the correction is small the offset can be handled as an offset in the roll angle data of the IRS. This offset will lead to a wrong

orientation of the "vertical" pressure ports $p_{\alpha 1}$ and $p_{\alpha 2}$ (which are used to determine α_i) as well as of the "horizontal" ports $p_{\beta 1}$ and $p_{\beta 2}$ (for β_i) in Figure 15. Any misalignment must therefore lead to a cross talk between these two pressure measurements i.e. the flow angle sensor would detect a dp_α signal during yaw oscillations which results in a systematic and vertical wind modulation in the data which is non-symmetrical with respect to β.

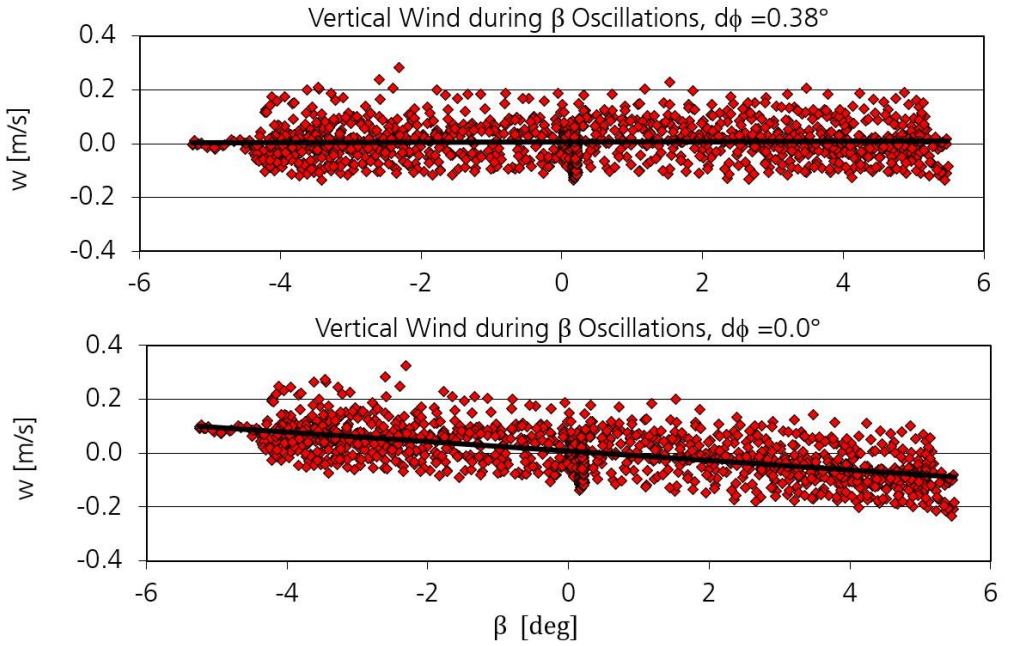

Figure 95*: Determination of the roll angle offset between IRS and flow angle sensor. The lower plot shows the relation between the original vertical wind speed and the angle of sideslip β during a yaw oscillation maneuver. The same data is plotted in the upper graph after an IRS pitch offset angle of 0.38° has been applied to the data. The data belongs to test point TP10 of flight #1.*

Figure 95 shows vertical wind data from a test point of flight #1 during yawing oscillations. The original time series yields a systematic positive offset of vertical wind speed for negative values of β which is visualized by a linear fit into the data.

After the application of an offset of 0.38° in the IRS roll angle data this correlation vanishes and the vertical wind is independent of the angle of sideslip.
The result is identical for other yawing test points. The determination is not subject to a systematic optimization process but determined "by hand". This angular offset must be performed whenever the boom is removed and re-installed on the aircraft.

Effect of correction for non-stationary flight

The dynamic correction of the angle of attack is based on the determination of a typical (trimmed) angle $\alpha_{i,trim}$ which is calculated from the dynamic pressure qc_i. Only deviations from this angle are subject to a correction with k_α. As mentioned above the calculation of $\alpha_{i,trim}$ from qc_i is only defined for trimmed horizontal flight only where the mean values of α_i and $\alpha_{i,trim}$ are found to be close to each other.
However, as one can see from Figure 57 - Figure 60 significant and systematic deviations between these two angles occur during other non-stationary flight states such as:

- Climbs
- Descents
- Changes in aircraft flight state (flaps, air brakes or gear deployment)
- Turns

From the dynamic correction scheme, it becomes immediately clear that a systematic deviation between α_i and $\alpha_{i,trim}$ during these flight states will result in an offset of the corrected vertical wind from the original value.
As we will see in the following the resulting offset works "into the right direction" for these flight conditions. It corrects the original data in a way that it becomes more plausible than before.
However, it must be clear that such an observation is no proof that the correction works and that an $\alpha_{i,trim}$ is defined at all under these conditions.

Further investigations are necessary in order to answer the question how data from the HALO airflow probe must be handled during non-stationary flight conditions.

Climb, Descent and flight states

Figure 96 shows the impact of the dynamic correction on the climb and descent of test flight #1. (The other test flights yield comparable results.)
As one can see the data from takeoff and climb are not significantly changed by the correction. This can be explained by the fact that the difference between α_i and $\alpha_{i,trim}$ is relatively small (compare to Figure 57 - Figure 60) despite the fact that $\alpha_{i,trim}$ was determined on the upper flight level.

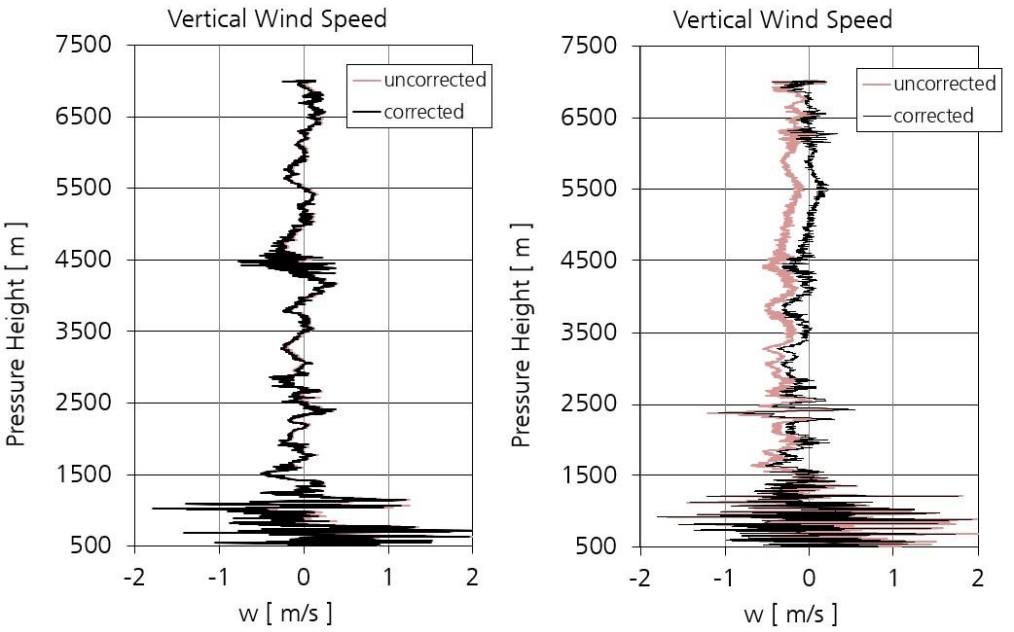

Figure 96*: Effect of dynamic flow angle correction during climb and descent of flight #1. The $\alpha_{i,trim}$ fit was performed on the main flight level (FL230).*

The increased variance of w at low altitude is an atmospheric effect. During this part of the flight the aircraft is within the atmospheric boundary layer where convective effects cause turbulent air motions.

The comparison looks different during descent where air brakes are regularly deployed. According to Figure 96 the uncorrected vertical wind shows a systematic negative offset from the expected mean of $w = 0$ which indicates that the original measurement is erroneous. The application of the correction pushes the data closer to the expected mean value of zero,

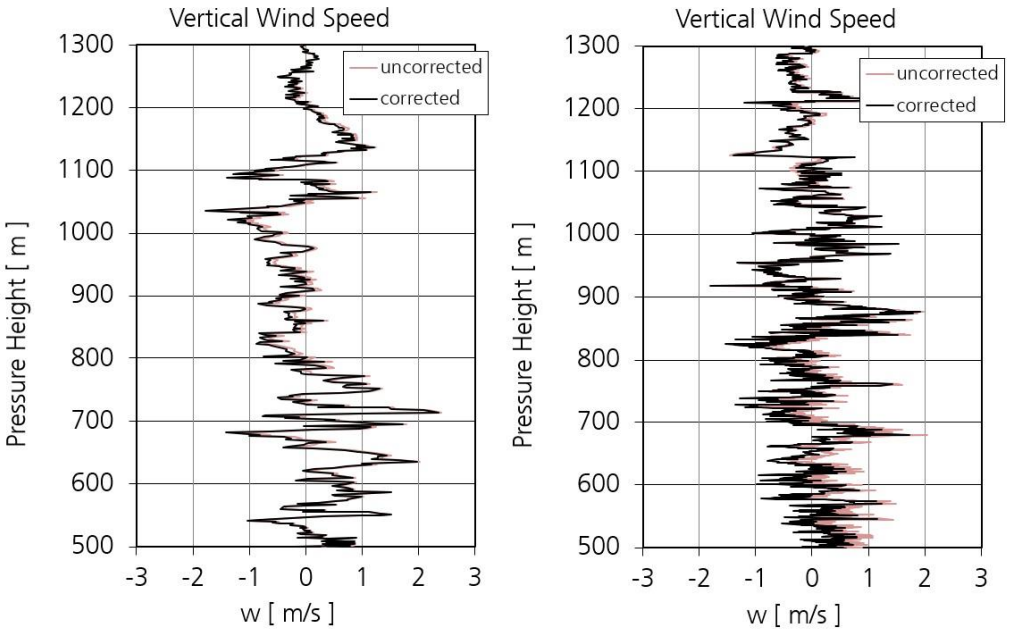

Figure 97*: Effect of dynamic flow angle correction during climb and descent for the lower altitudes of flight #1 (i.e. the lower part of* Figure 96*)*

The lowest flight level of Figure 96 contains the gear and flap operation which lasts longer during the approach. The respective flight part is shown in detail in Figure 97. Despite the fact that the difference between α_i and $\alpha_{i,trim}$ is large the

effect of the correction is surprisingly small which is due to the fact that according to Figure 63 the correction factor $k_\alpha$is small at low speeds.

Turns

Figure 81 above demonstrates the effect of the dynamic correction on horizontal wind data during a long sequence of test flight #1 which includes two 180° turns. The relevant data is shown in more detail in Figure 98 which covers a time interval of more than 20 minutes. The horizontal wind speed is plotted over geographical latitude in order to visualize the horizontal gradient of ws which seems to be stationary during the time interval of the measurement. As one can see the variance of the wind data during the turn is decreased by applying the dynamic correction. The horizontal structure in wind speed is reproduced during the turn with deviations of less than 0.5m/s and no direct correlation can be found between ws and roll angle data.

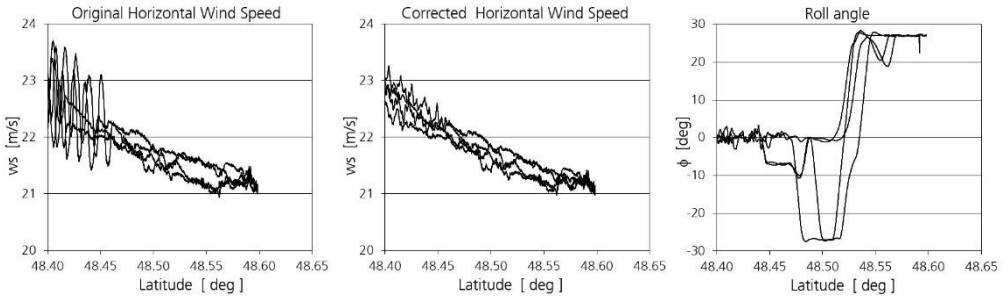

Figure 98*: Effect of dynamic flow angle correction during turns. The plot shows a 20-minute subset of Figure 81 with two 180° turns from flight #1.*

Figure 99 shows another example from test flight #2-a where the correlation between the roll angle ϕ and the vertical wind speed is checked for a pitching – yawing – 180° turn – yawing – pitching sequence.

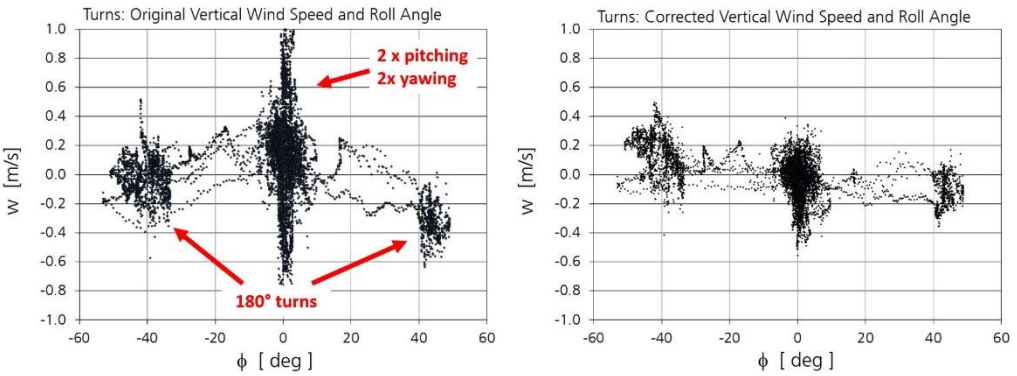

Figure 99*: Effect of dynamic flow angle correction during a series of several pitching and yawing maneuvers including a 180° turn during flight #2-a.*

As demonstrated above the correction eliminates the artificial modulation of vertical wind speed during the pitching maneuvers ($\phi = 0$) itself. But the plot also shows that the dependency of w on the roll angle which is visible in the uncorrected data is reduced by the correction.

The last example concerns a yawing-180°turn-yawing maneuver from Flight #2-a and is shown in Figure 100. Again, the correction removes an obviously artificial correlation between vertical wind speed and the angle of attack during the turn.

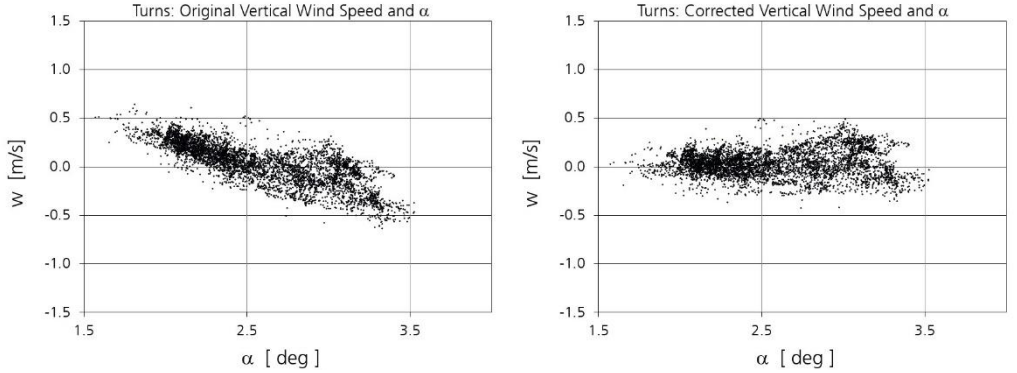

Figure 100*: Effect of dynamic flow angle correction during turns. The plot shows a yawing-180°turn-yawing maneuver from Flight #2-a.*

The data analysis of the test flights did not provide any example where the correction resulted in "worse data" or unexpected correlations between independent data sources. No influence of turns could be found anywhere in the wind data even for large roll angles. Although one can not prove the validity of the dynamic correction scheme for turns we conclude that the correction works and can be applied during turns. The applicability for other maneuvers must be subject to further investigations.

Example of BAHAMAS Wind Data with corrections

In the following we present two examples which prove the capability of the HALO wind measurement system during scientific projects in the field of atmospheric physics. The data shown is always subject to the complete set of aerodynamic corrections as described in this report. While the overview data is processed with a 10Hz time base the spectral analyses shown below use the full resolution of 100Hz in the wind data time series.

EMeRGe Intercomparison 13.07.2017

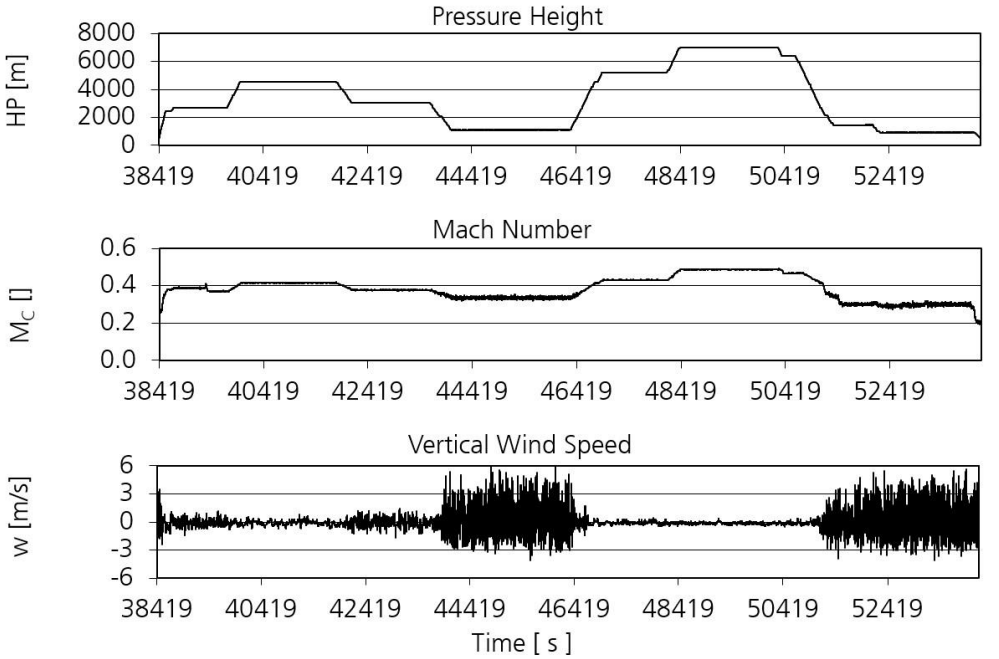

Figure 101*: Overview over the EMeRGe intercomparison flight. The large variations of w mark the flight legs within the atmospheric boundary layer. The data analysis from this report concerns the flight leg at FL37 (44000-46500s).*

The first example is taken from a research flight during the "Effect of Megacities on the transport and transformation of pollutants on the Regional to Global scales" (EMeRGe) campaign.
The flight took place on 13.7.2017 and aimed at the comparison between the scientific instrumentation of two research aircraft: The German HALO and a modified Bae-146-301 of the Facility for Airborne Atmospheric Measurements (FAAM) which is based at the Cranfield University, UK. A detailed description of this flight and data of the comparison can be found in
[18].
Figure 101 gives an overview about the complete research flight. We want to present a spectral analysis from a 30-minute flight section on flight level FL37. As one can see from Figure 101 this part of the flight was well within a convective boundary layer with strong vertical wind fluctuations which is an ideal environment for a spectral analysis of vertical wind data. The flight track of this leg is shown in Figure 102.

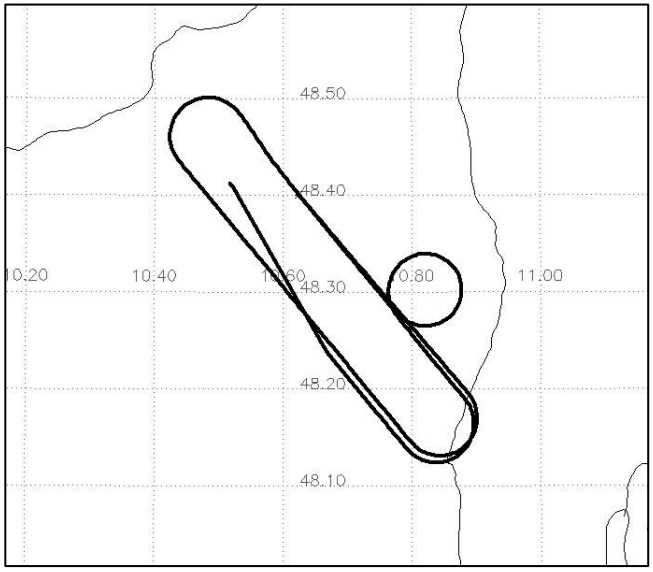

Figure 102*: Flight path of the comparison leg of the EMeRGe research flight which is analyzed in this report.*

As one can see this part of the flight contains three 180° turns and a full circle. The following data analysis uses the complete time series from the flight leg as displayed in Figure 102.

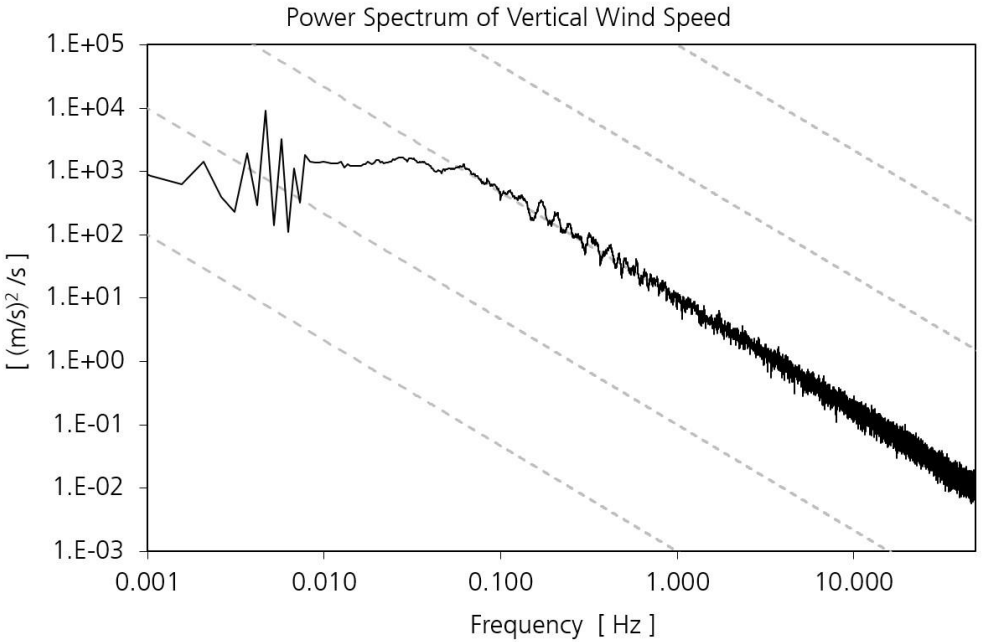

Figure 103*: Power spectrum of vertical wind speed during the flight leg shown in Figure 102. The spectrum was calculated from the 100Hz time series of w which was subject to all aerodynamic corrections described in this report and is smoothed over 30 values. The dashed lines represent the expected -5/3 dependency at high frequencies.*

Figure 103 shows the vertical wind power spectrum as calculated from the 100Hz fully corrected wind data. From the spectrum we can draw the following conclusions:

- The data shows the expected -5/3 behavior over a large portion of the spectrum which proves that:
    - the inertial subrange is well resolved

- no dampening or resonance effect from the instrumentation is visible in the data
- the turns and the full circle in the flight pattern do not lead to unexpected structures in the spectrum

- The -5/3 behavior extends up to the maximum possible frequency of 50Hz in the spectrum
  - the instrument (white) noise level is well below the atmospheric signal
  - the instrumentation (airflow measurement and inertial reference data) is able to resolve the full 100Hz data frequency
  - the boom eigenfrequency is not visible in this example

It is an interesting question how the dynamic correction of w depends on the frequency. In a convective boundary layer and no extreme aircraft maneuvers present one would expect that the deviations of α_i from $\alpha_{i,trim}$ are mostly wind driven. HALO was flying with an indicated Mach Number of $M_{Ci} = 0.32$ which corresponds to an α_i correction factor of $k_\alpha = 1.041$ (according to Figure 63).
For small values of α the vertical wind calculation for straight flight can be approximated by

$$w \approx TAS \cdot \sin(\alpha) \approx TAS \cdot \alpha \sim TAS \cdot \alpha_i \qquad \textbf{Equation 24}$$

Therefore, we expect that the dynamic correction for this flight level results in a vertical wind which is increased by about 4% over a large portion of the spectrum. However, at very low frequencies (30-minute time series!) the changes of α_i cannot be seen as "dynamic" any more, the time series of $1/qc_i$ will follow α_i and no correction takes place.
Figure 104 shows that the spectrum of the wind correction ($w_{corr} - w_{orig}$) behaves mostly as expected. However, some unexpected deviations from the $4\% \cdot w_{orig}$ behavior can be observed in the data.

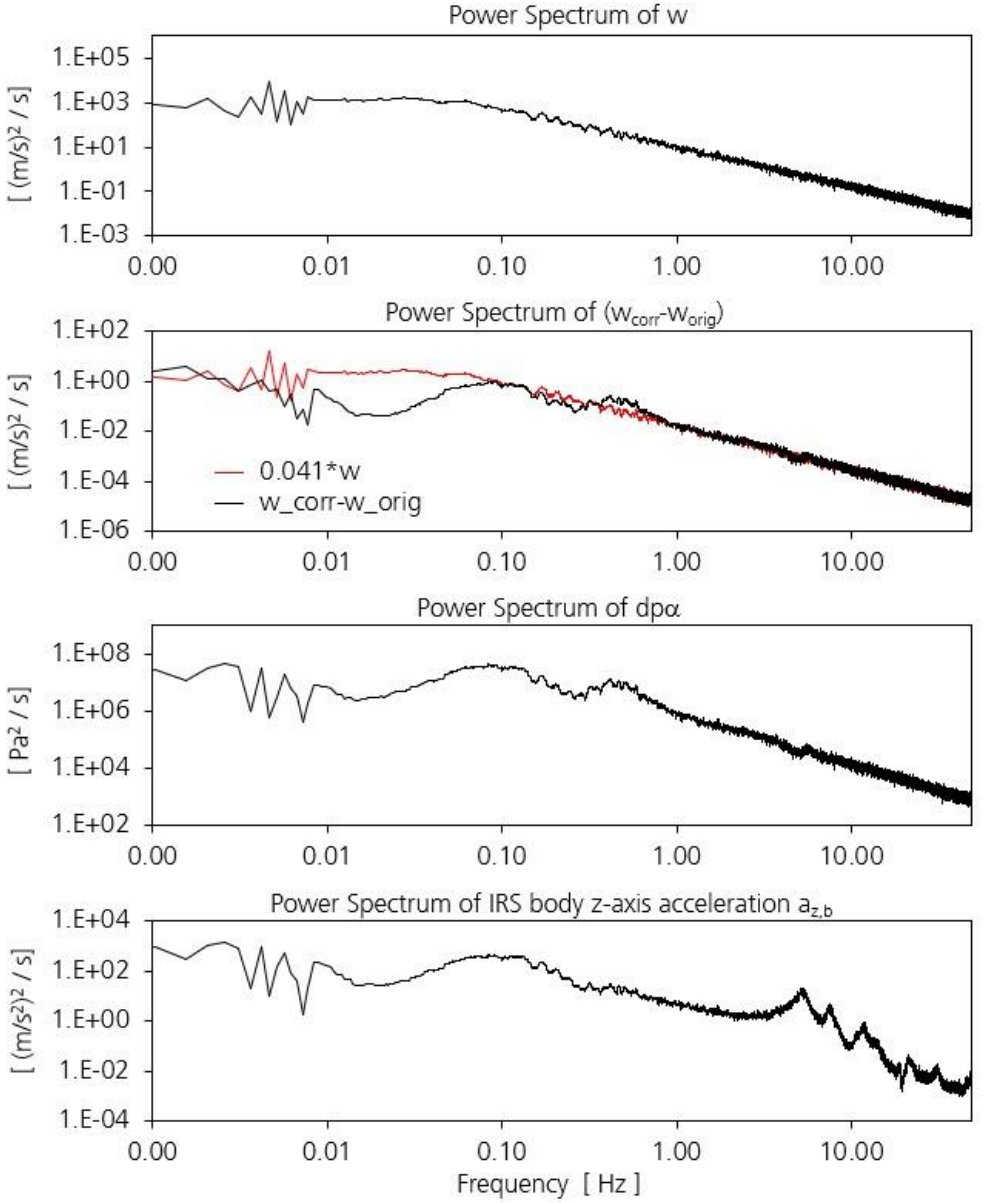

Figure 104*: Spectral analysis of the dynamic correction for the EMeRGe intercomparison flight.*

According to the additional spectra in Figure 104 these structures can be explained by vertical "maneuvers" which are visible in the vertical aircraft accelerations and real structures in the initial α_i measurement (as indicated by the differential pressure dp_α). The plot also proves that the final spectrum of w_{corr} is not influenced by theses contributions. All spectra are based on 100Hz data and are smoothed over 30 values.

EUREC4A Research Flight 05.02.2020

The second example is from the "Elucidating the Role of Clouds-Circulation Coupling in Climate" (EUREC4A) campaign which took place in 2020 on the island of Barbados in the Caribbean [15].

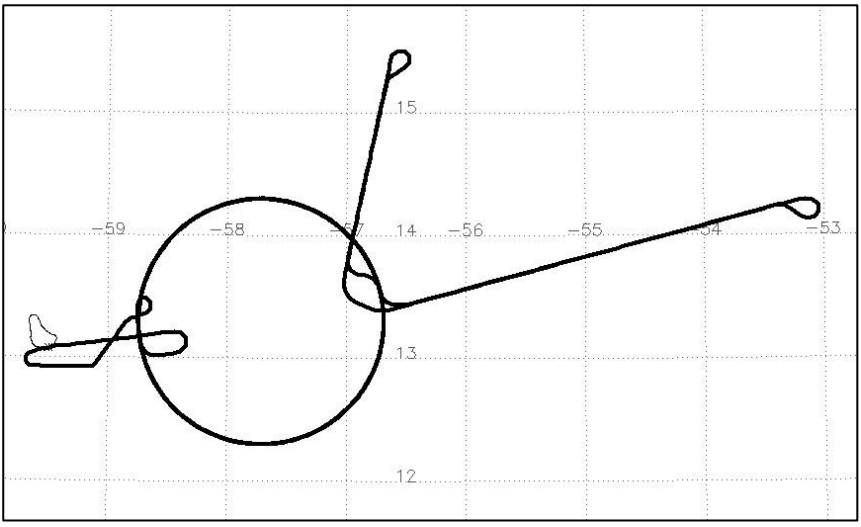

Figure 105*: Flight pattern of the EUREC4A flight from 05.02.2020.*

The long flight (with a duration of more than 9h) took place over water and was performed at a constant altitude of FL325 (9750m). As can be seen from Figure 105 and Figure 106 it consists of a large circle pattern which was flown almost 7

times (2x3.5 circles). The pattern also contains some straight flight legs, multiple turns and several aircraft speed changes in the middle of the flight.
The data set is therefore suitable to

- check for the applicability of a general dynamic correction over a long time period (i.e. determination of a consistent $\alpha_{i,trim}$ for the whole flight)
- investigate the influence of slow and fast turns as well as speed changes on the wind data
- demonstrate the capability of the system to measure fast fluctuations at higher altitude and speed (signal to noise check)

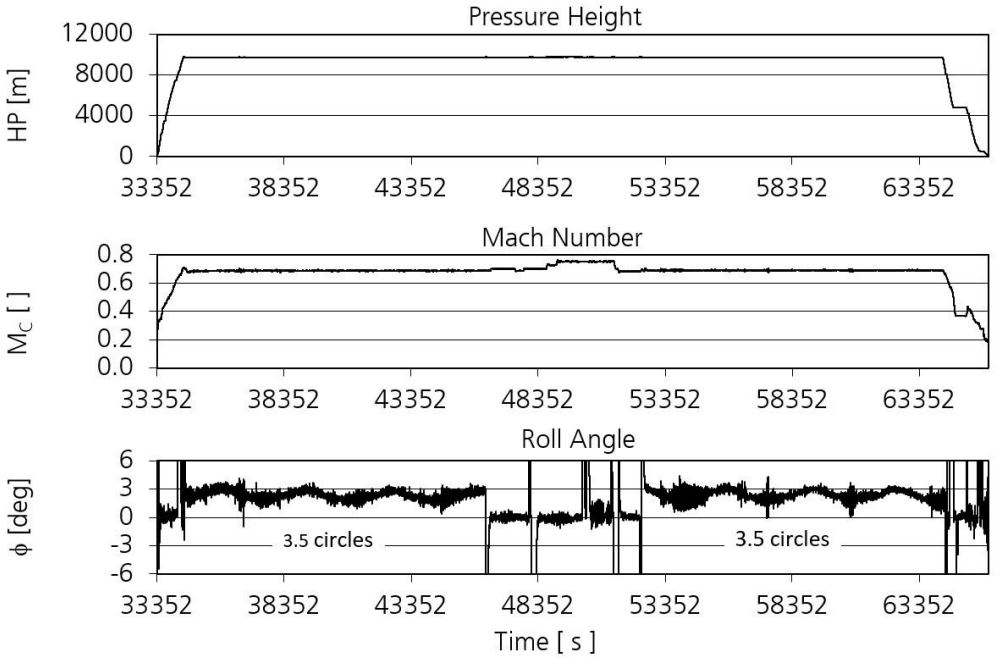

Figure 106*: Overview data for the complete EUREC4A research flight from 05.02.2020.*

The calculated $\alpha_{i,trim}$ and its comparison to α_i is shown in Figure 107. As one can see the idea of a linear time dependence for α_i works very well and the parameterization found can be used throughout the whole flight.

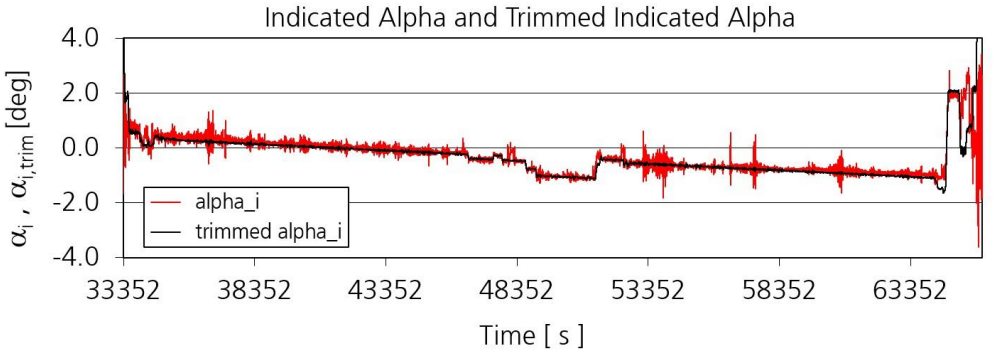

Figure 107*: Comparison of $\alpha_{i,trim}$ and α_i for the EURECA research flight with a duration of more than 9h.*

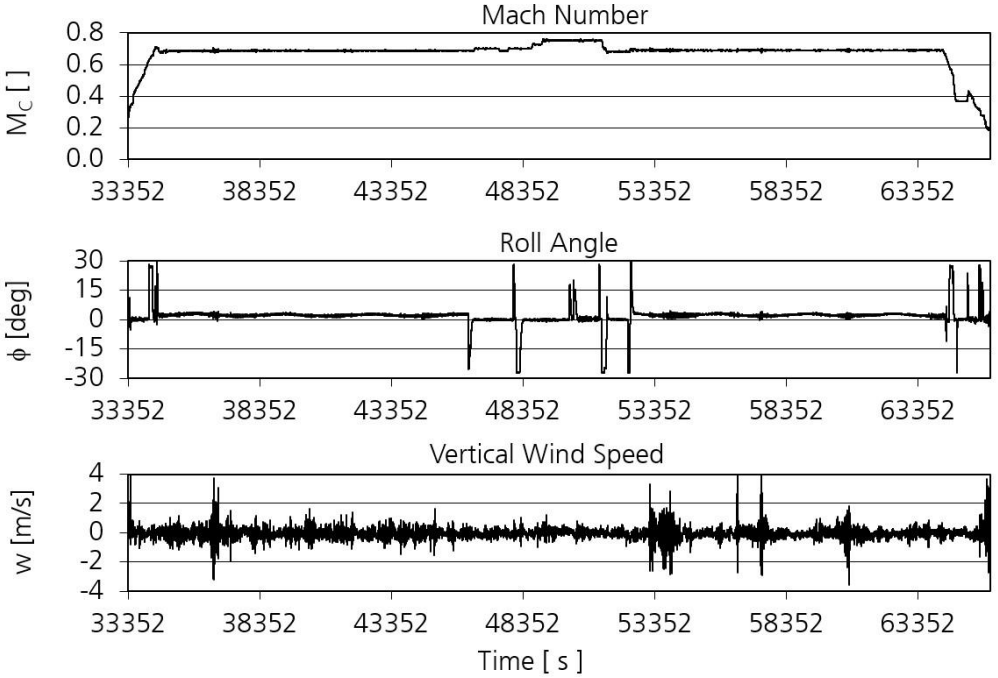

Figure 108*: Vertical wind data from the EUREC4A research flight. The vertical wind data has a 10Hz time resolution and was subject to the full correction scheme described in this report.*

Figure 108 shows the complete time series of the corrected vertical wind from this flight. The data shown was calculated at a stretch over the complete flight and proves the high data quality of the different sensors. The mean of w for the whole flight is $\overline{w} = 0.043\ m/s$ and the standard deviation was found to be $\sigma_w = 0.25\ m/s$. No trend is visible in the vertical wind data over the complete flight and no correlation can be detected between w and the aircraft roll angle or speed.

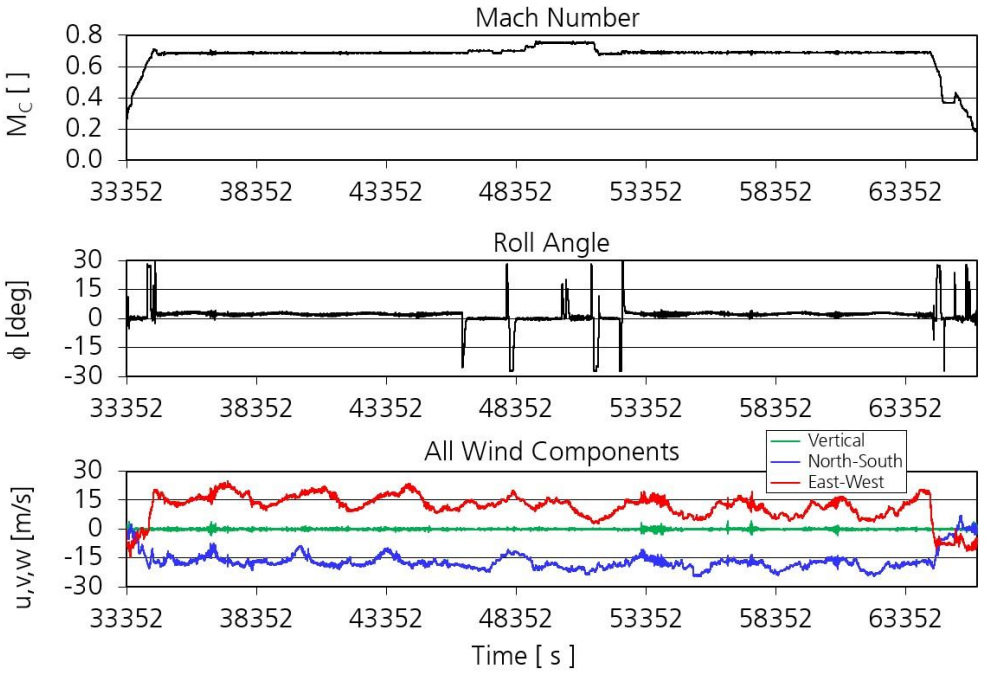

Figure 109*: All wind components from the EUREC4A research flight. The wind data has a 10Hz time resolution and was subject to the full correction scheme described in the report.*

The horizontal wind speed data can be seen in Figure 109. In this case a periodic modulation of the wind data is visible which has the same frequency as the large circles in the flight pattern.

A plot of wind speed over geographical latitude which is shown in Figure 110 explains the effect. The large circles were flown in a region with a horizontal gradient in wind speed which leads to a periodic modulation of the measured wind speed during the maneuver. The data from the straight flight leg which was flown between the circles proves this observation and is in perfect agreement with the data measured on the circles.

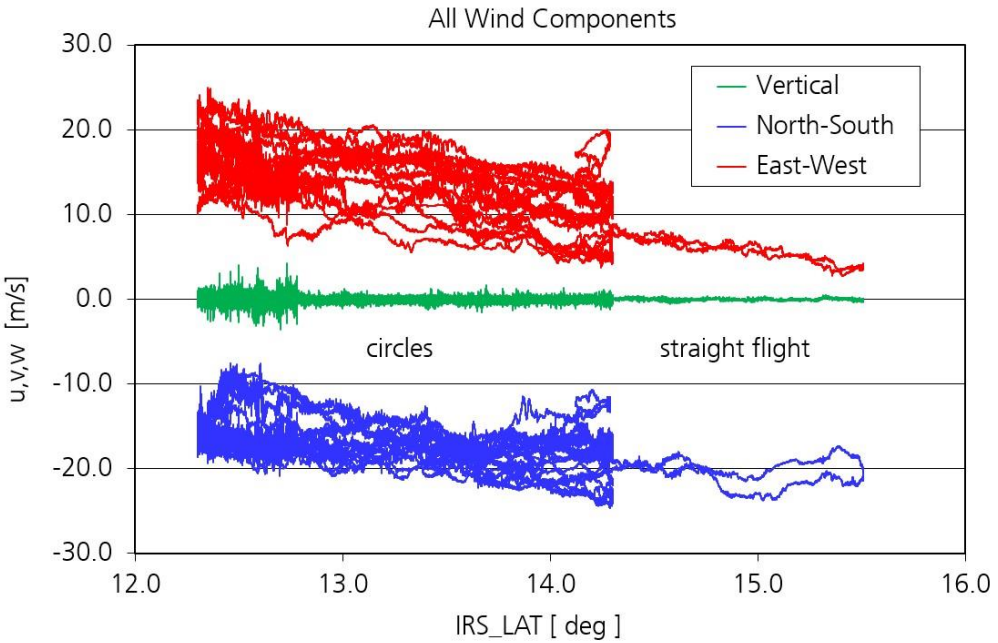

Figure 110*: Different wind components on FL325 from the EUREC4A research flight plotted over geographical latitude. The data shows a horizontal gradient which is seen in the circular flight pattern as well as in straight flight.*

From these observations we can conclude that the measurement of horizontal wind speed is also not influenced by aircraft turns, speed changes or constant roll angles.

It is an interesting question how the HALO wind measurement performs at higher altitudes and Mach Numbers where atmospheric variance is smaller and the effect of the correction larger (compare to Figure 63) than during the boundary layer flight leg of the first example.

As one can see from the vertical wind speed in Figure 108 the atmosphere during the EUREC4A flight was not homogeneous but shows areas with large values of *w* and others with very little variability. Therefore, we cannot determine a single representative spectrum of w for this flight but have to select a subset where the air data indicates homogeneous atmospheric conditions.

Figure 111 shows the power spectrum of vertical wind speed for a respective flight leg of about 5 minutes length.

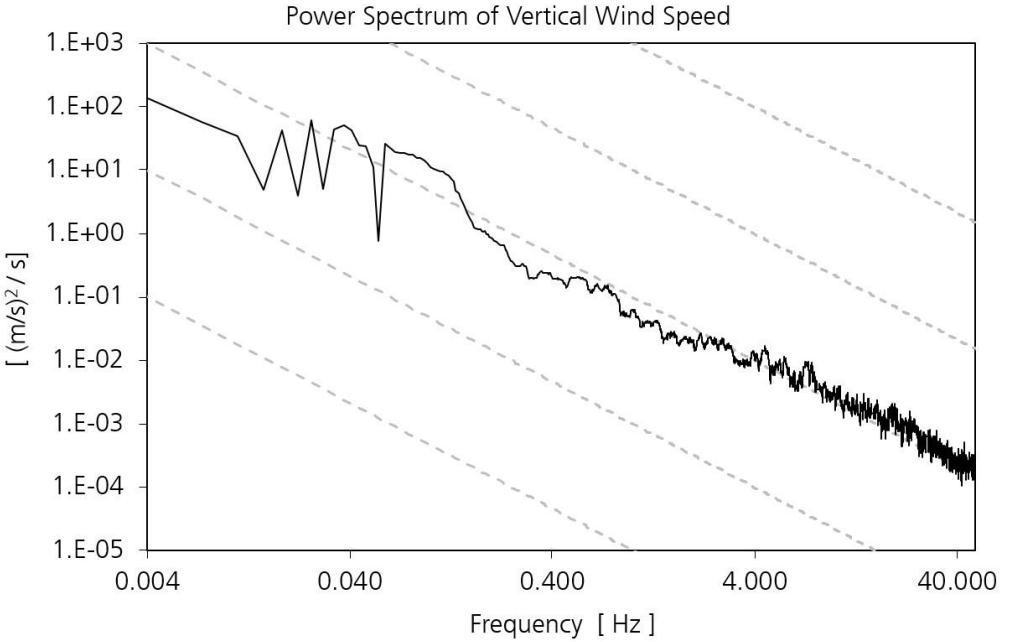

Figure 111*: Power spectrum of vertical wind speed from the EUREC4A test flight of 05.02.2020. The spectrum is calculated from 100Hz data over a time interval of about 5 minutes and smoothed over 30 values. The dashed lines represent the expected -5/3 dependency at high frequencies.*

From the spectrum one can see that the vertical wind data follows the expected $-5/3$ behaviour at high frequencies and that no white noise effect is visible in the data. We can therefore conclude that the flow angle corrections do not change the spectral properties of w even at high altitude and large Mach Numbers.
A last check concerns the vertical profiles of w during this flight which are shown in Figure 112. The plot proves that the mean vertical wind measurement during ascent and is close to zero ($\overline{w} = 0.024\ m/s$ (ascent), $\overline{w} = -0.021\ m/s$ (descent)) and that the observed variability lies within the expected range ($\sigma_w = 0.33\ m/s$ (ascent), $\sigma_w = 0.35\ m/s$ (descent)).

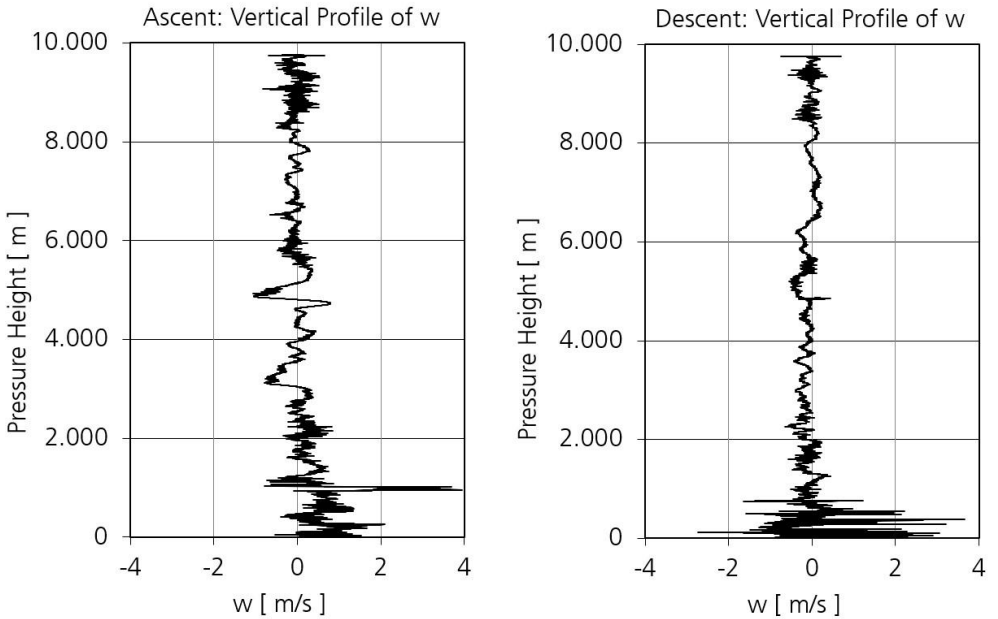

Figure 112*: Vertical profiles of corrected vertical wind speed for the EUREC4A research flight of 05.02.2020.*

However, especially at lower altitudes where gear and flaps are deployed the data shows some larger structures with systematic deviations from the expected mean values.

Discussion

The flow angle calibration of the HALO nose boom mounted 5-hole probe resulted in correction schemes for the aircraft pressure measurement as well as for the local flow angles which are measured directly by the airflow sensor. The relative orientation of the airflow sensor to the inertial reference unit is a third important information which can be derived from the data of these flight tests. All calibrations are based on the determination of the 3-dimensional wind vector and assumptions about certain wind properties.

Due to the negligible mean value and the small fluctuations vertical wind is much more sensible to measurement errors and drift effects from the air data probe or the IRS. However, inflight calibration procedures help to detect and correct for most of these effects. Measurement errors of the horizontal wind measurements are usually more difficult to detect and the relative uncertainty is much smaller.
For an aircraft with an up to date instrumentation no timing corrections (delays) between the different data sources have to be considered any more. Post processing of IRS data reduces the instrument error in a way that almost the complete wind speed error is caused by the air data probe.
Under stable horizontal flight conditions, the two flow angles α and β usually show a stable mean value (0 for β and θ for α) with high frequency fluctuations around these values which can be attributed to atmospheric wind variability. Therefore, the airflow sensor can also be seen as an exclusive detector for high frequency wind fluctuations as long as flight conditions are stable. Inflight maneuvers can be used to deviate from these conditions by generating different mean flow angles.

All pressure and flow angle corrections show a static and a dynamic component. In general, the static corrections account for most of the measurement errors in pressure and flow angles. Therefore, the static calibration is supposed to be sufficient for classic aircraft flight test applications.

However, atmospheric science which deals with dynamic wind effects has extreme accuracy requirements. In this case the dynamic calibration cannot be neglected.

The dynamic calibration/correction is an established tool to improve airborne wind measurements. However, the correction scheme presented in this document is new. The concept of applying the correction only to the dynamic part of the respective flow angle i.e. to the deviation from its "typical" value under the respective flight conditions is consistent and can be applied to α and β the same way.
The method covers the complete aircraft envelope and proves to be robust and stable. The results are very tolerant with respect to the way the maneuvers are flown, amplitudes and frequency of the maneuver oscillations do not show a significant impact on the correction factors k_α and k_β.
The dynamic calibration proves that the wind driven fluctuations are not properly measured if only static calibration is applied to the flow angle measurements. Without appropriate corrections:

- the vertical wind variations are systematically underestimated
- the horizontal wind variations are overestimated (except at high Mach Numbers)

The dynamic error correction is larger for the angle of attack than for the angle of sideslip.
In general, one can state that the airflow measurements are getting more difficult at high altitude and increasing aircraft speed. One reason comes from the fact that some of the aerodynamic corrections (static source error and k_α) are maximum close to the boundary of the aircraft envelope. Another problem is that flight test under these conditions is very challenging. A proper yaw or pitch maneuver is much more difficult to fly if the aircraft is operated close to its speed and altitude limits. Therefore, many maneuvers result in a loss of speed or altitude or large variations in oscillation amplitude or frequency. As a consequence, the k_α and k_β values typically show more scatter in this part of the envelope than at lower altitude.

For normal flight conditions and low atmospheric turbulence, the correction does not significantly change the calculated wind since

- only the small fluctuations around a mean flow angle are corrected
- the correction is in the order of 5-15%of this difference only
- the correction only concerns fast fluctuations of the flow angles

The correction does not leave a footprint or unexpected features in the wind spectra.

The final accuracies in the flow angle measurements are given for the most part by the static calibrations and were found to be:

- 0.15° for the angle of attack (2σ)
- 0.22° for the angle of sideslip (2σ)

In case of static pressure, we similarly find that the dynamic contributions are significantly smaller than the corrections which were determined from the static calibration. The accuracy of the flow angle pressure correction was found to be:

- 0.08 hPa (2σ) for the angle of sideslip

The influence of α_i and the respective error are already contained in the results from the preceding trailing cone parameterization [5].

Almost all aerodynamic corrections presented in this report were parameterized as functions of indicated units which greatly simplifies the data processing of aircraft data. An overview about the different corrections is given in Table 10.

We must emphasize that the presented results are valid for this specific aircraft and its individual instrumentation only. It is not clear to which extend these results can be applied to other aircraft.

air data parameter	type of correction	parameterization parameter	requires processed parameters?
static and dynamic pressure (p_s, qc)	static source error (SSE) correction	$M_{Ci}(p_{s\,i}, qc_i)$	no
	SSE ps-correction	p_{si}, $M_{Ci}(p_{si}, qc_i)$	no
	Also possible with different parameterization:		
	static α-correction	α_i	no
	static β-correction	β_i	no
	dynamic α-correction	$\alpha_i, \alpha_{i,trim}(qc_i)$	no
	dynamic β-correction	β_i	no
angle of attack (α)	basic static calibration	α_i, θ from Trailing Cone flight	no
	inflight static calibration	α_i, θ	no
	or		
	offset from IRS:ε_b	$w, TAS, \alpha, \beta, \theta, \phi$	yes
	dynamic calibration	$k_\alpha(M_{Ci}), \alpha_i, \alpha_{i,trim}(qc_i)$	no
angle of sideslip (β)	static calibration	β_i	no
	offset from IRS: η_b	$w, TAS, \alpha, \beta, \theta, \phi$	yes
	dynamic calibration	$k_\beta(M_{Ci}), \beta_i$	no
Roll angle (ϕ)	offset from sensor: $d\phi$	w, β	yes

Table 10: ***Required corrections for airflow sensor data as demonstrated in this report***

As a summary we can state that HALO is capable of acquiring high quality 3-dim wind data of up to 100Hz during straight and leveled flight. All results indicate that the measurement of wind speed during turns is of comparable quality. However, the wind vector measurement during aircraft ascent and descent is questionable and must be subject to further investigations.

Summary

Based on the results from the static source error calibration [5] we have presented a complete calibration concept for the nose boom mounted air data probe of the German research aircraft HALO.

The calibration contains new techniques which are presented for the first time and covers the following aspects:

- Calibration of the airflow angles
- Determination of their impact on the pressure measurement
- Identification of the exact orientation of the air data probe with respect to the aircraft axes

The presented methods are based on the exact determination of the 3-dimensional wind vector and require a precision Inertial Reference System (IRS) on the aircraft. The quality of this system (accuracy, timing) is critical for the calibration. Assumptions about certain wind properties allow then to determine corrections for the indicated data of the aircraft air data sensor. In many cases the parameterization of these corrections is based on directly measured (indicated) units in order to simplify the data processing.
The correction of the airflow data always consists of a "static" and a "dynamic" contribution which apply to the mean units and their fast fluctuations around a "typical" value at the actual aircraft flight state. In case of the angle of attack this dynamic correction refers to a reference value which can be calculated from indicated dynamic pressure and a time trend which accounts for the aircraft weight loss during flight. Harmonic pitch and yaw oscillation maneuvers were used to investigate these effects. In general, the dynamic corrections for flow angles and air pressure are significantly smaller than the static ones. However, they play an essential role for precise and fast wind measurements in atmospheric research.

The experiment proves that measurements which are based on static calibration methods only underestimate the vertical wind fluctuations while slightly overestimating the variability of horizontal wind.
The report also shows additional data from other experiments and covers different aircraft configurations as well as most of the aircraft envelope.

Acknowledgement

The flight test and the research experiment were positively evaluated by the HALO steering committee and funded by the HALO consortium whose decision is very appreciated by the authors.
The authors express their appreciation to all campaign members and partners involved in the WISE (carried out 2017), EMeRGe (European part carried out 2017), EUREC4A (carried out 2020) and CIRRUS-HL (carried out 2021) campaign, without whom this investigation would not have been possible. In particular we would like to thank the scientific campaign coordination teams and principal investigators (PI) Martin Riese (IEK-7, Jülich Research Centre), Martin Kaufmann (IEK-7, Jülich Research Centre), Peter Hoor (Institute for Atmospheric Physics, University of Mainz) and Daniel Kunkel (Institute for Atmospheric Physics, University of Mainz) of the WISE campaign, John P. Burrows and Maria Dolores Andrés Hernández (Institute of Environmental Physics, University of Bremen) of the EMeRGe campaign, Bjorn Stevens and Lutz Hirsch (Max Planck Institute for Meteorology, Hamburg) of the EUREC4A campaign and Christiane Voigt (German Aerospace Center, Institute of Atmospheric Physics, Oberpfaffenhofen & Johannes Gutenberg University Mainz) of the CIRRUS-HL campaign. The campaigns were supported by the German Research Foundation (DFG) within the Priority Program SPP 1294 "Atmospheric and Earth System Research with HALO", the Helmholtz Association and a wide range of other institutional partners that made measurements with HALO possible.
We thank all colleagues involved in this project. Special thanks go to Christoph Grad and Florian Gebhardt for their support in the operation, maintenance and calibration of BAHAMAS as well as for the pressure sensor development.
We thank the DLR pilots and operations team for their support in the realization of the ambitious flight test plans and Part 145 staff for keeping HALO always "ready to fly". Especially Steffen Gemsa provided important inputs and discussions during the design of the flight test and the proper performance of the first flight trials.

There is nothing good to say about the Corona Pandemic (COVID-19), but the suspension of some large measurement campaigns in 2020 and 2021 is one of the reasons that this report could be written. We therefore want to commemorate the victims of this terrible disease and express our hope for a return to a (research) life which is at least similar to the one we were used to before.

References

[1] W.Bögel and R.Baumann, *Test and Calibration of the DLR Falcon Wind Measuring System by Maneuvers*, J. Atmos. Ocean Tech. 8, 5-18, 1991

[2] Cramer, M., *Performance of IGI AEROcontrol-IId GPS/inertial system.* Final report, Available from: University of Stuttgart, Institute for Photogrammetry, 2001, D-70174 Stuttgart, Geschwister-Scholl-Str. 24 D, (https://www.ifp.uni-stuttgart.de/en/publications/annual_publications/)

[3] *Flugmechanik*, LN9300, Blatt 1 Normenstelle Luftfahrt, DK 533.6:003.62:001.4:629.73, Dezember 1970

[4] *RUSKA 7750i Air Data Test Set, User's Manual*, Fluke Cooperation, November 2010, Fluke Corporation, P.O. Box 9090, Everett, WA 98206-9090, U.S.A (https://eu.flukecal.com/de/literature/product-manuals/ruska-7750i-air-data-test-set-users-manual)

[5] Andreas Giez, Martin Zöger, Volker Dreiling, Christian Mallaun, *Static Source Error Calibration of Nose Boom Mounted Air Data System on an Atmospheric Research Aircraft Using the Trailing Cone Method.* DLR-Forschungsbericht 2019-7, 2020, ISRN DLR-FB—2019-07 https://elib.dlr.de/135789/

[6] Goodrich. (1975). *Total Temperature Sensors.* Technical Report 5755, Revision C, 1994, Goodrich Sensor Systems, Goodrich Cooperation, Burnsville, MN, 1976

[7] Gracey, W., *Measurement of Aircraft Speed and Altitude.* NASA Reference Publication 1046, 1979, National Aeronautics and Astronautics Administration, NASA, Dryden Flight Research Center, Edwards, California (https://ntrs.nasa.gov/archive/nasa/casi.ntrs.nasa.gov/19800015804.pdf) or via SpaceAge Control, Inc, 38850 20th Street East Palmdale, CA 93550 USA

[8] Haering Jr., E. A., *Airdata Measurement and Calibration.* NASA Technical Memorandum, 1995, National Aeronautics and Astronautics Administration, NASA, Dryden Flight Research Center, Edwards, California (https://www.nasa.gov/centers/dryden/pdf/88377main_H-2044.pdf) or via SpaceAge Control, Inc, 38850 20th Street East Palmdale, CA 93550 USA

[9] Krautstrunk, M. and Giez, A., *The Transition from FALCON to HALO Era Airborne Atmospheric Research*, in Atmospheric Physics - Background - Methods - Trends, U. Schumann, Editor, Springer-Verlag Berlin Heidelberg, 2012, p. 609-624, doi: 10.1007/978-3-642-30183-4_37.

[10] Lenschow, D. H. and Spyers-Duran, P.: *Measurement Techniques: air motion sensing*, RAF Bulletin 23, NCAR - RAF, NCAR Research Aviation Facility, https://opensky.ucar.edu/islandora/object/archives%3A6961, description of air measurement processes at NCAR, 1989.

[11] Mallaun, C., A. Giez, and R. Baumann, *Calibration of 3-d wind measurements on a single-engine research aircraft*, Atmospheric Measurement Techniques, 8 (8), 3177-3196, 2015

[12] Romy Heller, Christiane Voigt, Stuart Beaton, Andreas Dörnbrack, Andreas Giez, Stefan Kaufmann, Christian Mallaun, Hans Schlager, Johannes Wagner, Kate Young, Markus Rapp, *Mountain waves modulate the water vapor distribution in the UTLS*, Atmos. Chem. Phys., 17, 14853–14869, 2017

[13] Rosemount. (1975). *Model 858 Flow Angle Sensors.* Technical Report Bulletin 1014, Revised 11/94, Rosemount Engineering, Minneapolis, MN, 1976

[14] Rosemount. (1976). *Aerodynamic Performance of Rosemount Model 858 Air Data Sensor.* Rosemount Report 8767, Richard V.De Leo, Floyd W. Hagen, Aeronautical Research Department, Rosemount Inc., Minneapolis, MN, 1976

[15] Bjorn Stevens et al., *EUREC4A,* MS No.: essd-2021-18, Special Issue: *Elucidating the role of clouds–circulation coupling in climate: datasets from the 2020 (EUREC4A) field campaign*

[16] Stull, R.B. (1988) *An Introduction to Boundary Layer Meteorology*. Kluwer Academic Publishers, Boston. ISBN 978-94-009-3027-8

[17] USAF Test Pilot School, *Pitot Statics and the Standard Atmosphere*, Document ADA320216, 1996, available from SpaceAge Control, Inc, 38850 20th Street East Palmdale, CA 93550 USA

[18] Schumann, U., 2020 (Editor): *Measurement and model data comparisons for the HALO-FAAM formation flight during EMeRGe on 17 July 2017. DLR Forschungsbericht*, DLR-FB-2020-48, 188 pp, ISRN DLR-FB—2019-07 (2020), doi.:10.5281/zenodo.4427965 (https://zenodo.org/record/4427965)

Appendix A

Investigation about the precision of angle of attack and vertical wind measurements from the BAHAMAS system

Andreas Giez, 17.04.2025

The Appendix investigates the impact of nose boom vibration on the HALO wind measurement and uses the respective signal to determine the system precision for vertical wind data. It refers to the report about measurement errors of HALO air data [A1]. This report introduces the terms "accuracy" and "precision", describes the error propagation method and determines the measurement errors of HALO for different flight scenarios.

Introduction

Error propagation calculation determines the accuracy of a measured unit i.e. the validity of its absolute (mean) value. However, in many cases it is possible to analyze the temporal behavior of a physical unit beyond this limit. The fact that the measured variability of a unit is smaller than the accuracy does not automatically mean that the observed signal is "wrong" or "not real". It just means that the uncertainty in the absolute value is in the same order of magnitude as the fluctuation of the observed data. If the observation system is stable and does not generate significant instrumental noise or drift effects the measurement data still contains useful information beyond the calibration limit. Therefore, it can be used to realistically describe the fine structure in the temporal behavior of a unit or to determine secondary data which only depends on the variability of the unit. However, the fundamental requirement for respective investigations is an instrumentation and a data system with excellent measurement precision which allows to exactly resolve these fluctuations. In other words: The precision of the data acquisition system must be significantly better than the accuracy of the

concerned unit and the variability of the real (atmospheric) signal under investigation. In this case the sensor yields realistic fluctuations around the (inaccurate) mean value. The precision of a measurement system quantifies the theoretical accuracy which could be achieved if all sensors and aerodynamic parameterizations which are used in the data processing were subject to a perfect calibration with no error. It is of great interest to determine this precision in order to understand whether observed data fluctuations represent real atmospheric signals or just random noise contributions from an electronic component in the measurement chain.
One mean to perform this analysis is spectral analysis, which can help to identify the onset of white noise at a certain signal level or data frequency. The presence of a clear "-5/3 dependency" in the power spectrum of air data at high frequencies in a turbulent environment is a reliable indicator which can be used to estimate the precision for this kind of measurement.

However, there is in general no defined ("known") atmospheric reference signal for any of the parameters from an airborne air data measurement which can be used to verify that observed data is real. Some of the inflight calibration methods described in the HALO report on the calibration of the airflow sensor [A2] use aircraft maneuvers to artificially generate such reference signals which are then tracked and analyzed in the data processing. However, maneuver-induced inputs are usually "slow" and have large amplitudes.
One exception from the statement about missing "natural" inflight reference data is the angle of attack measurement with a nose boom mounted air data sensor because nose boom vibration creates a very small but characteristic footprint in the flow angle data. In principle, this signal can be detected by a fast air flow sensor with sufficient precision during flight.

HALO Nose Boom Vibrational Behavior

Nose boom design always aims at the minimization of boom vibration during flight in order to avoid aeroelastic resonance effects and to reduce artificial data modulation in the flow sensor measurement. However, every mechanical structure shows an intrinsic vibrational behavior with characteristic frequencies ("Eigenfrequencies"). These frequencies are a function of material properties, weight distribution and geometry of the specific structure. Therefore, Eigenfrequencies are like a fingerprint for any mechanical object including the complete aircraft structure itself.

The vibrational behavior of any structural component on an aircraft contributes to the overall aeroelastic behavior of the complete platform. Certification of new aircraft as well as certification of (external) modifications to existing aircraft require an extensive and costly investigation to prevent that Eigenfrequencies from different components match each other. Such a match of Eigenfrequencies leads to mechanical resonance effects. Aerodynamic excitation of critical vibration modes can result in a complete disassembly of structural components during flight with potentially catastrophic effects. Therefore, any mechanical structure on an aircraft is subject to a detailed vibrational investigation (which typically includes testing) in order to fully characterize and understand their role in the overall vibrational behavior of the aircraft during flight.

The vibrational behavior of the HALO nose boom was subject to multiple investigations in the engineering process of the aircraft as well as later in the production, certification and during the introduction phase at DLR. It is important to note that the Eigenfrequency of the nose boom is always influenced by the weight of the payload on the instrument tray behind the 5-hole probe: the lowest frequencies are observed with the maximum weight at the tip of the nose boom. Therefore, a respective analysis must always consider the instrument payload.

The HALO nose boom underwent 3 vibration tests which determined the nose boom Eigenfrequencies:

1. After a very extensive engineering and simulation effort to predict the nose boom Eigenfrequency during the HALO design phase Gulfstream Aerospace performed a first vibrational test in December 2008 during aircraft production. "*A 3.0 Kg ballast weight was installed in the instrument tray near the tip of the boom to simulate the weight of mission avionics in that location. At the forward lateral station, the greatest response was at 18.1 Hz, with smaller peaks at 16.6 and 22.9 Hz. At the forward vertical station, the greatest response was at 17.1 Hz, with smaller peaks at 22.9 and 13.7 Hz*".
2. Directly after aircraft delivery in 2009 HALO was subject to a full ground vibration test (GVT) over several weeks. This test was conducted by the DLR Institute of Aeroelasticity. The investigation determined the vibrational behavior of the complete aircraft and included all known external modifications. Figure A113 shows the boom instrumentation for that test. "*The nose boom has been tested locally with three different payload configurations. The evolution of the eigenfrequencies of the bending mode of the nose boom is shown as a function of the payload mass on the instrument tray inside the nose boom. To this end, three different nose boom configurations were investigated with 2.8 kg, 1.7 kg, and without payload mass*." The respective results can be seen in Figure A114.
3. In January 2012 the original (2 piece) HALO nose boom was replaced by a new but very similar design (single piece, made by INVENT, Germany). The certification process included another "small" nose boom GVT by RUAG Aerospace which directly compared the vibrational behavior of the two designs. "*The Gulfstream Boom 1st mode is dominant at 17.6 Hz in the z-direction. The INVENT Boom 1st mode is dominant at 18.6 Hz in the z-direction. The lateral motions of both booms are much smaller with* (a) *frequency* (which is a) *little lower than in the z-direction.*"

Figure A113: *Detail of the experimental setup from the "complete" HALO Ground Vibration Test (GVT) in 2009 by the DLR Institute of Aeroelasticity.*

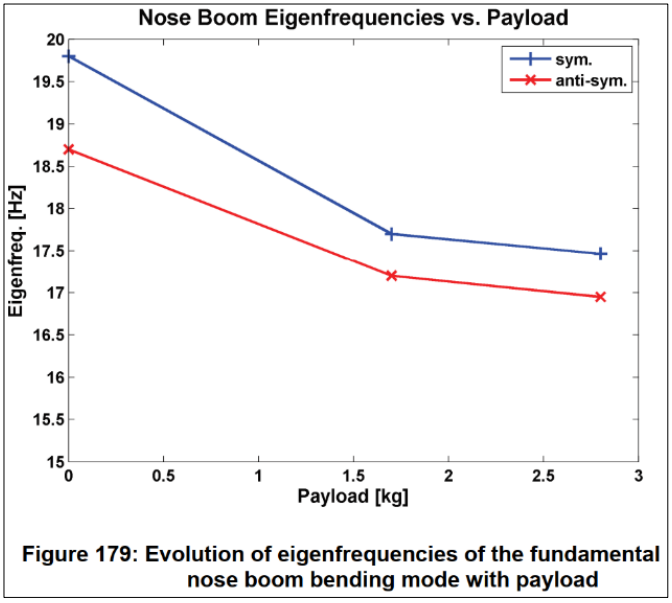

Figure 179: Evolution of eigenfrequencies of the fundamental nose boom bending mode with payload

Figure A114: *Result from the "complete" HALO Ground Vibration Test (GVT) in 2009. The plot shows the dependency of the nose boom Eigenfrequency on the weight of the instrument payload.*

Due to these tests the vibrational behavior of the HALO nose boom is completely characterized and well understood. For the present sensor payload, the most dominant Eigenfrequency is close to 19Hz and comparisons to other platforms prove that HALO has one of the stiffest booms of atmospheric research aircraft worldwide.

The Impact of Nose Boom Vibration on HALO Air Data

In airborne wind measurements turbulent fluctuations of vertical wind speed lead directly to corresponding angle of attack (α) variations. Therefore, high levels of atmospheric turbulence can create a level of α fluctuations which supersedes the vibration signal of a stiff nose boom during flight.

In case of HALO it is not possible to observe the nose boom vibration signal in α if the data was acquired in a turbulent environment like a thermally driven planetary boundary layer. Angle of attack oscillations from nose boom vibration are only visible under special flight conditions. We want to demonstrate this by comparing different HALO measurements.

High Turbulence Scenario: Convective Planetary Boundary Layer

As an example for high atmospheric turbulence levels, we chose a data set from the EMeRGe ("Effect of Megacities on the transport and transformation of pollutants on the Regional to Global scales") campaign in 2017. The data set has been presented before in the report about the calibration of the HALO air flow sensor [A2]. The selected flight took place on July 13th 2017. Figure A115 shows the 32-minutes (12:18-12:50 UTC) time series of vertical wind speed which was measured inside a convective boundary layer with strong vertical wind fluctuations (FL37, GPS flight altitude 1270 m).

The corresponding vertical wind power spectrum can be seen in Figure A116. It doesn't show any unusual feature in the expected nose boom Eigenfrequency window around 19Hz.

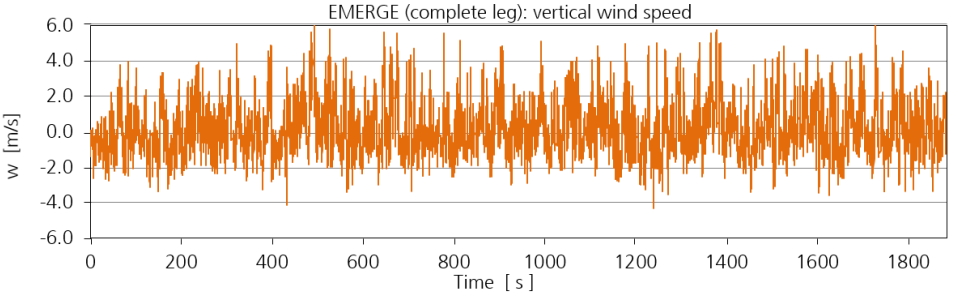

Figure A115: 100 Hz *vertical wind data time series of 32 minutes from the EMeRGe flight on July 13th 2017. The large variability of vertical wind speed (w) is characteristic for a thermally driven boundary layer environment.*

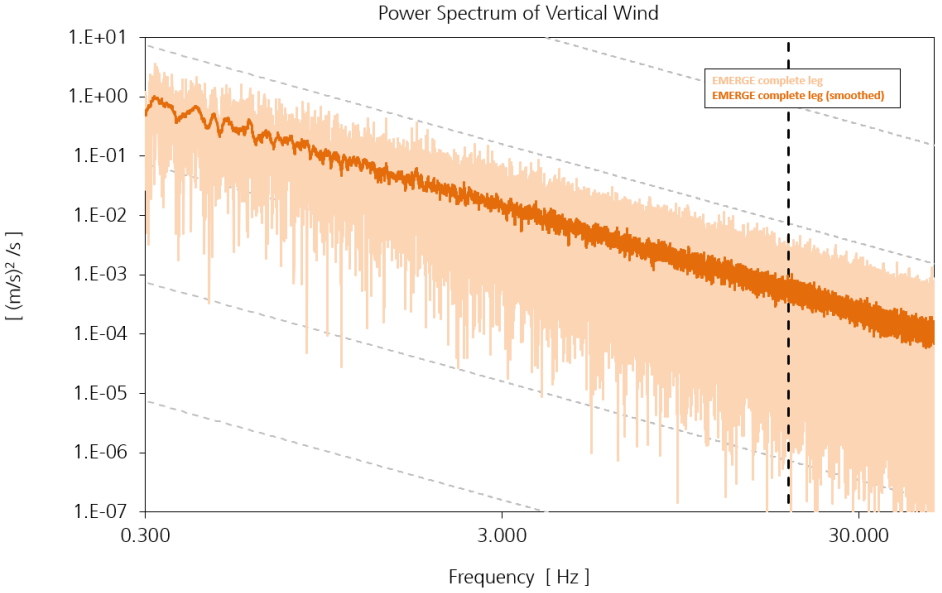

Figure A116: *Original and smoothed power spectrum of vertical wind speed (w) data as calculated from the 32-minute time series in Figure A115. The plot shows the original power spectrum as well as the smoothed curve (30 value averaging window). The dashed lines represent the expected -5/3 behavior in the inertial subrange of a turbulence spectrum. No signal from the nose boom vibration can be detected in the data at the expected frequency of about 19Hz which is highlighted by a vertical line.*

In order to visualize w/α-oscillations from the boom vibration one needs a very calm atmosphere where the wind-driven α-variability is small. This is the case for high flight levels in the upper Troposphere where the atmosphere is typically stable. On the other hand, the sensitivity/accuracy of flow measurements typically decreases with height, as can be seen from tables 2, 3 and 4 in the HALO error report [A1]. This trend hinders in principle the detection of nose boom vibration in α-data at higher altitude.

Low Turbulence Scenario: Upper Troposphere

In order to visualize the impact of nose boom vibration on w/α data we selected a data set from the HALO PHILEAS campaign in 2023. PHILEAS ("Probing High Latitude Export of air from the Asian Summer Monsoon") investigated the impacts of the Asian Summer Monsoon on global climate. The campaign which took place in Alaska, USA, was coordinated by the Institute of Energy and Climate Research (IEK) of the Forschungszentrum Jülich and the Airborne Measurements group at the Institute of Atmospheric Physics of the Johannes Gutenberg University Mainz. The data set used for this investigation belongs to the research flight "LIMBURG" which was performed on September 9th 2023 out of Anchorage, Alaska. It has a length of 26 minutes (24:00 - 00:26 UTC) contains two turns and was measured at a constant pressure altitude of 13700m (147 hPa) at a mean aircraft speed of 244m/s (M=0.82). The respective flight track can be seen in Figure A117. The following data analysis is based on 100Hz wind data which was subject to the full airflow correction scheme as described in the HALO report on the calibration of the flow sensor [A2].

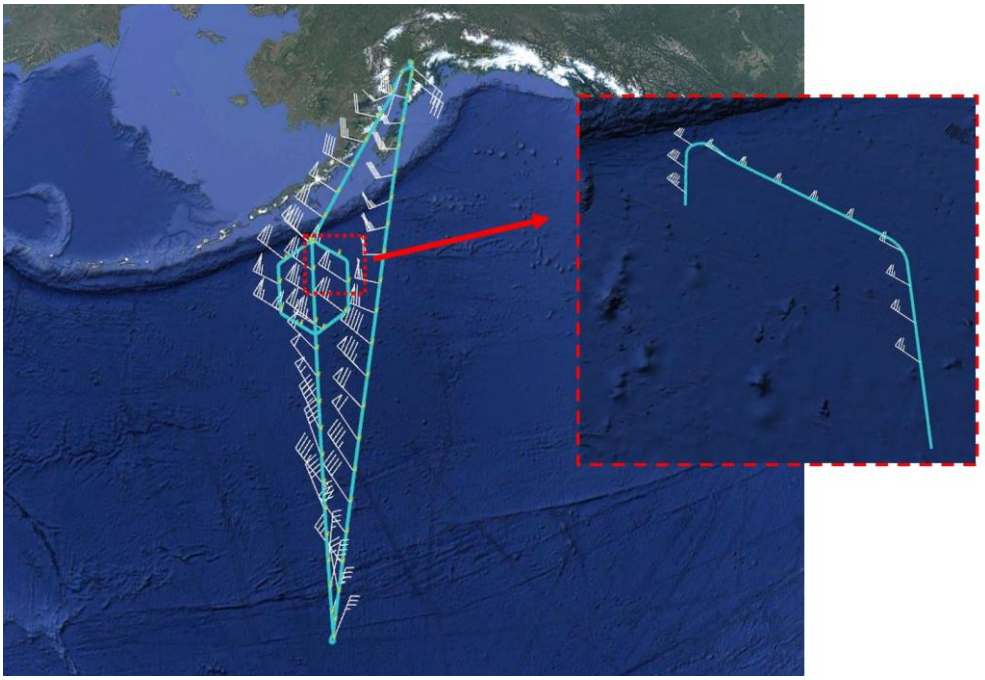

Figure A117: *Flight track of the PHILEAS research flight LIMBURG from September 9th 2023. The flight was conducted out of Anchorage, Alaska. The 26-minute flight leg which was used for this study is shown on the right side.*

As expected the vertical wind variability at this height is significantly lower than the boundary layer case which can be seen in Figure A118 where the time series of vertical wind / angle of attack from EMeRGe and PHILEAS are directly compared to each other.

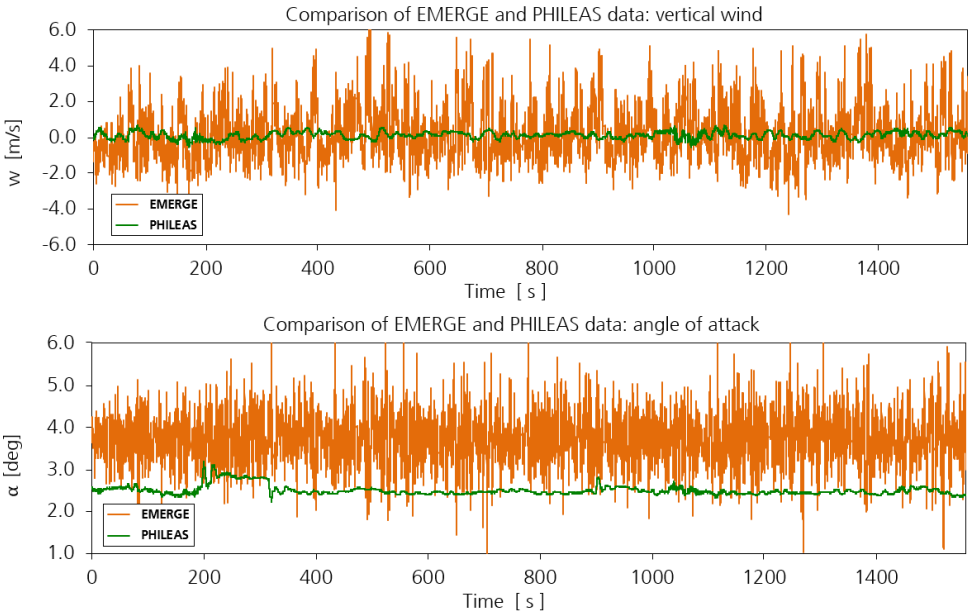

Figure A118: *Comparison of EMeRGe and PHILEAS data over a time window of 26 minutes. The different variability of vertical wind and angle of attack data in a convective planetary boundary layer and the upper troposphere is clearly visible. The different angle of attack values for the two data sets are due to the flight conditions (speed, altitude).*

However, the vertical wind power spectrum from the PHILEAS data which is displayed in Figure A119 still doesn't show a significant feature at the nose boom Eigenfrequency of 19 Hz despite the fact that the signal levels of both spectra differ by more than two orders of magnitude.

The reason for the missing nose boom resonance peak becomes visible when the PHILEAS time series of vertical wind speed is plotted separately as displayed in Figure A120: the data shows two short periods with slightly higher atmospheric wind fluctuations.

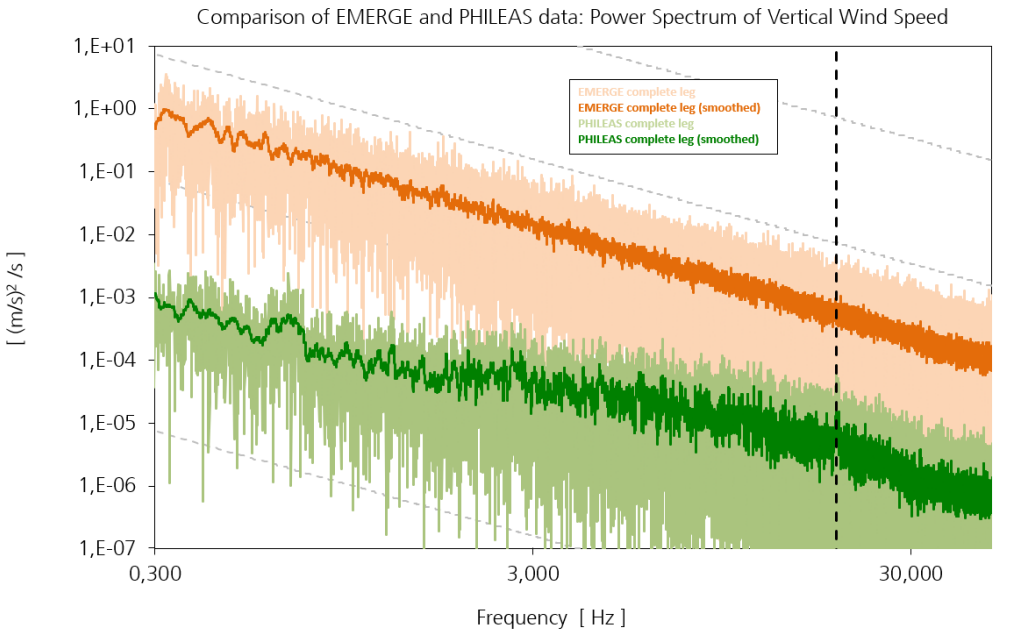

Figure A119: *Comparison of vertical wind power spectra from EMeRGe and PHILEAS. The spectra were calculated from the complete flight legs of 32 min and 26 min respectively. According to theory the Kolmogorov Scale ("-5/3-law") of the low turbulence scenario is found at higher frequencies. The nose boom resonance frequency is highlighted by a vertical line.*

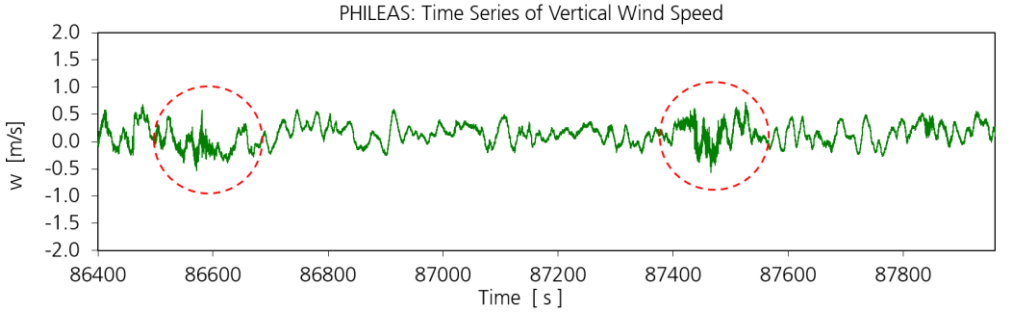

Figure A120: *PHILEAS vertical wind data from the 26-minute time leg which was investigated during this study. The data set shows two sections with increased atmospheric turbulence which are marked by a red circle.*

Comparison of the different Scenarios

In order to compare the wind and flow data with each other for different atmospheric conditions we selected 3 short time series of 2 minutes length each from the EMeRGe and PHILEAS data sets. Figure A121 shows the selected "cases" which mainly differ in the intensity of atmospheric turbulence. Case 1 from the EMeRGe boundary layer measurement shows the highest level of atmospheric turbulence while case 2 and case 3 from PHILEAS took place at much higher altitude with very little (case 2) and almost no turbulence (case 3).

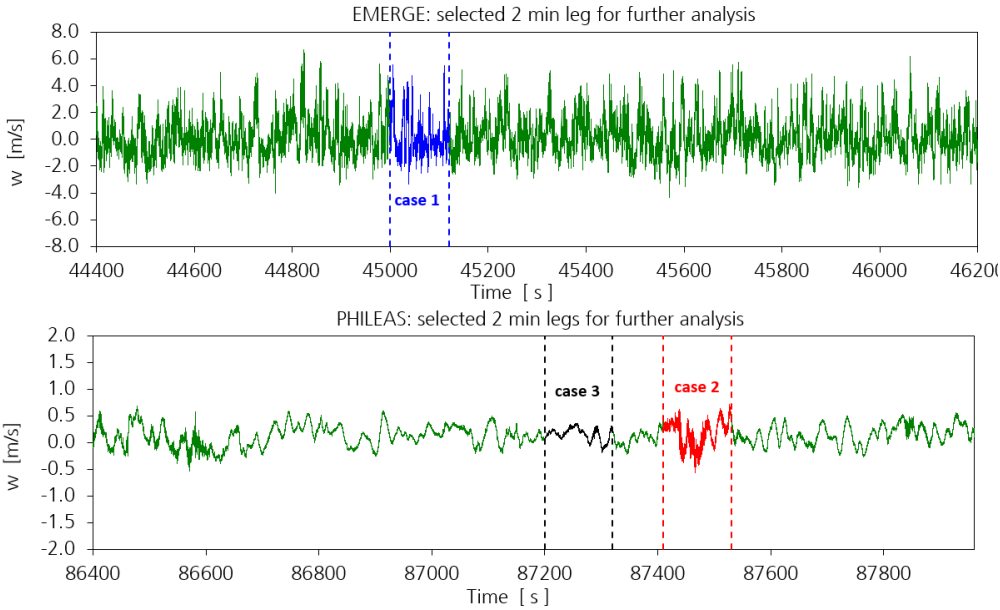

Figure *A121*: *Selection of three 2-minute flight legs from the EMeRGe and PHILEAS data set for the spectral analysis of this study. The two legs from PHILEAS concern different levels of atmospheric turbulence.*

Figure A122 shows the spectra which were calculated from these 2-minute time series and now the spectrum of case 3 shows the expected sharp resonance peak from the nose boom vibration at 19 Hz. The plot also explains the above findings: The nose boom resonance peak vanishes in the spectrum when the atmospheric turbulence level at 19Hz is higher than this vibration signal.

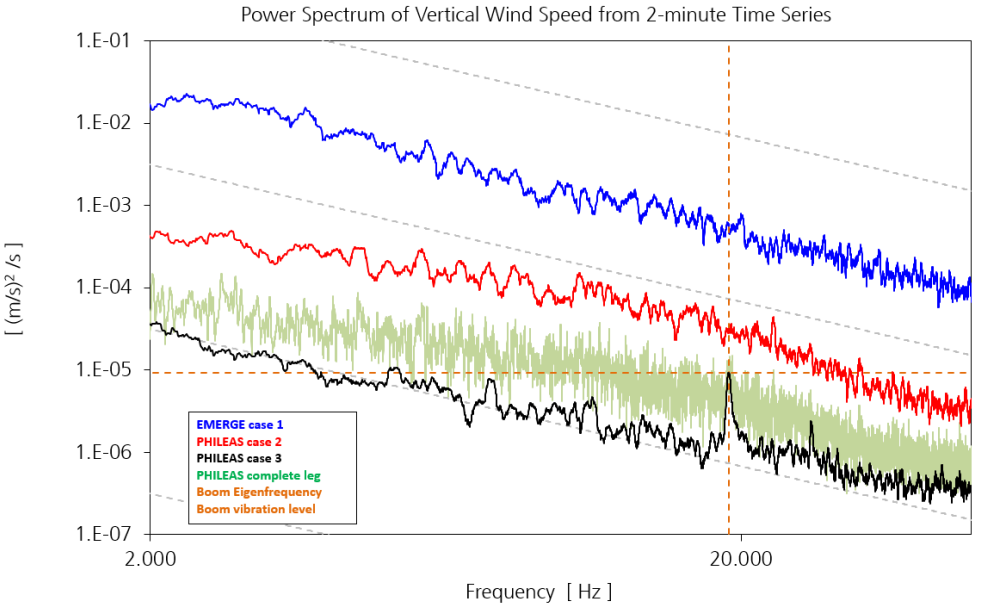

Figure A122: *Power Spectrum of vertical wind data for the 2-minute time series shown in Figure A121. While case 1 from the EMeRGe data and case 2 of PHILEAS show no obvious feature at 19 Hz, the resonance peak from the nose boom vibration is clearly visible in case 3 of PHILEAS which took place in an extremely calm atmosphere. The power spectrum of the complete PHILEAS leg is plotted for comparison.*

Determination of Instrument Precision

In order to interpret the data correctly it is important to make sure that the observed 19 Hz modulation of the calculated vertical wind speed is indeed a real air flow signal and not caused by other effects.

Therefore, a detailed spectral analysis was performed for all units which contribute to the calculation of w. The investigation for case 3 of PHILEAS concerned data from the inertial reference system (velocities, accelerations, attitude angles, angular rates), from the instrument tray (tray acceleration) and from the 5-hole probe (static pressure, dynamic pressure, differential flow angle pressure). The investigation concerned the power spectra of all these units and searched for unusual features in a small frequency window around 19 Hz. Figure A123 shows the location of the sensors involved and the boom dimension.

The minimization of the influence of nose boom vibration on the pressure measurements was already an important design criterion in the development of the nose boom payload itself. The pressure sensor orientation on the instrument tray was chosen in a way that the influence of lateral boom vibrations on the measurement is reduced to a minimum: the pressure membrane is oriented in the aircraft y-z-plane because aircraft accelerations along the x-axis are usually much smaller than the lateral (y- and z-) values during flight.

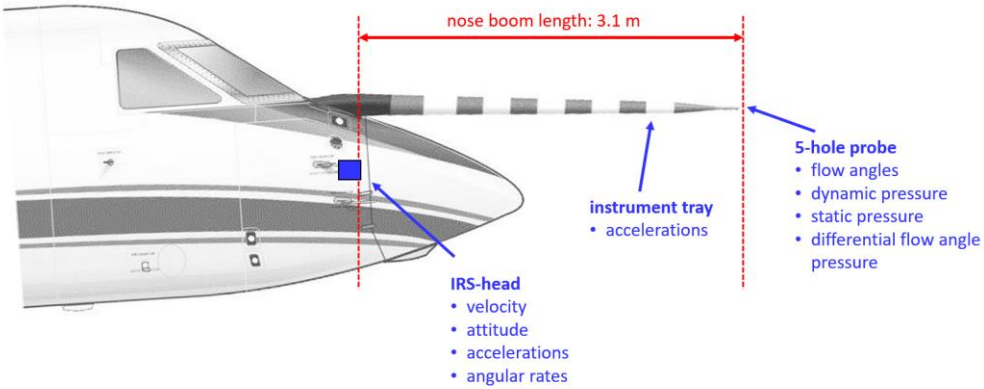

Figure A123: *HALO nose section: boom length location of the different BAHAMAS sensors.*

The spectral analysis of case 3 with the visible resonance peak in the wind data proved that only a few units show a respective feature at 19Hz. The most important findings can be seen in Figure A124, Figure A125 and Figure A126.

As one can see from the IRS data the aircraft nose structure is subject to a very weak pitch oscillation. However, the observed amplitude is significantly smaller than the respective angle of attack value at the boom tip.

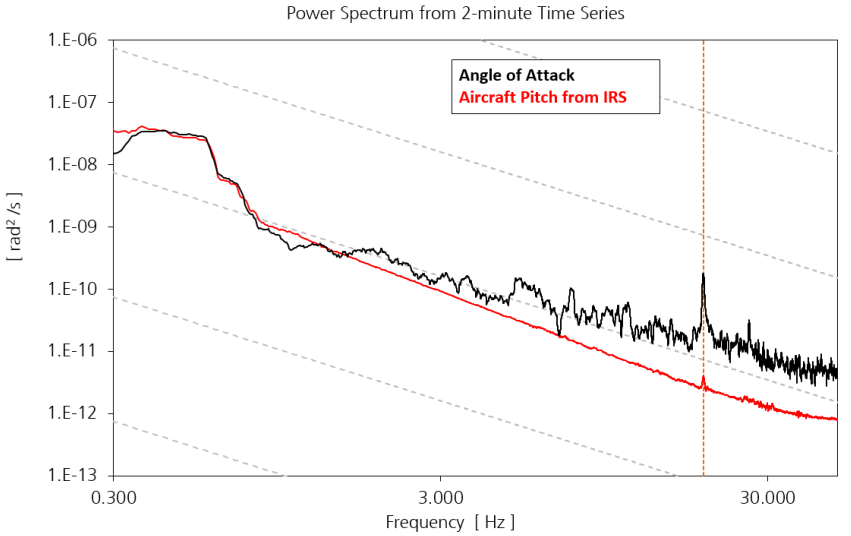

Figure A124: *Power spectrum of the angle of attack (from the nose boom flow sensor) and pitch (from the inertial reference system) for case 3 from the PHILEAS data set. Both units show a resonance peak at 19Hz. The plot also proves that pitch and angle of attack are identical at low frequencies. At higher frequencies both spectra differ due to the α contributions from vertical wind turbulent fluctuations. This also explains the higher spectral energy of α in this part of the spectrum.*

Similar to the angle of attack / pitch data in Figure A124 the acceleration measurements on the instrument tray and in the aircraft nose section shown in Figure A125 differ significantly from each other: the characteristic 19 Hz vibration signal is only observed by the nose boom instrumentation.

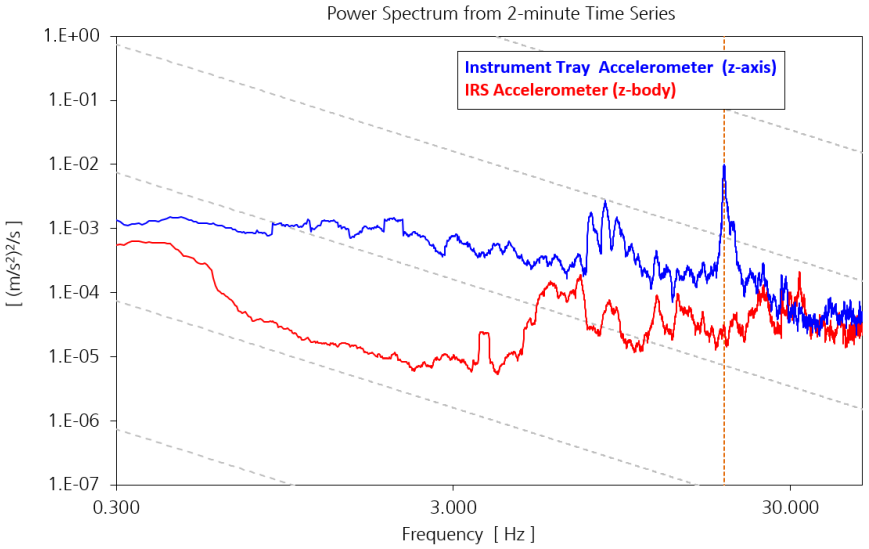

Figure A125: *Power spectrum of the z-accelerations from the accelerometer on the instrument tray in the nose boom and from the experimental inertial reference system in the aircraft nose for case 3 from the PHILEAS data set.*

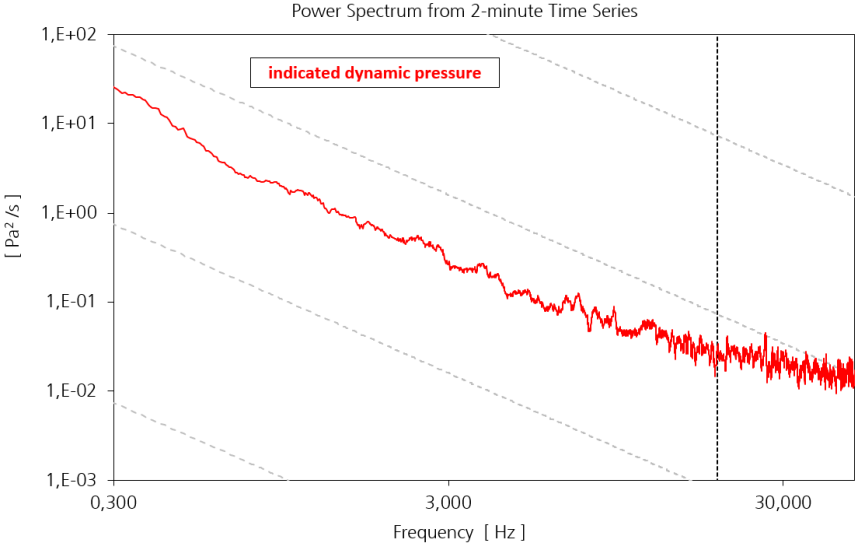

Figure A126: *Power spectrum of indicated dynamic pressure for case 3 from the PHILEAS data set. The inner sensor element of the differential pressure instrument is the same as for the α-sensor.*

From Figure A126 one can see that the spectrum of the indicated dynamic pressure from the flow sensor does not show any unusual feature at 19 Hz. The dynamic pressure measurement uses the same sensor element as the α differential pressure instrument. This proves that the 19 Hz modulation in the α-pressure measurement is not a sensor artefact which is caused by the instrument tray vibration.

We therefore conclude, that the observed α-oscillation must be generated in between the IRS and the flow angle sensor i.e. by a deformation of the nose boom structure (including the fuselage attachment of the boom). The small footprint of the oscillation in the IRS-data indicates that the boom vibration propagates into the aircraft nose structure.

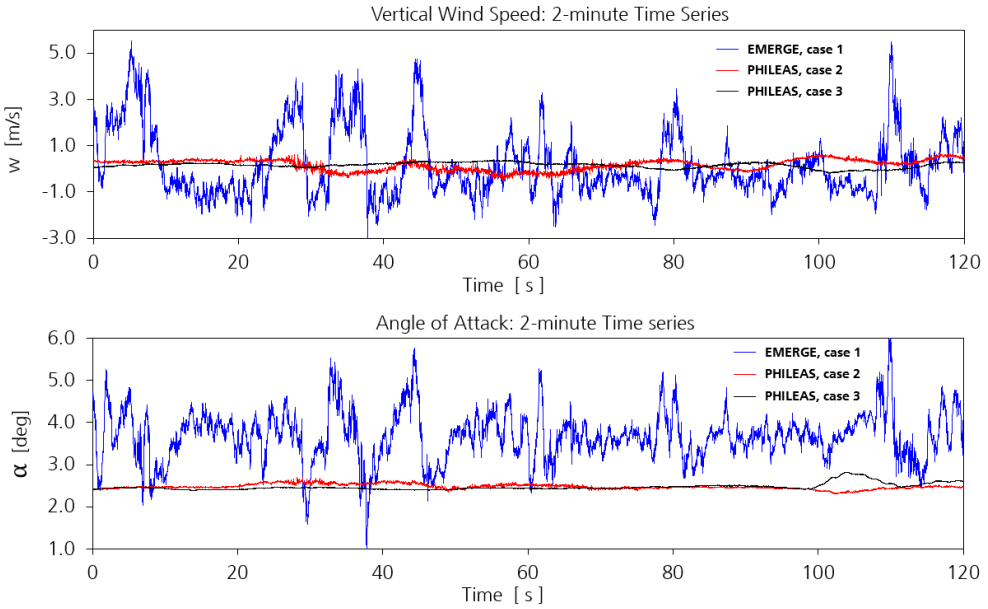

Figure A127*: Comparison of vertical wind and angle of attack data from the three 2-minute flight legs which were analyzed during this investigation. The different levels of atmospheric variability are clearly visible.*

Figure A127 and Figure A128 directly compare the different 2-minute time series with each other in order to visualize the different atmospheric background levels of the selected cases.

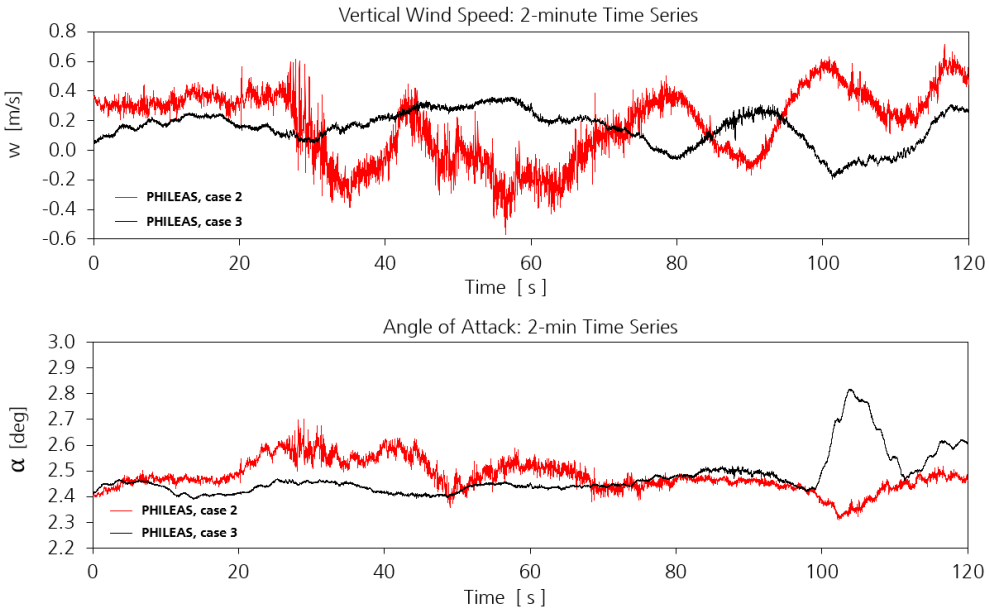

Figure A128: *Comparison of vertical wind and angle of attack data from the two 2-minute flight legs which were selected from the PHILEAS data. Despite the extremely small variance of wind data at this altitude a difference in the atmospheric turbulence level is visible.*

It is an interesting fact that two short events (Figure A120) with an extremely small atmospheric turbulence level of only 0.2 m/s (case 2 in Figure A128) are sufficient to lift the vertical wind power spectrum of the complete 26 minute time leg from the PHILEAS data above the detection limit for the nose boom vibration.

Figure A129 zooms into a very calm section of case 3 and visualizes the signal amplitudes which are caused by the nose boom vibration. The time series prove that the nose boom vibration leads to angle of attack oscillations with amplitudes in the order of 0.005° which is equivalent to a vertical wind speed of 2cm/s and a 2 Pa differential pressure in the α-pressure measurement of the 5-hole probe. An angle of 0.005° corresponds to a lateral vibration amplitude of 0.3 mm for the HALO nose boom length of 3.1 m.

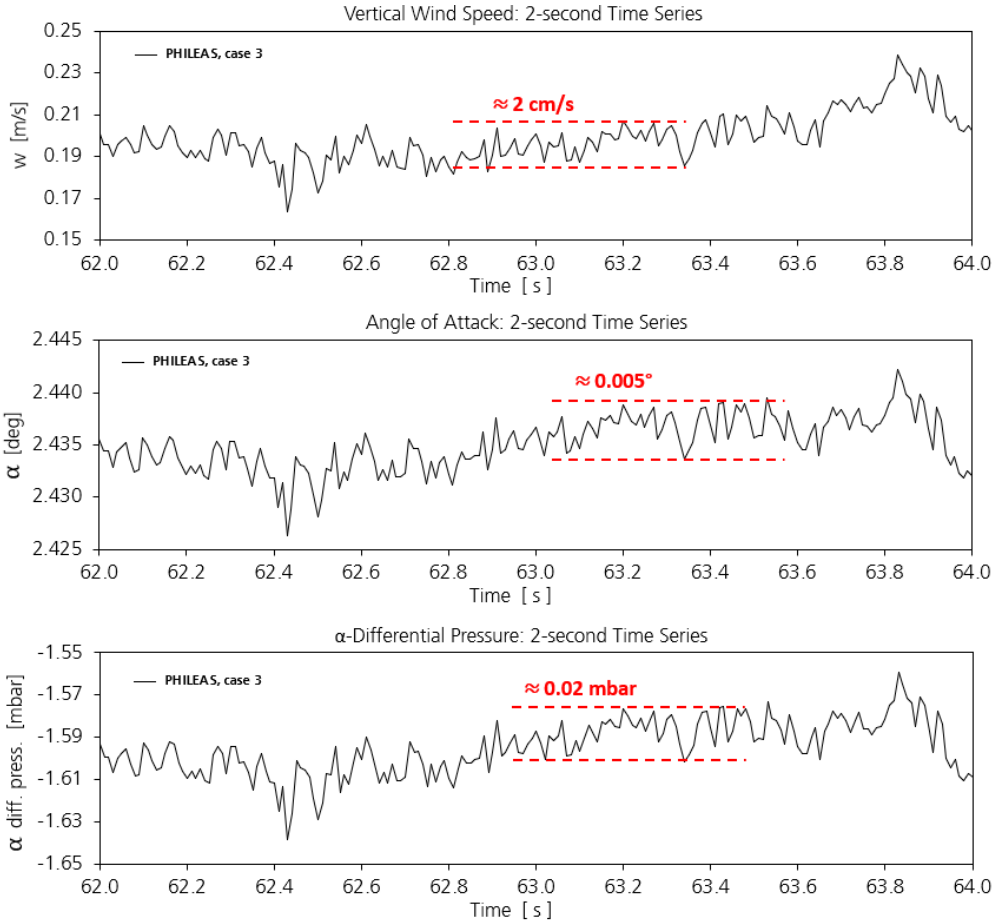

Figure A129: *2-second time series of vertical wind speed, angle of attack and α-differential pressure from case 3 of the PHILEAS data set. The time window contains ≈40 nose boom oscillations and the vibrational amplitudes are highlighted. The respective standard deviations for the 2-second time window (which include atmospheric contributions) are 1.2 cm/s (w), 0.0025° (α) and 1.3 Pa (α-pressure).*

Conclusion

We have demonstrated that the HALO air flow instrumentation is able to detect the vibration signal of the aircraft nose boom as a 19 Hz angle of attack oscillation during flight. This nose boom signal is only visible under very calm atmospheric conditions and has an amplitude of 0.005° which is almost 2 orders of magnitude smaller than the typical accuracy of α at this altitude (1σ: 0.15°, according to table 4 in the HALO error report [A1]).

The signal level of the HALO inflight nose boom vibration can be seen as an upper limit for the precision of BAHAMAS air flow (α) and wind (w) measurements. In other words: the HALO wind measurement system is obviously able to resolve real wind fluctuations down to this order of magnitude.

However, the curve of case 3 in Figure A124 suggests that this still is a rather conservative estimation since 1) the resonance peak exceeds the atmospheric background level by one order of magnitude and 2) no onset of white noise can be observed in the spectrum - even at higher frequencies. Therefore, it seems that the real system precision is probably a factor 3-4 better than observed amplitude of the boom vibration.

Appendix References

[A1] Andreas Giez, Martin Zöger, Christian Mallaun, Vladyslav Nenakhov, Marina Schimpf, Christoph Grad, Andreas Numberger, Kevin Raynor, Determination of the Measurement Errors for the HALO Basic Data System BAHAMAS by Means of Error Propagation. DLR-Forschungsbericht 2022-27, 2023, ISRN DLR-FB-2022-27 https://elib.dlr.de/193175/

[A2] Andreas Giez, Christian Mallaun, Vladyslav Nenakhov, Martin Zöger, Calibration of a Nose Boom Mounted Airflow Sensor on an Atmospheric Research Aircraft by Inflight Maneuvers. DLR-Forschungsbericht 2021-17, 2021, ISRN DLR-FB—2021-17 https://elib.dlr.de/145969/

1434-8454

ISRN DLR-FB—2025-17